UNIVERSITÄT HAMBURG, DEPARTMENT PHYSIK

Electronic and Atomic Structure at Metal - Oxide Heterointerfaces

Dissertation

zur Erlangung des Doktorgrades
des Department Physik
der Universität Hamburg

vorgelegt von

Dipl. min. Univ. Christoph Friedrich Schlueter
aus München

Hamburg
2013

Gutachter der Dissertation:	Prof. Dr. Robert Johnson
	Prof. Dr. Christof Kunz
Gutachter der Disputation:	Prof. Dr. Robert Johnson
	Priv. Doz. Dr. Jörg Zegenhagen
Datum der Disputation:	05.04.2013
Vorsitzender des Prüfungsausschusses:	Priv. Doz. Dr. Georg Steinbrück
Vorsitzender des Promotionsausschusses:	Prof. Dr. Peter Hauschildt
Dekan des Fachbereichs:	Prof. Dr. Daniela Pfannkuche

Zusammenfassung

In der vorliegenden Arbeit wird über Untersuchungen an Oxidmaterialien berichtet. Es werden Ergebnisse präsentiert, die mittels Photoelektronenspektroskopie mit harten Röntgenstrahlen (HAXPES) sowie der Methode der stehenden Röntgenwellenfelder (XSW) gewonnen wurden. Die Kombination mit XSWs verleiht Photoelektronenspektroskopie eine Ortsempfindlichkeit mit Picometer Auflösung.

An den Grenzflächen von $SrTiO_3$ mit polaren Oxiden wie $LaAlO_3$ oder $LaGaO_3$ kommt es bei geeigneter Präparation zu der Ausbildung eines quasi zwei-dimensionalen Elektronengases (2DEG). Im Rahmen dieser Arbeit wurden an der ESRF und in Neapel hergestellte Schichten untersucht. Oberflächenröntgenbeugung bestätigt die ausgezeichnete Epitaxie der Filme. Mit Hilfe der XSW-Methode wurden Bilder der Struktur der $LaAlO_3$ Deckschichten im realen Raum rekonstruiert. Diese Bilder zeigen Verzerrungen im $LaAlO_3$ Gitter, die geeignet sind, das elektrostatische Potenzial in der Deckschicht zu verringern. Desweiteren erlauben XSW/HAXPES Messungen die Beiträge von Ti und Sr,O zum 2DEG in der Nähe des Fermi-Niveaus zu identifizieren. Die Auswertung legt nahe, dass das Ti $3d$-Band das Fermi-Niveau kreuzt, jedoch auch einige Zustandsdichte auf Sauerstofffehlstellen zurückzuführen ist.

Übergitter von $SrTiO_3$ und polarem $CaCuO_2$ wurden mittels HAXPES untersucht. Die Polarität des $CaCuO_2$ sollte, ähnlich wie im Fall von $SrTiO_3/LaAlO_3$, zu einem divergierenden Oberflächenpotenzial führen. Ca, Sr und Ti Spektren geben Hinweise auf eine Umverteilung von Sauerstoff, die in der Lage ist dieses Potential zu kompensieren. Durch Sauerstoffbeladung werden diese Überstrukturen supraleitend $T_C \sim 40$ K. Nebenkomponenten in den Spektrallinien der Metallatome und ein neuer Abschirmungskanal in Cu $2p$ Rumpfniveauspektren der stärker oxidierten, supraleitenden Proben sind ein Anzeichen für die Lochdotierung der $CaCuO_2$ Blöcke.

Magnetoresistive $La_{0.65}Sr_{0.35}MnO_{3-\delta}$ Filme zeigen eine Abnahme der Leitfähigkeit und der Metall-Isolator Übergangstemperatur bei zunehmender Fehlstellenkonzentration δ. Temperaturabhängige Transport und HAXPES Messungen unterstützen einen Variable-Range Hopping Mechanismus als Ursache des isolierenden Zustands. Zusätzlich reagiert der abgeschirmte Zustand in den Mn $2p$ Spektren empfindlich auf δ, was auf einen Rückgang der Hybridisierung der dotierten Zustände mit dem $2p$ Orbitalen des Sauerstoffs deutet.

Abstract

The results of a series of investigations on modern oxide materials using hard X-ray photoelectron spectroscopy (HAXPES) combined with the X-ray standing wave (XSW) method are described in this thesis. The combination of hard X-ray photoelectron spectroscopy and X-ray standing waves enables the electronic structure to be measured with a spatial resolution in the picometer range.

Under suitable preparation conditions, a quasi two-dimensional electron gas (2DEG) is formed at the heterointerfaces of strontium titanate ($SrTiO_3$) with polar oxides, such as lanthanum aluminate ($LaAlO_3$) or lanthanum gallate ($LaGaO_3$). Samples were grown at the ESRF and in Naples and surface X-ray diffraction confirmed the excellent epitaxial quality of the films. The XSW-method was used to reconstruct images of the structure of $LaAlO_3$ layers in real space. These images give evidence of distortions in the $LaAlO_3$ structure which facilitate the compensation of the potential differences. Furthermore, XSW/HAXPES measurements permit the Ti and Sr,O contributions to the 2DEG close to the Fermi level to be identified unambiguously. The analysis shows that the $3d$ band crosses the Fermi level and that some density of states is associated with oxygen vacancies.

Superlattices of $SrTiO_3$ with polar calcium cuprate ($CaCuO_2$) were investigated by HAXPES. Similar to the case of $SrTiO_3/LaAlO_3$, the polarity of $CaCuO_2$ should lead to a diverging surface potential. The core level spectra from Ca, Sr, and Ti show that there is a redistribution mechanism for oxygen which compensates the potential differences. When the oxygen concentration is enhanced these superstructures become superconducting ($T_C = 40\,K$). The increased oxidation of the superconducting material is revealed by the additional components in the core level spectra of the metal atoms and in the appearance of a new screening channel in Cu $2p$ core level spectra, which signals the hole doping of the $CaCuO_2$ blocks.

Magnetoresistive lanthanum strontium manganate ($La_{0.65}Sr_{0.35}MnO_{3-\delta}$) films show a reduction in both the conductivity and the metal–insulator transition temperature with increasing vacancy concentration δ. Temperature-dependent transport and HAXPES measurements support variable-range hopping as the mechanism creating the insulating phase. In addition, the screening state in the Mn $2p$ spectra reacts sensitive to the vacancy concentration δ, which indicates a reduction in the hybridization of the doping-induced states with the $2p$ orbitals of oxygen.

Contents

List of Figures

List of Tables

1. Introduction

Oxide based materials are promising candidates for future electronic devices. Transition metal oxides (TMOs) are particularly interesting because they exhibit an enormous range of functional properties that can be tuned for different applications. TMOs cover a wide range of electrical conductivity exhibiting insulating, metallic, and even high-temperature superconducting (HTS) behaviour. They show multiferroic properties such as ferroelectricity, in addition to magnetism and colossal magnetoresistance (CMR). The magnetic properties are of special interest in modern electronics, since magnetic[1] and non-magnetic[2] oxides are being discussed for the next generation of data storage devices. Zaag *et al.*[3] have already reported the construction of all-oxide spin valves based on Fe_3O_4. One of the most prominent examples of oxide materials in use is the metal-oxide-semiconductor field-effect transistor (MOSFET), which is now a standard component in virtually all electronic devices.

The huge variety of properties presented by TMOs has stimulated strong interest in fundamental research as well as in material science and technology. Given the complex nature of these compounds, it is not surprising that new and unexpected effects may arise at interfaces between these materials. The physics of surfaces and interfaces is continuing to grow in importance since the ongoing trend of miniaturization yields devices that are entirely dominated by surface and interface effects. Several examples such as exchange bias devices, superconducting, ferroelectric and magnetic tunnel junctions, and ferromagnetic metallic states in superlattices composed of antiferromagnetic insulators, can be found in the literature. In 2004, Ohtomo and Hwang[4] at Bell Laboratories were the first to observe the surprising properties of $LaAlO_3/SrTiO_3$ heterostructures, in which a superconducting 2-dimensional electron gas (2DEG) is formed in the interfacial region of $SrTiO_3$.

The band theory of oxides is often complicated by correlation effects between the charge carriers. In general, the description of the electronic states in a solid is a many-body problem since the electrons influence each other via Coulomb interactions. In the mean-field approximation, each electron is assumed to interact with the crystal potential, derived from all of the charges in the system. This approximation has been applied very successfully in solid state physics. However, especially in the d-band TMOs, strong correlations between the electrons can

lead to a break down of conventional band theory. It is exactly these interactions which give rise to the most exciting properties currently found in the oxides, namely, metal–insulator transitions, magnetic ordering and superconductivity, but, unfortunately complicate their understanding.

One of the experimental techniques expected to yield important information about the electronic properties of materials is photoelectron spectroscopy, since it probes the occupied states. Hard X-ray photoelectron spectroscopy (HAXPES) is a truly bulk sensitive technique due to the high energy of the emitted photoelectrons. It is essential to first determine the properties of bulk samples to be able to compare the measured data with the results of theoretical predictions. In practice the electronic and magnetic properties can be strongly influenced by surface effects. They react sensitively to structural modifications at the surfaces due to reconstruction or relaxation. The intrinsic electronic properties at the surface are different from the bulk (surface states)[5,6] and surface contamination (i.e. hydroxyl groups, carbon, etc.) can additionally be present. Hard X-ray photoelectron spectroscopy is ideal for studying buried interfaces and is thus particularly well suited for analyzing the interfacial electronic structure of TMO systems.

The X-ray standing wave (XSW) technique allows one to correlate structural and electronic aspects in these materials. The technique exploits the possibility of sweeping the position of the maxima and minima of the XSW field, created by interference of the incoming and reflected beams under Bragg, or total reflection, conditions, through the structure. This makes the XSW technique highly site-specific. With the help of XSWs, the contribution to the valence band from different atomic sites can be deconvolved, a feature extremely interesting when studying highly-correlated electron systems. In the past, this method has been used to study the valence electronic structure of TiO_2,[7] V_2O_3[8] and $SrTiO_3$.[9] In a much more straightforward way, the site-specificity of the XSW technique can be used to get structural information about the sample. Most interestingly, if a sufficient numbers of reflections are measured, model-free real space images can be calculated from the data.

These experimental techniques make use of the brilliant photon beam provided by third generation synchrotron sources like the ESRF and high-throughput analyzers, capable of detecting electrons at high energies. These powerful experimental techniques are able to provide novel insights into the electronic and atomic structure in metal oxide heterostructures.

Outline

In this thesis, HAXPES and XSW studies of several complex TMO materials highlight some of the aspects presented above. The samples studied were het-

erointerfaces of $SrTiO_3$ with $LaAlO_3$, $LaGaO_3$ and $NdGaO_3$, superlattices of $CaCuO_2$ with $SrTiO_3$ and $La_{1-0.65}Sr_{0.35}MnO_3$, as well as oxygen-deficient films of $La_{0.65}Sr_{0.35}MnO_{3-\delta}$.

Chapter 2 gives an introduction to the experimental techniques employed. Both pulsed laser deposition and molecular beam epitaxy were used for sample preparation. Initial sample characterization was performed using atomic force microscopy (AFM) and surface X-ray diffraction (SXRD). Since photoelectron spectroscopy and the X-ray standing wave technique are the key experimental methods used in this thesis they are presented in more detail. Chapter 3 contains a short introduction to the experimental setups used in the experiments at ID32 at the ESRF.

The $SrTiO_3/LaAlO_3$ interfaces are the subject of Chapter 4. Thin film growth at the ESRF and the characterization of the samples using SXRD and AFM will be discussed. Since the in-house grown samples were not so reproducible, higher-quality thin film samples prepared at CNR-SPIN (Naples, Italy) were studied. For these films, SXRD measurements confirmed that the samples were high-quality epitaxial films. A detailed XSW imaging study is presented, which compares the lattice distortions in 2 monolayer (ML) and 5 ML thick LAO films. The images show distortions in the metal oxide planes and a modulation of the interplanar distances. Larger distortions are found in the thinner samples. HAXPES spectra for the conducting interface samples, revealed a weak intensity in the band gap of $SrTiO_3$, originating from the 2DEG. This spectral yield was decomposed into the site-specific contributions and compared to similar spectra from Nb-doped $SrTiO_3$ and and oxygen-deficient $SrTiO_{3-\delta}$. The analysis indicates a mixed origin of the 2DEG, from oxygen vacancies as well as intrinsic field-effect doping.

In Chapter 5, novel superconducting $CaCuO_2/SrTiO_3$ superlattices are discussed. These superlattices consist of three monolayers of $CaCuO_2$ and two monolayers of $SrTiO_3$, and were found to be superconducting, after annealing under highly oxidizing conditions. The polar nature of the $CaCuO_2$ should create a diverging potential, similar to the situation in $SrTiO_3/LaAlO_3$. HAXPES measurements give evidence for an efficient compensation of this potential build-up, based on a redistribution of oxygen at the interfaces. Furthermore, the HAXPES measurements on superconducting samples show a stronger oxidation of the interfacial metal atoms as a result of the incorporation of additional oxygen at the interfaces. This results in hole doping of the $CaCuO_2$ blocks.

HAXPES and transport measurements on oxygen-deficient $La_{0.65}Sr_{0.35}MnO_{3-\delta}$ films are described in Chapter 6. The metal–insulator transition temperature and the conductivity of these samples decreases with increasing oxygen vacancy concentration. HAXPES measurements were performed at room temperature and 86 K. The Mn $2p$, $3s$ and valence band spectra showed significant changes related

to the vacancy concentration. The results give evidence for band redistribution and point to a variable-range hopping driven insulating state.

The majority of the results described in this thesis have been presented at international conferences and were either published in peer-reviewed journals or were submitted for publication. The publications on the site-specific valence band structure of $SrTiO_3/LaAlO_3$ interfaces and the XSW imaging of distortions in $LaAlO_3$ films are currently in preparation. The HAXPES study on the $CaCuO_2/SrTiO_3$ superlattices has been submitted to Physical Review Letters.[10] The HAXPES study on oxygen-deficient $La_{0.65}Sr_{0.35}MnO_{3-\delta}$ films has been published in Physical Review B.[11]

2. Materials and Methods

This chapter starts with a brief introduction to the oxide compounds studied in the following chapters. Next the experimental techniques, which were available at the ID32 beamline at the ESRF and its attached surface characterization laboratory (SCL) are described. The sample preparation was performed using either pulsed laser deposition (PLD) or molecular beam deposition (MBE). The samples were characterized by means of a variety of techniques – surface X-ray diffraction, hard x-ray photoemission and the X-ray standing wave technique – using synchrotron radiation.

2.1. Polar and non-polar transition metal oxides

Many oxides crystallize in the perovskite structure which can be formed with a variety of modifications. Section 2.1.1 introduces the undistorted cubic perovskite structure as found in $SrTiO_3$. Depending on the cation ratios, systematic distortions are observed. The guiding principle for these distortions will be outlined in Section 2.1.2. $LaGaO_3$, $NdGaO_3$, and $La_{(1-x)}Sr_xMnO_3$ will be discussed as representative examples. Finally, in Section 2.1.3, the closely-related infinite layer structures as found in $CaCuO_2$ will be introduced.

$SrTiO_3$, $NdGaO_3$ and $LaAlO_3$ are routinely used as substrate materials since they have a small lattice mismatch to other oxide compounds such as YBCO or the manganite system ($La_{(1-x)}Sr_xMnO_3$) (see Table 2.1). The chemical formulas are regularly abbreviated by the first letters of the of the constituting elements (e.g. $SrTiO_3$ as STO and $LaAlO_3/SrTiO_3$ as LAO/STO)). Throughout this text the full chemical formulas are used.

2.1.1. Cubic perovskites

The generalized structure formula is ABO_3 where the 'A' ions are larger than the 'B' ions.[12] The structure can be described as a cubic primitive lattice of B

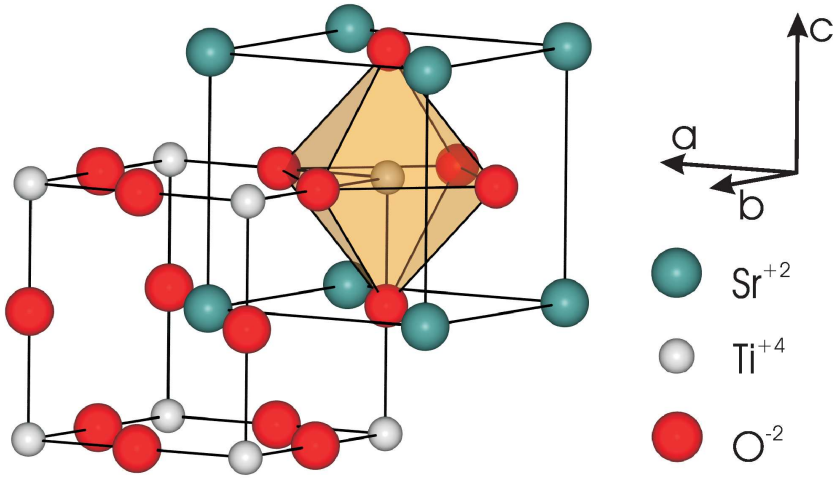

Figure 2.1.: $SrTiO_3$ crystallizes in the cubic perovskite structure with strontium ions (Sr^{2+}) (grey), titanium ions (Ti^{4+})(blue) and ions (O^{2-}) (red). The $TiO_{6/2}$ octahedron and the two possible cell settings are shown.

ions with the voids filled by the other ions (see Fig. 2.1). The oxygen ions sit half-way between the 'B' sites on the edges of the cell giving rise to an octahedral coordination of the 'B' cations. The larger 'A' ions are located in the large void in the center of the cell and it has a cuboctahedral (12-fold) coordination. The structure is commonly described either with the origin located at either the A or the B-site.

Strontium titanate, $SrTiO_3$, is probably the most well-known representative of this class of materials. It is frequently used as a substrate for thin film growth. The material properties of $SrTiO_3$ are intriguing since it is a paramagnetic insulator at perfect stoichiometry, a ferroelectric under strain, a metal upon doping and even a superconductor in the mK range. $SrTiO_3$ has a band gap of 3.3 eV[13] and is optically transparent and insulating. It can be rendered conducting by doping either with oxygen vacancies or cation impurities such as Nb or La yielding an n-type material.

Multiple variants of the basic structure, such as $A_nB_nO_{3\times n}$, the ability to accommodate mismatch in the A-O and B-O bond length, as well as different equilibrium bond lengths, when more than one A or B-site cation is present, lead to a wide range of stoichiometric perovskites. In addition, the possibility of substitution at either cation position and a huge tolerance to vacancies and intergrowth structures give rise to an abundant structural variety in the perovskite family.

Table 2.1.: Summary of the space groups and lattice parameters of the investigated oxide materials and their lattice mismatch to $SrTiO_3$.

Compound	**Space group**	**Lattice parameters (Å)**			**Mismatch to SrTO (%)**		
		a	b	c	in a	in b	in c
$SrTiO_3$	$Pm\overline{3}m$	3.905					
$LaAlO_3$	$R\overline{3}c$	5.364		13.109	-2.955	-2.955	-3.191
$LaGaO_3$	$Pbnm$	5.527	5.494	7.777	+0.008	-0.51	-0.42
$NdGaO_3$	$Pbnm$	5.433	5.504	7.716	-1.61	-0.34	-1.21
$La_{0.7}Sr_{0.3}MnO_3$	$Pnma$	5.451	5.981	7.739	-1.312	+7.666	-0.917
$CaCuO_2$	$P4mm$	3.856		3.18	-1.27	-1.27	-22.8

2.1.2. Distorted perovskites

Structural modifications depend on the cation radius ratios. A tolerance factor was introduced in 1926 by Goldschmidt,[14] which allows structural predictions to be made. In ionic oxide perovskites, the ions can be approximated by hard spheres and their ionic radii are well known.[15] The A and B-cations are separated by oxygen anions, hence the lattice constant can be expressed in terms of the ionic radii. For an ideal perovskite, we can identify by simple geometrical considerations

$$r_O + r_A = \sqrt{2}(r_O + r_B) \tag{2.1}$$

where the sum of the radii of oxygen r_O and the A-cation r_A is equal to the cubic lattice constant a. The sum of the radius of the B-site cation r_B and r_O is the face diagonal of one unit cell which is $\sqrt{2}$a. The Goldschmidt tolerance factor, defined as

$$t = \frac{r_O + r_A}{\sqrt{2}(r_O + r_B)}, \tag{2.2}$$

can be used to predict the structure if the radii are known. For t > 1 the A-cations are too large to fit in the interstitial sites. The B-O bonds are under tension but maintain the 180° bond angle. Hexagonal structures occur under these conditions. For a tolerance factor between 0.9 and 1.0, the ideal cubic perovskite structure is formed. $SrTiO_3$ being the best example. For a tolerance factor t = 0.71 – 0.9, orthorhombic and rhombohedral polytypes form. The A-cation is too small to fill the octahedral void, the structure responds with cooperative rotations of the $BO_{6/2}$ octahedra, leading to a reduction of the cubic $Pm\overline{3}m$ symmetry. Glazer[16] identified 15 possible tilt systems. The main axis of the tilt can be parallel to each of the crystallographic axis while the amplitude of each tilt may be different from the others. In addition, two adjacent layers stacked along the tilt axis may be tilted in phase or anti phase leading to a doubling of the unit cell in this direction.

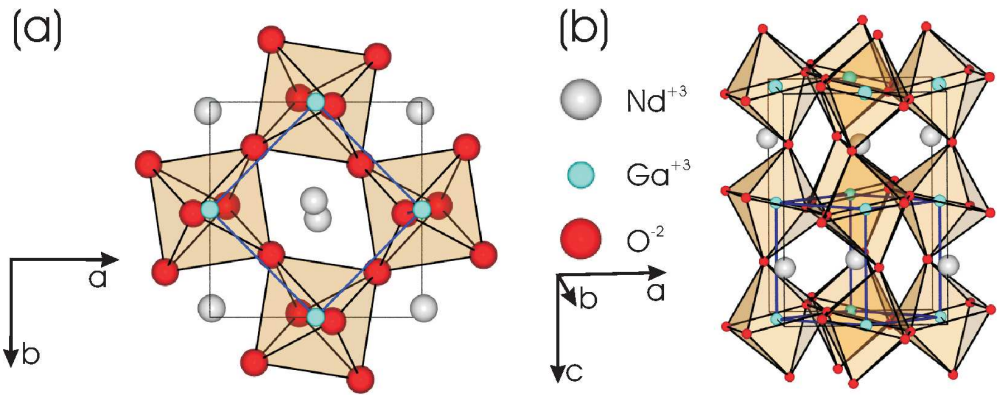

Figure 2.2.: $NdGaO_3$ crystallizes in a distorted perovskite structure. A truncated orthorhombic unit cell is shown in a projection (a) along the **c**-axis and (b) the **b**-axis revealing the cooperative rotations and tilts of the $GaO_{6/2}$ unit. The pseudo-cubic unit cell in shown in blue.

Examples of the orthorhombic structure are $NdGaO_3$, $LaGaO_3$ and $La_{(1-x)}Sr_xMnO_3$.[17] Figure 2.1.2(a) shows the distorted structure of $NdGaO_3$ along the orthorhombic **c**-axis; the rotations of the octahedra are clearly visible. The tilts of the octahedra can be seen in the side view along the **b**-axis, in Figure 2.1.2(b). The structure can be described in a pseudo-cubic coordinate system. In Figure 2.1.2, the pseudo-cubic cell is shown in blue. The structure of $LaGaO_3$ is very similar to $NdGaO_3$.

$La_{(1-x)}Sr_xMnO_3$ can be seen as a solid solution of the end members $LaMnO_3$ and $SrMnO_3$. It crystallizes in a distorted orthorhombic structure where the lattice constants vary with the cation concentration. $La_{0.7}Sr_{0.3}MnO_3$ has a *Pnma* symmetry. Qualitatively, the structure is very similar to $NdGaO_3$ and does not need to be discussed in more detail. The doped manganite systems exhibit an exceptionally rich variety of electronic and magnetic properties. Most outstanding being colossal magnetoresistance (CMR),[18,19] perfect spin polarization[20] and a metal/insulator transition above room temperature. The properties are strongly modified by doping (e.g. substitution of La by Sr). The end members $LaMnO_3$ and $SrMnO_3$ are antiferromagnetic insulators, but the optimally doped $La_{0.66}Sr_{0.33}MnO_3$ exhibits half-metallic conductivity and ferromagnetism. This makes manganites technologically interesting for spintronics applications.[21]

$LaAlO_3$ has a cubic high-temperature phase ($Pm\bar{3}m$, a=3.778 Å).[22] At ≈ 800 K it undergoes a structural phase transition into a rhombohedral low-temperature phase. The structure can also be referred to in a pseudo-cubic lattice, with a lattice constant of 3.790 Å. Recently, it has attracted a lot of interest due to the formation of a conducting interface with $SrTiO_3$.

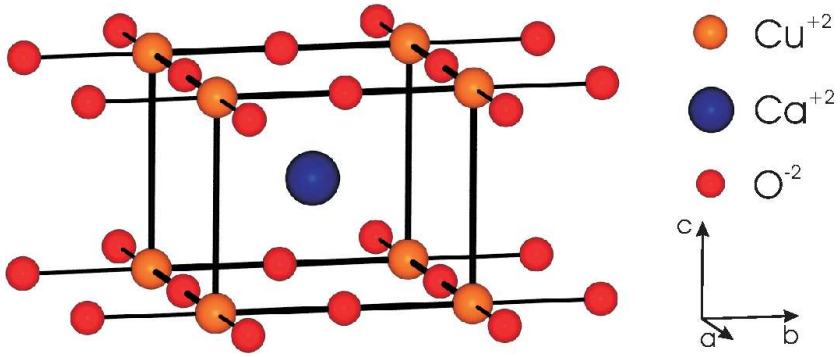

Figure 2.3.: $CaCuO_2$ crystal structure. A truncated tetragonal unit cell is shown. The structure consists of infinite layer $CuO_{4/2}$-planes separated by bare Ca^2+ ions.

The space groups, lattice parameters, and the lattice mismatch to $SrTiO_3$ are summarized in Table 2.1.

2.1.3. Infinite layer compounds

Another material with a crystal structure closely related to the perovskite structure is found in $CaCuO_2$ — the infinite layer structure. This tetragonal structure can be derived from the perovskite structure by the removal of oxygen from the AO-planes. This results in $CuO_{4/2}$ planes with Cu in fourfold planar coordination with oxygen ions.[23] In the $CaCuO_2$ structure these planes are separated by layers of bare Ca ions as shown in Figure 2.3. $CaCuO_2$ is an insulator with a 1.5 eV band gap, but the substitution of Ca ions by Sr ions can produce either narrow-band semiconducting and or even superconducting properties.[24]

The CuO_2 planes are thought to be the essential building block in high-temperature superconductors. Consequently, artificial heterostructures consisting of $CaCuO_2$ and other oxide materials like $BaCuO_2$,[25,26] and, more recently, $SrTiO_3$ and $La_{(1-x)}Sr_xMnO_3$[27,28] were studied by several groups and transition temperatures (T_C) as high as 80 K have been measured.

2.2. Sample preparation

The samples investigated were oxide thin films, or superlattice samples, grown either by PLD or MBE. PLD has been employed for the deposition of highly ordered $LaAlO_3$, $LaGaO_3$ and $NdGaO_3$ thin films, as well as superlattices of $CaCuO_2/SrTiO_3$ and $CaCuO_2/La_{0.65}Sr_{0.35}O_3$. MBE was used for the growth of oxygen-deficient $La_{0.65}Sr_{0.35}MnO_{3-\delta}$ thin films on $SrTiO_3$.

2.2.1. Pulsed-laser deposition

Pulsed laser deposition (PLD) has become a popular technique for thin film growth besides chemical vapor deposition, off-axis magnetron sputtering and MBE. An advantage of PLD is the stoichiometric transfer of the source material (target) to the substrate which makes PLD particularly interesting for the deposition of complex oxide materials containing many elements. A view into the PLD chamber in the SCL is shown in Figure 2.4. The target material is irradiated by focused UV-laser light pulses (KrF excimer laser wavelength λ=248 nm) leading to the formation of a dense plasma plume of ablated material. The condensation of the plasma takes place on the surface of a substrate positioned in the plume. The thermodynamic conditions in a PLD process are far from equilibrium, e.g. the partial pressures of the individual species in the plasma significantly exceed their equilibrium vapor pressures.

The film nucleation process is largely determined by the interfacial energies, the diffusion kinetics at the surface and the kinetic energy of the impinging plasma. A detailed study of the PLD deposition of $LaAlO_3$ was published by Aruta *et al.*[29] employing an ultra fast camera with chemical sensitivity. There are several reviews on PLD and the deposition of complex metal oxides available in the literature.[30–32]

2.2.2. Molecular beam epitaxy

The MBE technique was used by our collaborators in Trieste, Italy, for the deposition of stoichiometric $La_{0.65}Sr_{0.35}MnO_{3-\delta}$ (LSMO) films. The main advantage of the MBE technique in comparison to PLD is the high homogeneity of the deposited material over a relatively large distance of a few centimeters. There are several different types of evaporation sources available. In general the material to be deposited is heated in an evaporator mounted in a UHV chamber. The material will start to evaporate due to the increase of its vapor pressure at higher temperatures. The vapor beam propagates without a pronounced angular dependence.

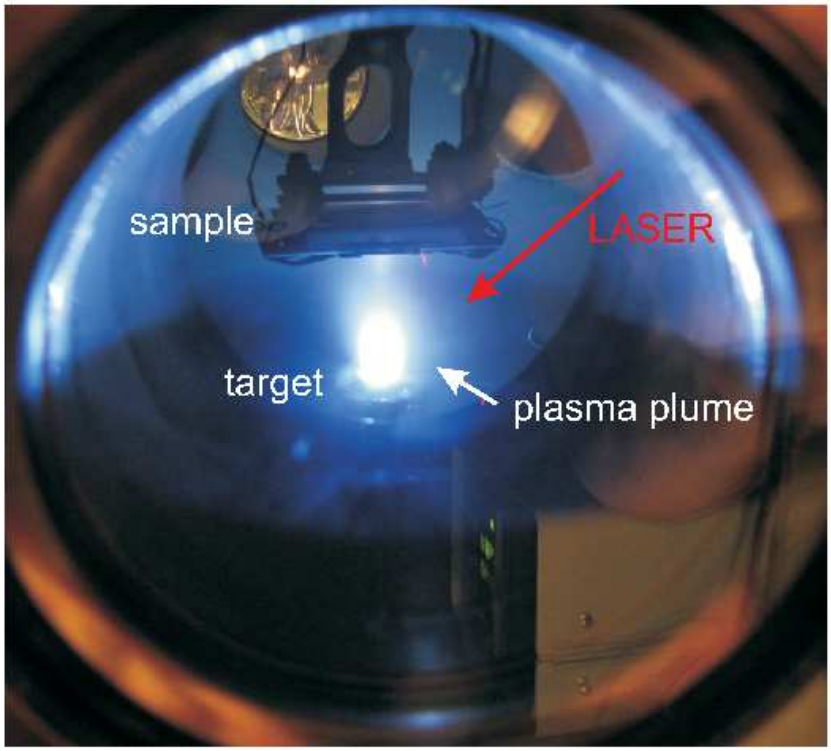

Figure 2.4.: View into the PLD chamber during $LaAlO_3$ growth. The beam path of the laser is schematically indicated by a red arrow. The absorption of the highly energetic laser pulses leads to the formation of a bright plasma plume. The plume points in the direction of the substrate which is mounted top-down on a resistive heater above the target.

An arrangement of apertures is used to produce a beam that is directed onto the sample while keeping contamination of the chamber to a minimum.

LSMO film growth was achieved by codeposition of La from an e^--beam evaporator and Sr and Mn from effusion cells. A high-purity metal source, a filament, pin holes and a flux meter are aligned on the same axis. The metal sources are heated by a filament. For the La e^--beam evaporator, a high voltage can be set between the La source and filament giving rise to electron bombardment. The emission current I_E is measured and typically in the range of tens of mA. Growth rates were typically in the range of 0.1Å/s.

In order to deposit stoichiometric LSMO films, three individual sources of La, Sr and Mn were aligned with the substrate and deposition rates carefully calibrated to match the desired sample stoichiometry. Oxygen stoichiometry was ensured by introducing a low partial pressure of oxygen (typically $\sim 2.66 \times 10^{-5}$ mbar) into the growth chamber.

2.3. Atomic force microscopy

AFM is a direct space imaging technique for the surface morphology. A very sharp tip with a typical curvature in the order of nanometers is used to produce a highly resolved image of the sample topography. In the most simple setup (contact mode), the surface is brought in the vicinity of the tip by high-precision piezoelectric elements. While approaching the surface, the tip starts to be deflected from its original position owing to interactions with the surface. This deflection is detected by the reflection of a laser, focused on the back of the tip, onto an array of photo diodes. According to Hooke's law, the deflection is related to a force. With the help of the piezo elements, the sample can be scanned under the tip (or vice versa). A feedback loop is set to keep the deflection signal constant during scanning. Two signals can now be used for imaging the sample. The current applied to the piezo for controlling the tip–sample distance can be converted directly into the height profile of the specimen. Another signal which gives good contrast is the deviation from the deflection setpoint.

In non-contact AFM, a piezo actuator is used to excite vibrations at the resonance frequency of the cantilever. The resonance frequency changes as a function of the tip–sample distance and can hence be used as a signal for creating an image of the sample topography. The mode can be of advantage for soft materials and films with weak adhesion, furthermore, the weaker interactions with the substrate increase the lifetime of the AFM-tip.

2.4. Diffraction of X-rays

In a general X-ray diffraction patterns result from coherent scattering of X-rays. The interaction of X-rays with matter can be separated into two basic processes. Radiation is either absorbed, or it is scattered with or without energy loss. We restrict ourselves to the latter process, i.e. the elastic scattering of X-rays. The atomic scattering factor f_a is the Fourier transform of the electron density distribution around one atom and describes the angular dependence of scattering. The scattering intensity from one unit cell or molecule is described by the sum of all individual scattering factors. Turning now to a crystal, described by the convolution of the 3-dimensional periodic lattice function with the electron density distribution of one unit cell, Fourier transformation yields the structure factor for the reflection $\mathbf{h}=(hkl)$

$$F_{\mathbf{h}} = \sum_{\nu}^{N} f_\nu e^{2\pi i \mathbf{h}\cdot\mathbf{r}_\nu} \tag{2.3}$$

where N is the number of atoms per unit cell, f_ν is the atomic scattering factor and $\mathbf{r}_\nu = (x_\nu, y_\nu, z_\nu)$ represents the coordinates of the ν-th atom. The intensity of a reflection is proportional to the square of $F_\mathbf{h}$.

$$\mathrm{I} \propto |F_\mathbf{h}|^2 \tag{2.4}$$

In this we can see the famous "phase problem" of X-ray crystallography. Only the amplitude of the structure factor is measured, but not the phase. There are some methods that allow to directly measure the phase, one of them is the XSW technique.

There are several factors that influence the measured intensity of a particular reflection: These are the absorption factor A, the Lorentz factor L, the polarization factor P and the extinction correction E.

$$I_\mathbf{h}^{obs} = ALPE|F_\mathbf{h}|^2 \tag{2.5}$$

In a simple picture, only waves with a phase shift of an integral number of wavelengths interfere constructively. This relation is expressed in Bragg's law.

$$\mathrm{n}\lambda = 2\mathrm{d}_\mathbf{h} \sin\theta \tag{2.6}$$

With the help of Bragg's law one can calculate, from the diffraction angle θ, the corresponding lattice plane distances $\mathrm{d}_\mathbf{h}$ for the reflection $\mathbf{h}$ and therefore, the lattice parameters of the crystal.

Diffraction is easier to handle in reciprocal space. The space is spanned by the three reciprocal vectors $\mathbf{a}^*$,$\mathbf{b}^*$, and $\mathbf{c}^*$. The reciprocal vector $\mathbf{a}^*$ is perpendicular to the (100)-plane and has a length of $\frac{1}{|\mathbf{a}|}$. In a similar way we can calculate the vectors $\mathbf{b}^*$ and $\mathbf{c}^*$. All lattice points can be described by linear combinations of the three vectors.

A geometrical representation of the scattering conditions can be made with the Ewald construction (see Fig. 2.5). The primary beam is described as the vector $\mathbf{k}_0$ and points to the origin of the reciprocal lattice. Its length is $\frac{1}{\lambda}$. Because $|\mathbf{k}_0| = |\ \mathbf{k}| = \mathbf{k}_0$, i.e. the wavelength remains unchanged during diffraction (elastic scattering), all diffracted beams come to lie on a circle with radius $\mathbf{k}_0$ which passes through the origin of the reciprocal lattice. Bragg's law (Eq. 2.6) is only valid for beams that come to lie on this circle. The scattering vector therefore points to a reciprocal lattice point to satisfy the diffraction condition. This point then has the indices (hkl).

For the scattering vector $\mathbf{h}$ we can write

$$\begin{aligned} \mathbf{h} &= h\mathbf{a}^* + k\mathbf{b}^* + l\mathbf{c}^* \\ \mathbf{h} &= \mathbf{k} - \mathbf{k}_0. \end{aligned} \tag{2.7}$$

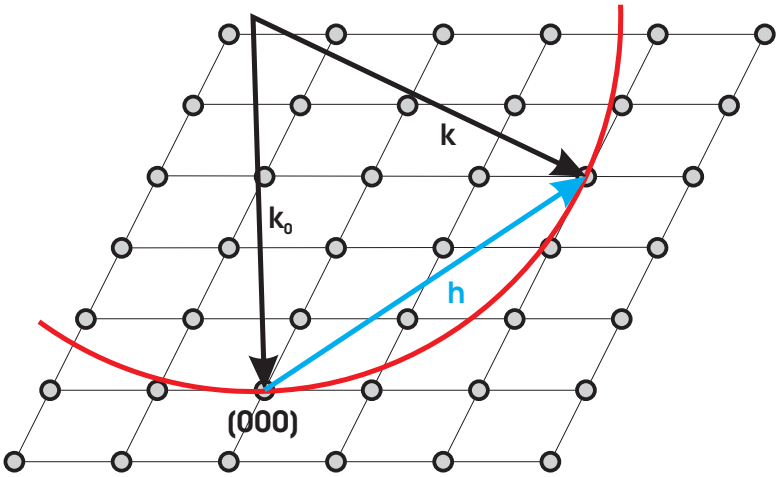

Figure 2.5.: A schematic drawing of the Ewald construction in reciprocal space. The incident wave vector $\mathbf{k}_0$ points to the origin of the reciprocal space. Bragg's law is valid for all lattice points that come to lie on the circle with radius $|\mathbf{k}_0|$ passing through the origin of reciprocal space.

The coordinates of a point (hkl) in reciprocal space are measured in reciprocal lattice units (r.l.u.). For a more detailed treatment see e.g. the description by Giacovazzo *et al.*[33]

2.4.1. Surface X-ray diffraction

In the past, X-rays were considered unsuitable for surface studies owing to their relatively weak interaction with matter. The contribution of the extremely small fraction of surface atoms compared to the total number of atoms in a bulk crystal gives rise to only a scarcely detectable contribution to the overall scattering of the sample. However, X-rays have developed as an important tool in surface structure determination. The weak interaction which limits the intensity gives rise to the important advantage that multiple and inelastic scattering can frequently be neglected in the structure determination. This makes structure determination easier and more straightforward. The development of special scattering geometries employing grazing incidence which, combined with strong X-ray sources and modern detectors provide sufficient intensities for measurements with short acquisition times.

The existence of a surface modifies the diffraction pattern from a crystal. Diffraction theory is usually applied to a perfectly ordered 3-dimensional periodic arrangements of atoms. However, at the surface, the periodicity is destroyed and

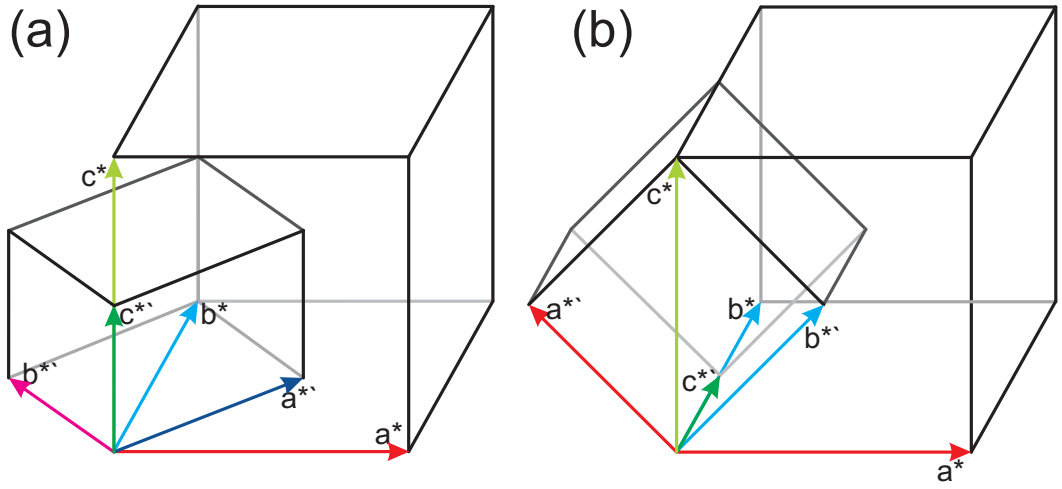

Figure 2.6.: Epitaxial growth of the orthorhombic perovskites, $LaGaO_3$ and $NdGaO_3$, on the cubic $SrTiO_3$ substrate can take place with (a) the **c**-axis aligned out-of plane or (b) in-plane.

this gives rise to the so-called crystal truncation rods (CTR). Bragg reflections become extended along ℓ, producing intensity between Bragg points. According to the exact theoretical description, the intensity of the CTR, in the middle between two Bragg points, will be $\sim 10^{-5}$ times the intensity of a strong Bragg reflection.[34]

2.4.2. Transformation of coordinates

A major part of this work focuses on perovskite thin films grown on $SrTiO_3(001)$ substrates. The different compounds may have a lower symmetry and different unit cell dimensions than the substrate (see Table 2.1). The orientation of the overlayer with respect to the substrate lattice is defined by the alignment of the oxygen sublattices. For the orthorhombic perovskites $LaGaO_3$ and $NdGaO_3$ the possible alignment of the lattice vectors is schematically shown in Figure 2.6. In the orthorhombic crystal system the lattice vectors **a**, **b** and **c** are not equivalent. The simplest case is for the long **c**-axis parallel to the **c**-axis of the substrate. This is illustrated in Figure 2.6(a) and is giving rise to a $(\sqrt{2} \times \sqrt{2})R45°$ superstructure. Another possibility is for the **c**-axis to be oriented in-plane, parallel to the $SrTiO_3$ **a** or **b**-axis. This leads to the **a** and **b**-axis pointing out-of-plane (see Fig. 2.6(b)). The resulting superstructure is a (2×1) superstructure that, due to substrate symmetry, it is observed as a two-domain superstructure.

The transformation matrix **M** is defined by the scalar products of the vectors spanning the substrate and thin film coordinate system. The transformation is

performed by solving

$$\begin{pmatrix} \mathbf{a}' \\ \mathbf{b}' \\ \mathbf{c}' \end{pmatrix} = \mathbf{M} \cdot \begin{pmatrix} \mathbf{a} \\ \mathbf{b} \\ \mathbf{c} \end{pmatrix}. \tag{2.8}$$

For the transformation of pseudo cubic to orthorhombic coordinates the following matrix $\mathbf{M}$ was applied for the $\mathbf{c}$-axis out-of-plane

$$\begin{pmatrix} \mathbf{a}^{*'} \\ \mathbf{b}^{*'} \\ \mathbf{c}^{*'} \end{pmatrix} = \begin{pmatrix} 1/2 & 1/2 & 0 \\ 1/2 & -1/2 & 0 \\ 0 & 0 & 1/2 \end{pmatrix} \times \begin{pmatrix} \mathbf{a}^{*} \\ \mathbf{b}^{*} \\ \mathbf{c}^{*} \end{pmatrix} \tag{2.9}$$

and for the $\mathbf{c}$-axis oriented in-plane

$$\begin{pmatrix} \mathbf{a}^{*'} \\ \mathbf{b}^{*'} \\ \mathbf{c}^{*'} \end{pmatrix} = \begin{pmatrix} 1/2 & 1/2 & 0 \\ 0 & 0 & 1/2 \\ 1/2 & -1/2 & 0 \end{pmatrix} \times \begin{pmatrix} \mathbf{a}^{*} \\ \mathbf{b}^{*} \\ \mathbf{c}^{*} \end{pmatrix}. \tag{2.10}$$

The reciprocal lattice vectors $\mathbf{a}^{*\prime}$, $\mathbf{b}^{*\prime}$ and $\mathbf{c}^{*\prime}$ describe the orthorhombic cell and the $SrTiO_3$ lattice vectors are described by $\mathbf{a}^*$, $\mathbf{b}^*$ and $\mathbf{c}^*$.

From Figure 2.6 it becomes clear that, due to the fourfold substrate symmetry, 4 symmetrically equivalent domains of each orientation can coexist. The additional superstructure reflections should be observable in the half integer positions by SXRD.

2.5. Hard X-ray photoelectron spectroscopy

X-ray photoelectron spectroscopy is an important tool to study the electronic structure of molecules and solids and is a widely used surface analytical technique.

Depending on the photon energy one distinguishes: (i) UPS for the ultraviolet range (5 to 100 eV), (ii) SXPS for the soft X-ray regime (100 to 1000 eV) and (iii) for higher energies XPS. In recent years the interesting insights revealed by higher photon energies lead to the term HAXPES for photon energies above 2–3 keV. The main differences are the increased binding energy (E_B) range and maximum probing depth. This makes HAXPES particularly interesting for the study of buried interfaces. One drawback is, however, the decrease in count rate due to the rapidly diminishing photoionization cross sections[35] and the poor energy resolution (using standard monochromators) at higher photon energies. However, it should be mentioned that at modern synchrotron sources much better energy resolution (down to 50 meV above 6 keV) than with traditional XPS can be achieved, which is another reason for the success of HAXPES.

The following introduction into the principles of the photoemission process follows the descriptions by Hüfner[36] and Fadley.[37]

2.5.1. General principles

The sample to be analyzed is irradiated by photons of energy $h\nu$. Electrons are ejected by the photoelectric effect from core levels and subsequently analyzed by an electron spectrometer. The data are then presented as a graph of intensity versus electron energy (binding energy). In a first approximation, the electronic states of a sample are measured in this way.

The actual experimental quantity measured by the spectrometer is the kinetic energy (E_{kin}) of the electrons. Its value depends on the photon energy of the X-ray source and is therefore not an intrinsic material property. The more relevant measure is the binding energy E_{B},

$$E_{\mathrm{B}} = h\nu - E_{\mathrm{Kin}} - W \tag{2.11}$$

where W is the work function of the spectrometer. Theoretically, all the parameters mentioned on the right hand side of Eq. 2.11 are known or can be measured so that E_{B} can be determined precisely.

The excitation process requires the absorption of a photon of energy hν by an atom with N electrons. Generally, the photoelectron is only weakly coupled to the (N−1) ion. The final state can then be separated leading to

$$\psi^i(N) \xrightarrow{h\nu} \psi^f(N-1) + \Phi^f(1)\chi^f(1) \tag{2.12}$$

where $\psi^i(N)$ and $\psi^f(N-1)$ are the wave function of the atom/ion prior and after the ionization process and $\Phi^f(1)$ and $\chi^f(1)$ are the spatial and spin part of the photoelectron wave function.

The transition probability from the initial state to the final state can be calculated from Fermi's Golden rule within first-order perturbation theory

$$w \propto \frac{2\pi}{\hbar}|\langle\psi^f|\ \mathbf{H}|\psi^i\rangle|^2\delta(E^f - E^i - \hbar\nu) \tag{2.13}$$

where E^f and E^i are the final and initial state energies and $\mathbf{H}$ is the perturbation operator

$$\mathbf{H} = \frac{1}{m_e c}\mathbf{A}\cdot\mathbf{p} \tag{2.14}$$

which describes the interaction of the electrons with the electromagnetic field $\mathbf{A}$ and the generalized momentum operator $\mathbf{p} = -i\hbar\nabla$. The phase factor of

single electromagnetic wave $\mathbf{A} = A_0 e^{-2\pi i \mathbf{k}\cdot\mathbf{r}}$ can be expanded in a Taylor series as $e^{-2\pi i \mathbf{k}\cdot\mathbf{r}} = 1 - 2\pi i \mathbf{k}\cdot\mathbf{r} + \pi i (\mathbf{k}\cdot\mathbf{r})^2 - \ldots$. In the dipole approximation this expression is simplified under the approximation that $e^{-2\pi i \mathbf{k}\cdot\mathbf{r}} \sim 1$. That means that only the first-order term is considered and $\mathbf{A} = A_0$. The simplification may give incorrect results and hence higher order terms may be needed.

The considerations presented so far make use of a fundamental simplification, the so-called sudden approximation. It is assumed that the orbitals of the N−1 final state system are the same as in the initial state ($\psi^i(N-1) = \psi^f(N-1)$). This does not generally hold. Intuitively, one would expect that the system after ejection of an electron relaxes in a way to minimize its energy. In a more complete approach, one has to sum over all possible excited final states

$$\langle \psi^f | \mathbf{H} | \psi^i \rangle = \langle \phi^f_{E_{kin}} | H | \phi^i_k \rangle \sum_s c_s \tag{2.15}$$

with

$$c_s = \langle \psi^f_{s,k}(N-1) | \mathbf{H} | \psi^i_{R,k}(N-1) \rangle \tag{2.16}$$

with c_s being the probability for an electron in the ground state ϕ^i_k to be emitted in the excited state $\psi^f_{s,k}(N-1)$. Here k is a running subscript for the different orbitals in the system. For $s = k$ we observe the principal line. Especially in strongly correlated systems, there can be a significant probability for s≠k transitions.

The intensity I can now be written as follows

$$I \propto \sum_{f,i,k} |\langle \psi^f_{E_{kin}} | \mathbf{H} | \psi^i \rangle|^2 \sum_s |c_s|^2 \delta(E^f + E_s(N-1) - E_0(N) \hbar\nu) \tag{2.17}$$

where $E_0(N)$ is the ground state energy. Hence, the photocurrent shows main lines corresponding to the photoionization of the orbitals k, and a number of satellite features for the excited states s of the orbital k.

For solid samples, another formalism, using the spectral function A(k,E), is more useful. The spectral function is related to the single particle Green function G(k,E) by

$$A(k, E) = \pi^{-1} \mathrm{Im}\{G(k, E)\}. \tag{2.18}$$

With this, we find a new expression for the photocurrent

$$I \propto \sum_{f,i,k} |\langle \psi^f_{E_{kin}} | \mathbf{H} | \psi^i \rangle|^2 A(k, E). \tag{2.19}$$

A more detailed treatment of the theory of photoemission can be found in Hüfner[36] and Fadley[37] and the references therein.

The observed photoelectrons are described in the scheme nl_j with respect to their quantum numbers. The principal quantum number n takes integer values starting from 1, the orbital angular momentum l is given a letter ($0\rightarrow s$, $1\rightarrow p$, $2\rightarrow d$, $3\rightarrow f$). The quantity j is a vector addition of the spin and orbit angular momentum $j = |l + s|$. For a p orbital we thus get j of $1/2$ for $l - s$ or $3/2$ for $l + s$. Similarly, for d-orbitals we can have $3/2$ and $5/2$.[38]

2.5.2. Core levels and final states

The binding energies of the core levels provide direct information about the chemical composition and bonding in solids. Even more detailed information on the electronic properties of the samples can be obtained by studying the fine structure of the core level peaks. Typically, one can observe modifications such as shifts of the core level position, additional peaks or peak broadening. In the following, a few of the most frequently encountered effects will be explained. They can be classified as either initial state and final state effects. In the case of initial state effects, the state on the atom prior to photoemission plays the major role e.g. the chemical shift observed due to a valence change. Final-state effects occur as a response of the system to the emission process. Such effects are core hole screening, relaxation of electron orbitals and/or shake-up satellites.

Chemical shift Already in the first photoemission experiments by Kai Siegbahn and coworkers,[39] it was found that the core levels in different compounds exhibit relative binding energy shifts characteristic for the chemical environment of the emitting atom or ion. Generally, a reduction of the oxidation state of a metallic atom typically results in a $\sim$1 eV shift to higher binding energy.

Spin-orbit coupling Orbitals with an angular momentum greater than 0 (i.e. p, d, f, ...) show splitting due to interactions of the electron spin with the orbital angular momentum. This leads to the formation of characteristic doublets with two components.

The relative intensity of the components depends on the degeneracy (relative population) of the orbital. The degeneracy is given by (2j+1), consequently, for a $3d$ orbital we get an intensity ratio of (2×3/2+1):(2×5/2+1)=2:3 for the $3d_{3/2}$ and $3d_{5/2}$ components respectively. Similarly for $2p_{1/2}$ and $2p_{3/2}$ we expect a 1:2 ratio. These physical constraints are useful to minimize the number of free parameters when fitting XPS spectra.[38]

The spacing between the components depends on the strength of the spin orbit coupling. For a given atom, it increases with decreasing n and j. Thus, deeper core levels show a stronger splitting.

Exchange splitting Compounds with unpaired valence electrons may show exchange splitting. This is the case, for example, for the $3s$ core levels of Mn and Cr, the $2p_{3/2}$ of Co and Ni and the $4s$ levels of the rare earths.

In the case of Mn $3s$, the two states arise due to $3d$-$3s$ exchange interaction after photoionization: (i) a high-spin state at lower E_{B} with the spins of the $3s$ and the $3d$ electrons parallel and (ii) a low-spin state at a higher E_{B} with anti-parallel spin alignment. The size of the exchange splitting observed in the Mn $3s$ core level spectra has a linear dependence on the Mn oxidation state.[40,41] This is expressed in the relationship $\Delta E = (2S+1)J^{eff}_{3s-3d}$, where S is the total spin moment and $\mathrm{J}^{\mathrm{eff}}_{3s-3d}$ the effective exchange integral between Mn $3d$ and $3s$ states.

Shake-up and shake-off satellites Shake-up satellites are a multielectron response involving the interaction of an emitted core electron with electrons from outer shell subbands. In a shake-up satellite the emitted electron excites the second electron to a higher bound state. In a shake-off satellite, the second electron in emitted to the continuum. These interactions require an energy transfer to the second electron and thus lead to a satellite structure at the high binding energy side of the main line. The intensity contribution to a core level line can account for 20% of the total photoelectron yield. A well known example are the Cu $2p$ core-level shake-up satellites.

Screening in transition metals Screening features can be found in many transition metals and transition metal oxides like the nickelates, cuprates and manganates.[42–44] The interest in these features grew recently because many of them are only observable by HAXPES. This finding indicates that the process leading to their formation requires a larger excited volume to develop than is usually probed by XPS.

It was shown by Horriba *et al.*[42] that the LSMO Mn $2p$ core level exhibits a low binding energy feature $-1\,\mathrm{eV}$ below the main line. This feature can be explained by a screening effect of the Mn core hole. In general, the core hole will be screened by electrons from neighboring atoms. We can write this process as $2p3d^n \rightarrow 2p3d^{n+1}\,\underline{\mathrm{L}}$ where $\underline{\mathrm{L}}$ denotes a hole in the oxygen $2p$ orbitals.

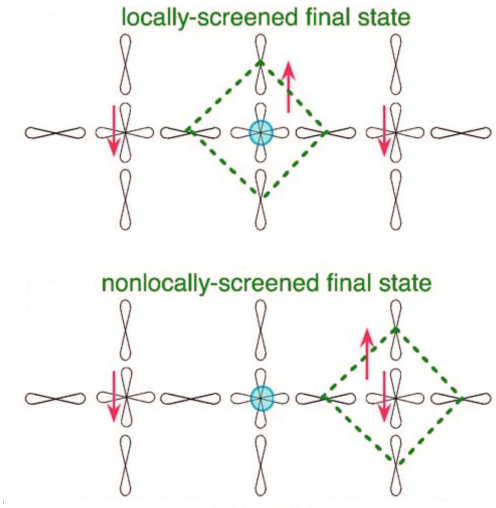

Figure 2.7.: Local and non-local screening of a Cu $2p$ core hole. Shown are the x^2-y^2 orbitals of Cu and the σ-bonding p-orbitals of oxygen. Figure taken from Ref.[43]

In many cuprates the Cu $2p$ spectra show multiple peaks that can be explained in terms of core hole screening by the valence electrons. The screening is predominantly facilitated by the Cu $3d$ and O $2p$ orbitals, which modify the binding energy of the photoelectrons. Following the work of Michel van Veenendaal,[43] two screening channels can be distinguished as shown in Figure 2.7. The core hole can be screened by electrons from the oxygen atoms surrounding the site with the core hole, known as a local screening process or the core hole can be screened by electrons from the ligand atoms surrounding a neighboring CuO_4 plaquette, known as a non-local screening. This gives rise to a Zhang-Rice singlet (ZRS) on a neighboring CuO_4 plaquette.

2.5.3. Depth selective measurements

Photoelectron spectroscopy with high energy X-ray beams provides large probing depths. The probing depth is defined as 3 times the inelastic mean free path (IMFP) λ and refers to the depth that accounts for 95% of the photoelectron intensity. The intensity can be estimated by integrating the Beer-Lambert equation from the surface to a depth d

$$I = I_0 \exp^{\frac{-d}{\lambda \sin\theta}} \tag{2.20}$$

where λ is the inelastic mean free path of the electron in the material A, I_0 is the intensity measured on an infinitely thick sample and θ is the electron take-off angle. The IMFP λ is a material constant and can be estimated experimentally

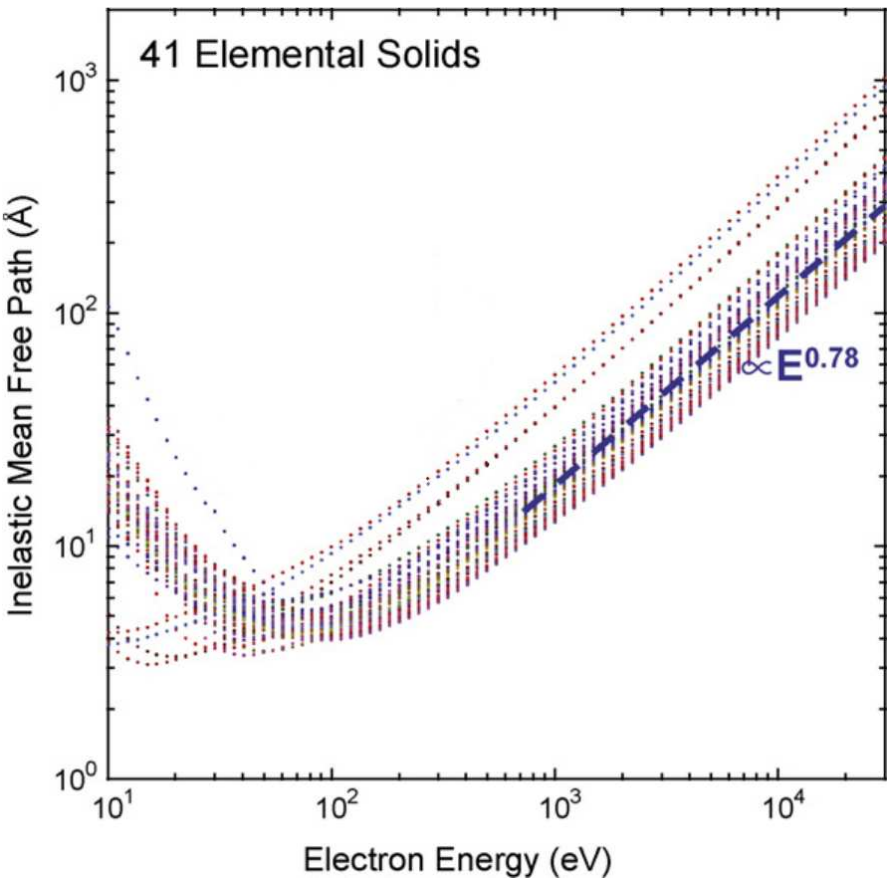

Figure 2.8.: Plot of the mean free path of electrons in the range of 0 to 15 keV as estimated from the TPP-2M equation. The mean free path is in the order of only a few Å for energies of a few 100 eV. At higher energies the variation as can be reasonably approximated as indicated by the thick dashed line. The figure is modified from Tanuma *et al.*[46]

or calculated by a predictive formula (TPP-2M).[45] For typical values of λ (e.g. 2nm at 6 keV), probing depths of above 6 nm are easily accessible. The variation of the IMFP as a function of E_{kin} is shown in Figure 2.8. A minimum IMFP is found for kinetic energies in the range of 100 eV, for higher energies a reasonable approximation can be made via $\lambda = E_{kin}^{0.78}$. This estimate is not accurate because it does not take elastic scattering events into account which is the reason that the real escape depth can be significantly smaller than the IMFP. However, in this context, it is important that elastic scattering is less pronounced at higher electron kinetic energies.

In many cases, it may be interesting to vary the probing depth during an experiment to localize the origin of specific features in the XPS spectrum. Several methods achieve their depth sensitivity by controlled removal of material from the surface e.g. by ion milling. The downside of these methods is the destruction

of the specimen and possible introduction of artifacts due to disorder due to ion bombardment, preferential sputtering of different components of the sample and unknown sputtering rates. Nevertheless, there are non-destructive methods available.

To achieve depth sensitivity in photoelectron spectroscopy, the effective probing depth must be changed. This can be achieved by variation the take-off angle or the excitation energy. If we consider a thin homogeneous film of material A with a thickness d on a flat substrate of material B. The intensity from A can be estimated from

$$I_A = I_A^{\infty} \left[1 - \exp^{\frac{-d}{\lambda_{A,A} \sin\theta}} \right] \tag{2.21}$$

where I_A^{∞} is the intensity for an infinitely thick overlayer and $\lambda_{A,A}$ is the IMFP for the electron from A in A. The decrease in the X-ray intensity can be neglected due to the comparatively small absorption coefficients.

The intensity, I_B^{∞}, of the substrate electrons arriving at the interface is attenuated by the film. $\lambda_{B,A}$ is the mean free path of the electrons from substrate B in the film A.

$$I_B = I_B^{\infty} \exp^{\frac{-d}{\lambda_{B,A} \sin\theta}} \tag{2.22}$$

There is some confusion in the definition of the angles in XPS although there exists an international standard, ISO 18115. The angle of emission is measured with respect to the surface normal and the take-off angle is measured with respect to the surface plane. This angle is varied by the *vth* motor of the manipulator in the main HAXPES chamber.

2.6. X-ray standing waves

The introduction to the basic principles of the XSW technique partially follows the descriptions given by Woodruff[47] and Zegenhagen.[48]

2.6.1. Basic concepts

The XSW technique makes use of the interference of the incoming and reflected beam under Bragg or total reflection conditions. While scanning the incident beam energy through the reflection range of the crystal, photoelectron or X-ray fluorescence spectra are collected together with the intensity of the reflected beam.

The spectra show an intensity modulation related to the crystallographic site of the emitting atoms.

The standing wave field extends into the crystal but also covers the whole volume above the crystal surface in which the two beams overlap. The wave field intensity has a sinusoidal modulation with the periodicity of the scattering planes ($\lambda = 2d$) and the intensity varies between 0 and 4 times that of the incident beam. Analysis in the framework of dynamical theory of diffraction shows that due to backscattering events there is a finite penetration of the beam in the crystal and hence the angular or energy range in which the reflection occurs are finite (Darwin width). It is known that the wave field can be moved through the unit cell by scanning through the Bragg reflection by varying either the photon energy or the angle.

The fundamental equation describing the experiment defines the intensity variation of the XSW relative to the lattice plane $d_{\mathbf{h}}$.

$$I_{\mathbf{h}}/I_0 = |1 + \left(\frac{E_{\mathbf{h}}}{E_0}\right) \exp(-2\pi i \frac{z}{d_{\mathbf{h}}}))|^2 \tag{2.23}$$

The ratio of the scattered electromagnetic wave amplitude to the amplitude of the incident electromagnetic wave E_H/E_0 is related to the reflectivity, R, via

$$\frac{E_{\mathbf{h}}}{E_0} = \sqrt{R_{\mathbf{h}}} \exp(i\nu) \tag{2.24}$$

where $i\nu$ is a phase factor. Hence, we can write

$$I_{\mathbf{h}} = 1 + R_{\mathbf{h}} + 2\sqrt{R_{\mathbf{h}}} \cos(\nu_{\mathbf{h}} - 2\pi \frac{z}{d_{\mathbf{h}}}). \tag{2.25}$$

Processes like photoelectron emission and X-ray fluorescence are excited with a probability proportional to the electric field intensity $Y_{\mathbf{h}} \propto I_{\mathbf{h}}$. The photoelectron or fluorescence yield Y_h detected in a real experiment is excited from N atoms with distribution due to vibrational, or static, disorder and/or several sites. We can write

$$\begin{aligned} Y_{\mathbf{h}} &\propto 1 + R_{\mathbf{h}} + 2\sqrt{R_{\mathbf{h}}} \frac{1}{N} \sum_{j=1}^{N} \cos(\nu_{\mathbf{h}} - 2\pi \frac{z_j}{d_{\mathbf{h}}}) \\ Y_{\mathbf{h}} &\propto 1 + R_{\mathbf{h}} + 2\sqrt{R_{\mathbf{h}}} f_{\mathbf{h}} \cos(\nu_{\mathbf{h}} - 2\pi P_{\mathbf{h}}) \end{aligned} \tag{2.26}$$

with the coherent position $P_{\mathbf{h}}$ being the average phase of the N atoms and the coherent fraction $f_{\mathbf{h}}$ describing the spread of the atomic distribution perpendicular to the scattering planes.

The reflectivity $R_{\mathbf{h}}$ and phase $\nu_{\mathbf{h}}$ of the XSW field can be calculated from the dynamical theory of diffraction.[49] Consequently, the coherent position P_H and the coherent fraction $f_{\mathbf{h}}$ can be obtained by fitting Eq. 2.26 to the experimental photoelectron yield curves. These two quantities are the amplitude $f_{\mathbf{h}}$ and phase $P_{\mathbf{h}}$ of one Fourier coefficient of the elemental atomic distribution function $\rho(r)$.

There are fundamental differences between the data measured by XSW and the X-ray structure factor $F_{\mathbf{h}}$ (see Eq. 2.3) measured in a diffraction experiment. The scattering amplitude $A(\mathbf{h})$ of a crystal is defined as the sum of the structure factors for all unit cells participating in the scattering process.

$$A(\mathbf{h}) = F_{\mathbf{h}} \sum_j \exp^{2\pi i \mathbf{h}\cdot\mathbf{R}_j} \tag{2.27}$$

where $\mathbf{R}_j$ is a vector pointing to the jth unit cell.

The $f_{\mathbf{h}}$ and $P_{\mathbf{h}}$ values obtained from Eq. 2.26 for an element μ can be related to the X-ray scattering amplitude by

$$f_{\mathbf{h}} = N^{-1} f_\nu^{-1} |A(\mathbf{h})| \tag{2.28}$$

$$2\pi P_{\mathbf{h}} = \varphi_\mu \tag{2.29}$$

where f_ν is the atomic form factor. The elemental scattering amplitude $A_\mu(\mathbf{h}) = |A_\mu(\mathbf{h})| \exp^{-\varphi_\mu}$ and analog the total scattering amplitude is $A(\mathbf{h}) = |A(\mathbf{h})| \exp^{-\varphi}$. In a X-ray diffraction experiment, we determine the absolute value of the total scattering amplitude of the electron density $A(\mathbf{h})$ whereas, with XSW, we determine the element specific amplitude of the atomic density $A_\mu(\mathbf{h})$ and the phase φ_μ.

2.6.2. Site-specific deconvolution

Site-specific decomposition of the valence band using XSWs in combination with HAXPES offers a unique way to gain a deeper understanding of the bonding and conduction mechanisms in correlated oxides. It was performed the first time on rutile TiO_2[7] and revealed the partial densities of states (p-DOS) for Ti and O. In a previous study, the valence band for a lightly annealed $SrTiO_3$ single crystal[9] was decomposed into the partial contributions from Sr, Ti and O.

The high spatial sensitivity of the XSW technique in conjunction with PES arises from the fact that the photoabsorption happens virtually at the center of the atom, which is understood within the framework of the dipole approximation (DA). The DA is essentially valid even for HAXPES of valence or conduction electrons, which was convincingly demonstrated by the site-specific photoemission of copper

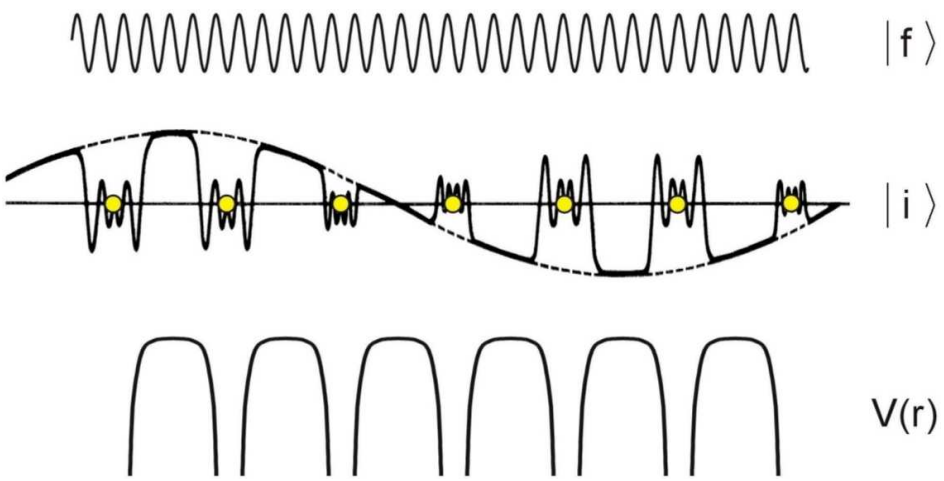

Figure 2.9.: The wave functions of the photoelectron final state $|\langle\psi^f|$ and initial state $|\psi^i\rangle$ are sketched schematically together with the crystal potential V(r). Strong interactions occur only in the region where V(r) has a large gradient, namely close to the atomic core. Figure taken from Thieß.[51]

conduction band electrons.[50] The volume in which photoelectron emission can effectively occur is limited to a small region around the atomic cores in which the overlap integral of the spatially dependent functions $\langle\psi^f|$, $|\psi^i\rangle$ and V(r) is non-zero. This can be seen from the schematically sketch in Figure 2.9 which shows the crystal potential V(r) created by the periodic arrangement of atomic cores in the lattice. Large gradients are observed only in the vicinity to the cores. $|\psi^i\rangle$ is the wave function of the initial state of a valence electron. It overlaps significantly with the rapidly oscillating final state wave function $\langle\psi^f|$ in the vicinity of the atomic cores while the quasi-free electron in between the cores does not participate in the photoexcitation process. One can see from this that electron from the valence band should be emitted from the same volume in the unit cell. This means that we cannot measure something like a "delocalized" electron gas.

In photoelectron spectra of valence bands and Fermi levels the relative contributions of the different elements in the sample cannot easily be distinguished. However, by employing some simple considerations, the contributions from different lattice sites can be recovered.

The total photoelectron yield of a valence band can be approximated by

$$Y(E,h\nu) = \sum_j Y_j(E,h\nu) \propto \sum_j Y_j^{Obs}(E,h\nu) \times A_j(E,h\nu) \quad (2.30)$$

$$Y_j^{Obs}(E,h\nu) \propto \sum_k \rho_{jk}(E) \times \sigma_{jk}(h\nu) \times [1-\beta_{jk}(h\nu)] \quad (2.31)$$

where E and hν are the binding energy and photon energy. j indexes the different elements in the unit cell and k the different subshells of each element. Here, Y_j is the XSW-modulated partial yield and Y_j^{Obs} is the off-Bragg partial yield of element j. ρ, σ and β are the (angular-momentum resolved) partial density of states, photo-ionization cross section and dipole parameter, respectively. A_j is the XSW field intensity experienced by element j (when element j occupies multiple positions, A_j represents the XSW intensity averaged over all positions).

In the analysis, we take advantage of the fact that A_j is proportional to a core level yield of element j, which can be measured experimentally. However, since the proportionality factor varies from element to element, the measured core level yields must be normalized (to their off-Bragg yields) before one can apply Eq. 2.30.

Without the help of theoretical lp-DOS, XSWs may allow one to separate the data into the (off-Bragg) partial yields of the individual elements using Eq. 2.30. If there are N elements in the unit cell and the VB XSW measurement contains M photon-energy steps around a Bragg reflection, Eq. 2.30 represents a system of M linear equations of N unknowns Y_j^{Obs} for any fixed binding energy E:

$$\begin{aligned} Y(E,h\nu_1) &= Y_1^{Obs}(E)\,A_1(h\nu_1) + Y_2^{Obs}(E)\,A_2(h\nu_1) + \ldots + Y_N^{Obs}(E)\,A_N(h\nu_1) \\ Y(E,h\nu_2) &= Y_1^{Obs}(E)\,A_1(h\nu_2) + Y_2^{Obs}(E)\,A_2(h\nu_2) + \ldots + Y_N^{Obs}(E)\,A_N(h\nu_2) \\ &\ldots \\ Y(E,h\nu_M) &= Y_1^{Obs}(E)\,A_1(h\nu_M) + Y_2^{Obs}(E)\,A_2(h\nu_M) + \ldots + Y_N^{Obs}(E)\,A_N(h\nu_M) \end{aligned} \tag{2.32}$$

Y_j^{Obs} can be considered as constant over the narrow photon energy range of the XSW scans. The N unknowns Y_j^{Obs} may be solved if $N \leq M$.

The site-specific partial yield cannot be directly translated into individual partial DOS because the exact site-specific cross sections near E_F are normally unknown.

2.6.3. Real space imaging

In contrast to standard X-ray diffraction measurements, in XSW measurements the amplitude *and the phase* of the Fourier coefficients are determined for each reflection. Consequently, the phase problem does not apply to XSW. This means that if a sufficient number of Fourier components are known, the atomic distribu-

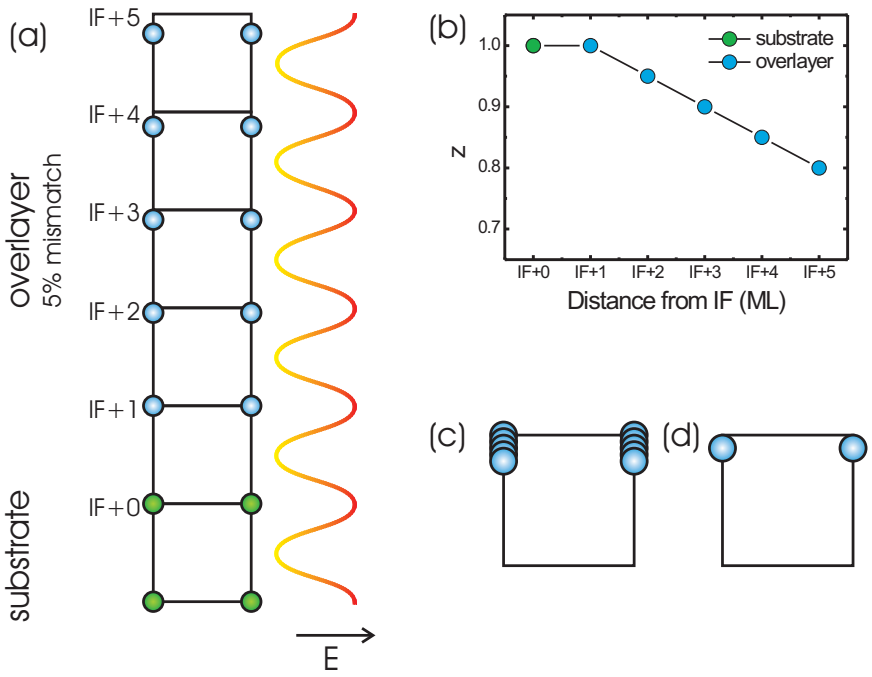

Figure 2.10.: (a) Schematic of a crystalline overlayer (blue circles) with a lattice constant 5% smaller than the substrate (green circles) in **c**-direction. (b) The atoms in the overlayer have a linear displacement with respect to the substrate lattice as function of their distance from the interface (IF). In the real space images the overlayer positions (c) are folded back into the substrate unit cell and, hence, an average position (d) is measured.

tion function, $\rho(r)$, can be reconstructed by solving

$$\rho(r) = \frac{1}{\mathrm{V}_{uc}} \left(1 + 2 \sum f_{\mathbf{h}} \cos\left[2\pi(P_{\mathbf{h}} - \mathbf{h} \cdot \mathbf{r})\right]\right) \tag{2.33}$$

where V_{uc} is the unit cell volume and $\mathbf{r}$ the real space coordinates (x,y,z).

In the XSW technique it is important to understand how the structural information from different sites is combined. The largest distances that can be probed are defined by the lattice constants of the substrate. Thus, real space images contain the atomic density of the probed volume folded back into the unit cell of the substrate. Figure 2.10(a) shows a schematic of several monolayers (MLs) of a crystalline material with a 5% mismatch of the out-of-plane lattice constant compared to that of the substrate. In this case, the atoms in the overlayer have a linearly increasing displacement as a function of their distance from the interface (IF) as shown in Figure 2.10(b). In the real space image, all positions in the overlayer are folded back into the substrate unit cell as indicated in Figure 2.10(c).

Therefore, the measured position is the average of all overlayer positions (see Fig. 2.10(d)).

The XPS lines from different sites may overlap and a deconvolution of the individual components may not be possible. The measured XSW structure factor can contain contributions from two sites. This situation may occur for oxide thin films grown on oxide substrates. In this case, the measured Fourier components ($f_{\mathbf{h}}$, $P_{\mathbf{h}}$) can be decomposed into a sum of the contributions from film (A) and substrate (B) using the standing wave structure factors in their complex form $G_{\mathbf{h}} = f_{\mathbf{h}} \exp(2\pi i P_{\mathbf{h}})$ in the following way

$$G_{\mathbf{h}\mathrm{exp}} = G_{\mathbf{h},A} \times c + G_{\mathbf{h},B} \times (1 - c) \tag{2.34}$$

where $G_{\mathbf{h},exp}$ is the experimentally measured structure factor, $G_{\mathbf{h},A}$ and $G_{\mathbf{h},B}$ are the structure factors from the film and the substrate and c is the relative contribution from the film to the measured photoelectron yield. The substrate contribution to the signal can be subtracted to obtain the corrected Fourier coefficients.

The main advantages of the XSW real space imaging technique is that the atomic density distribution is recovered without any assumptions. This means that there are no fitting or modeling steps involved, as it is necessary in most diffraction based techniques. The reason for this arises from the element specificity of the XSW technique. Moreover, the element specific measurements have another advantage, namely the high sensitivity to all elements independent of their atomic number Z. This allows one to analyze dilute systems or compounds where the constituting atoms have very similar Z.

The third attractive feature is the high spatial resolution achieved in XSW measurements. The error bar on the extracted atomic positions is defined by the smallest lattice spacing used for the imaging. Commonly, the error of a XSW measurement is in the range of 1-2%, which gives for the imaging presented here, a precision in the order of 0.02Å.

Model refinement

A model refinement using the experimentally measured Fourier components can be used to obtain additional information about the overlayer structure. The structural model can be refined by minimizing

$$S = \sum_{\mathbf{h}} |G_{\mathbf{h},\mathrm{model}} - G_{\mathbf{h},\mathrm{exp}}|^2 \tag{2.35}$$

in a grid search. $G_{h,model}$ and $G_{\mathbf{h},exp}$ are the model-calculated and XSW-measured Fourier components, respectively. Only the atomic position z along the **c**-axis

was varied in a systematic way. As a result the structural model with the best agreement can be identified.

The contribution $I(n)$ of a plane of atoms at depth $d(n)$ in the film is attenuated by the overlying atomic planes

$$I(n) = \left(1 - e^{\frac{-d(n)}{\lambda_{\mathbf{h}} \cos\theta_{\mathbf{h}}}}\right) - I\,(n-1) \tag{2.36}$$

where $\lambda_{\mathbf{h}}$ is the inelastic mean free path calculated from the TPP-2M equation[45] and $\theta_{\mathbf{h}}$ is the emission angle and n is an integer number counting the layers starting from the surface. In this way, the attenuation of the signal from deeper layers by the overlying atomic layers can be taken into account.

3. Experimental

In this chapter, the characteristics of the insertion device beamline 32 (ID32) at the ESRF and the available experimental facilities are are described. The experimental station had two experimental hutches (EH) dedicated to the study of surfaces and interfaces. EH1 was equipped with a six-circle diffractometer, mainly used for SXRD, or XSW, measurements under fluorescence detection. A PHOIBOS 225 HV analyzer (SPECS, Berlin, Germany) was installed on a UHV chamber in EH2 for HAXPES and XSW experiments. The beamline had a dedicated surface characterization laboratory (SCL) available which provided sample preparation and in-situ characterization methods.

A detailed description of the experimental setup at ID32 was published by Zegenhagen *et al.*[52] From December 2011 the ID32 beamline was no longer accessible for external users and after a final period of in-house experiments the beamline was dismantled during the summer shutdown in 2012.[53]

3.1. ID32 beamline

Highly relativistic electrons, with a kinetic energy of 6 GeV, circulate in the ESRF storage ring. In order to keep them on a circular trajectory, bending magnets are installed in periodic distances. The interjacent straight sections contain an arrangement of multipole magnets for refocusing, radio frequency cavities to compensate for the energy loss of the beam, and insertion devices to extract horizontally polarized photon beams of high brilliance. The ID32 beamline was installed on a 5 m straight section and equipped with three undulators covering a photon energy range of 1.4–30 keV, providing a maximum photon flux of $\sim 10^{15}$ph s^{-1} mm^{-2} at 2.5 keV (0.1% bandwidth, 30 m source distance, 200 mA ring current).[52]

Several optical elements were in place to provide a monochromatic and, if needed, focused beam with a well-defined cross section. Along the beam path a system of slits, beam position and intensity sensors were used to tailor the dimen-

sions and monitor the photon flux in the beam. The main optical components will be explained briefly.

The first optical element was a liquid nitrogen cooled Si (1 1 1) double crystal monochromator (DCM) with an energy resolution $\Delta E/E = 1.3 \times 10^{-4}$. Further downstream a remotely controlled focusing system ('transfocator') had been installed recently which allowed different packages of compound reflective lenses to be introduced in the beam. It was possible to combine different packages to produce a highly focused photon beam ($20 \times 300\,\mu$m) at 121 discrete energies.

A flat mirror with stripes of SiO_2, Ni and Pd coatings was installed in the second optical hutch, which served as a low-pass filter, to reduce the intensity of higher harmonic radiation transmitted by the DCM. This mirror was used during diffraction experiments in EH1.

Two high-precision post-monochromators were available equipped with Si(111), (220), and (311) channel-cut crystals. The high energy resolution required for HAXPES and XSW experiments was achieved by utilizing higher index reflections.

3.1.1. Diffractometer — Experimental hutch 1

The first hutch housed a six-circle kappa diffractometer. A variety of experiments were possible using this diffractometer. Electrochemical reactions at the solid liquid (electrolyte) interface were investigated by performing SXRD measurements in the electrochemical environment provided by various electrochemical cells. Diffraction experiments could be easily combined with XSW measurements under fluorescence detection by mounting an energy dispersive solid-state detector (e.g. the VORTEX detector) close to the sample. An automatic filter system prevented saturation of the NaI scintillation detector. A UHV baby chamber was used to transport samples from the SCL to the beamline and it was mounted directly on the diffractometer for studies under UHV conditions.

For the SXRD measurements presented here the samples were mounted in an electrochemical cell under a mylar foil with flowing N_2. By using this cell it was possible to avoid sample modification due to O_3-formation induced by the high intensity of the photon beam.

The photon beam was set to an energy of 17.7 keV with an incident angle of 0.3°. The typical beam size was 0.06×0.5 mm which corresponds to the full width half maximum of the focused beam.

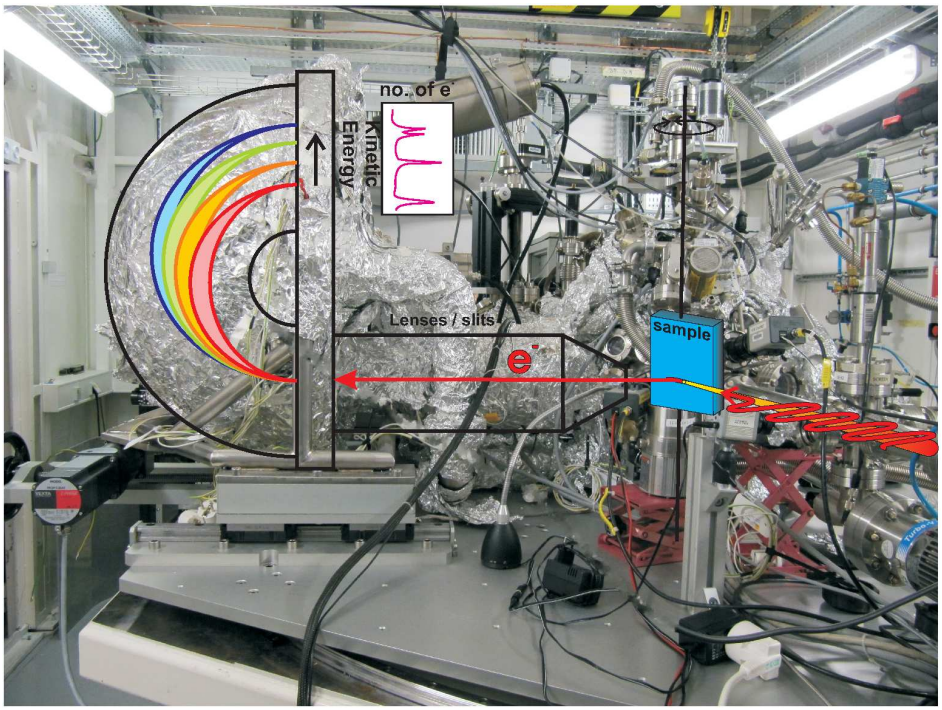

Figure 3.1.: Photograph of the PHOIBOS 225 HV analyzer as it was installed on ID32 together with a schematic of the incident polarized X-ray beam and the flight path of the electrons in the analyzer.

3.1.2. HAXPES endstation — Experimental hutch 2

HAXPES measurements were performed in EH2. For these experiments, a flight tube was installed in EH1 and pumped to high vacuum to avoid the reduction of intensity due to air scattering and to provide a windowless connection to the storage ring. The drain current from a thin metal foil at the entrance of EH2 was used to monitor the intensity of the incident beam. A PHOIBOS 225 HV analyzer (SPECS, Berlin, Germany) capable of analyzing electrons with kinetic energies $\leq 15\,\mathrm{keV}$ was mounted on a UHV analysis chamber (base pressure $\leq 10^{-9}\,\mathrm{mbar}$). A photograph of the experimental equipment in the hutch is shown in Figure 3.1 together with a simplified sketch of the incoming X-ray beam and the flight path of the emitted electrons in the hemispherical mirror analyzer. The analyzer was oriented in the polarization direction of the photon beam to avoid multipole effects in the photoemission spectra, which can strongly influence the coherent fractions obtained in XSW measurements. The electrons were detected by a delay line detector which provided a high count rate capability and a low background noise level. A reflective screen was installed in backscattering geometry to monitor the intensity of the reflected beam by measuring the drain current. The sample

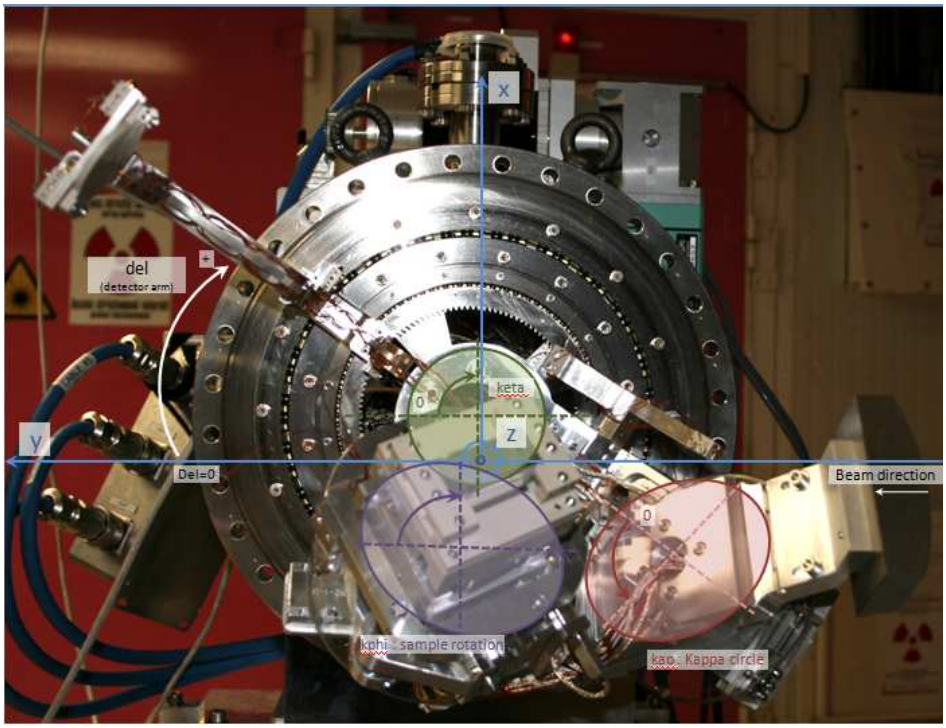

Figure 3.2.: Photograph of the high-precision kappa manipulator before installation in the HAXPES chamber. Several encoded piezo stepper motors are used to ensure reproducible sample positioning. The various different rotations provided by the manipulator are indicated. Courtesy of Julien Duvernay.

manipulator provided 3 translational movements (vertical, and horizontal both along and perpendicular to the beam) and polar and azimuthal rotations. It was connected to a liquid He cryostat via a copper braid for controlled cooling to temperatures down to about 40 K.

For the quantitative analysis of the XPS spectra, a Shirley background function was used for background correction and a multi-peak deconvolution procedure using combined Gaussian and Lorentzian function was used to extract the exact peak positions and intensities. The overall instrumental resolution was determined by fitting the Fermi edge of a Au reference sample. Energy calibration was performed by measuring the Au $4f_{7/2}$ core level peak during each experimental run.

The new in-house developed kappa manipulator was installed and tested in the HAXPES main chamber during this period of time. A photograph of the manipulator is shown in Figure 3.2. This custom-built manipulator was designed

to provide the precision required for XSW measurements on tilted reflections and on high-quality samples like silicon.

The preparation chamber provided facilities for low-energy electron diffraction (LEED) measurements, sample heating, and thin film deposition with thickness monitoring using a variety of evaporators.

3.2. Surface characterization laboratory

A wide range of UHV-based surface preparation and characterization tools were available in the SCL in two separate UHV systems.

The larger UHV system consisted of a central R2P2 transfer chamber with eight side chambers, each offering different surface preparation and characterization techniques. Sample transfer was achieved using the central transfer arm. Two side chambers were dedicated to sample annealing. One was equipped with a resistive heater that could operate at temperatures up to 900°C and a sputter gun for Ar-ion bombardment. The second chamber had an electron-beam bombardment heater which enabled temperatures above 1300°C to be reached routinely. A combined LEED and Auger electron spectroscopy system was used to check surface cleanliness and order. An Omicron micro-STM system was installed for surface characterization. To minimize vibrations during STM measurements all of the mechanical pumps were turned off and the system was lifted on air-pressurized damping pillars. Two other sample preparation facilities were available. One chamber was used for pulsed laser deposition. A picture of the interior of the PLD deposition chamber is shown in Figure 2.4 in Section 2.2. The Compex 205 KrF Excimer UV laser (Lambda Physics, Santiago, Chile) was operated at a wavelength λ=248 nm with pulse length of 25 ns and an energy of 240 mJ per pulse for thin film deposition. The beam was reflected into the UHV deposition chamber through a quartz window and focused by a lens down to about 5×2 mm on the target surface providing a power density of 80 MW/cm^2. A 0.5 mm thick platinum wire was chosen for the resistive heater to permit annealing at high oxygen partial pressures.

A smaller chamber was available with an Omicron STM with a tripod scanner, a LEED system and different evaporation cells for thin film deposition, but this chamber was not used for the experiments described in this thesis.

4. Conductive interfaces between $SrTiO_3$ and polar oxides

The conductive heterointerfaces formed between polar perovskite films of $LaAlO_3$, $LaGaO_3$ and $NdGaO_3$ and (0 0 1) surfaces of $SrTiO_3$ are the focus of this chapter. The basic properties and the scientific questions concerning these systems are presented in the introduction (Section 4.1). In the following Section 4.2 the deposition of films in the SCL at the ESRF and in Naples, Italy will be outlined. The characterization by SXRD, HAXPES and XSW of films grown in Naples is the subject of Section 4.3. XSW imaging results of 2 ML and 5 ML thick $LaAlO_3$ films presented in Section 4.4 reveal distortions in the overlayer. The last Section 4.5 focuses on the valence band region. The gap states were studied with site-specific valence band spectroscopy in comparison with oxygen-deficient $SrTiO_{3-\delta}$ and 2 % Nb-doped $SrTiO_3$ single crystals.

4.1. Introduction

Ohtomo and Hwang[4] were the first to observe that a highly mobile 2-dimensional electron gas (2DEG) can form at the $LaAlO_3/SrTiO_3$ interface, despite the fact that the constituent materials are both band insulators. This 2DEG sparked significant scientific interest which, in the following years, revealed some typical characteristics for this system. (i) The formation of a 2DEG is only observed on TiO_2-terminated $SrTiO_3$ substrates and (ii) only for $LaAlO_3$ overlayer thicknesses above 4 ML.[54] The conductivity drops slowly for higher coverages.[55] (iii) Depending on the preparation conditions, the observed carrier densities differ significantly and are in most cases much smaller than the 1/2 e^- per surface unit cell ($= 3 \times 10^{14}\,\mathrm{cm}^{-2}$) theoretically predicted for a purely electronic reconstruction.[56] (iv) Interfaces appear to be atomically sharp in STEM studies and show no apparent signs of intermixing.[57]

In the following, we will consider more closely the interface formed between these two structures. For this it is convenient to visualize the structures as stacks of alternating AO and BO_2 planes along [001]. Owing to the differences in the

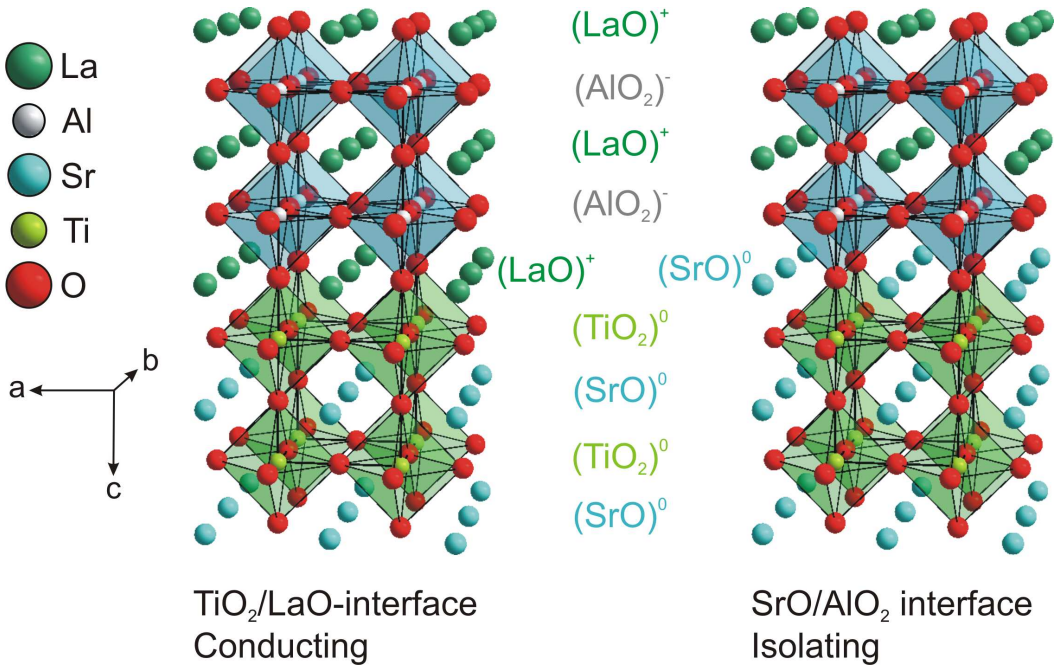

Figure 4.1.: Structural models of ideal $LaAlO_3/SrTiO_3$ interfaces with two different interface configurations. Depending on the termination of the $SrTiO_3$ surface one observes a TiO_2/LaO or a SrO/AlO_2 interface. The perovskite stacking sequence is preserved in both cases.

valences of the constituting atoms, the LaO planes will formally carry a charge while the $SrTiO_3$ planes stay formally neutral. Figure 4.1 shows that at the ideal interface the perovskite stacking sequence is preserved. Two different interfaces result depending on the termination of the $SrTiO_3$. On TiO_2 terminated substrates growth will start with a LaO layer and on a SrO terminated substrate the first layer will be AlO_2. The formal valence states can be assigned as La^{+3}, Al^{+3}, O^{-2}, Sr^{+2} and Ti^{+4}. Only Ti has accessible mixed-valence character, allowing for reduction towards Ti^{+3}.

The 'A' and 'B' atoms donate charge to the 3 oxygen anions per unit cell. In the case of $SrTiO_3$, a formal charge transfer of one electron from Sr and two electrons from Ti results in charge neutral SrO and TiO_2 planes. For $LaAlO_3$, the valence of Al and La are both 3+, and the alternating layers will carry a formal charge $(LaO)^+$ and $(AlO_2)^-$. In the bulk crystal, the overall charge is kept neutral, but at the interface of an ideal $LaAlO_3$ crystal, a polar discontinuity arises. Thus, the repeated addition of $LaAlO_3$ layers on top of $SrTiO_3$ leads to a increasing dipole and a divergence of the interface energy as shown schematically in Figure 4.2(b). This behavior was coined the "polar catastrophe" and can be seen as the interface variant of the divergent surface energy for unreconstructed polar surfaces described by Tasker.[58] Polar surfaces are known to reconstruct,

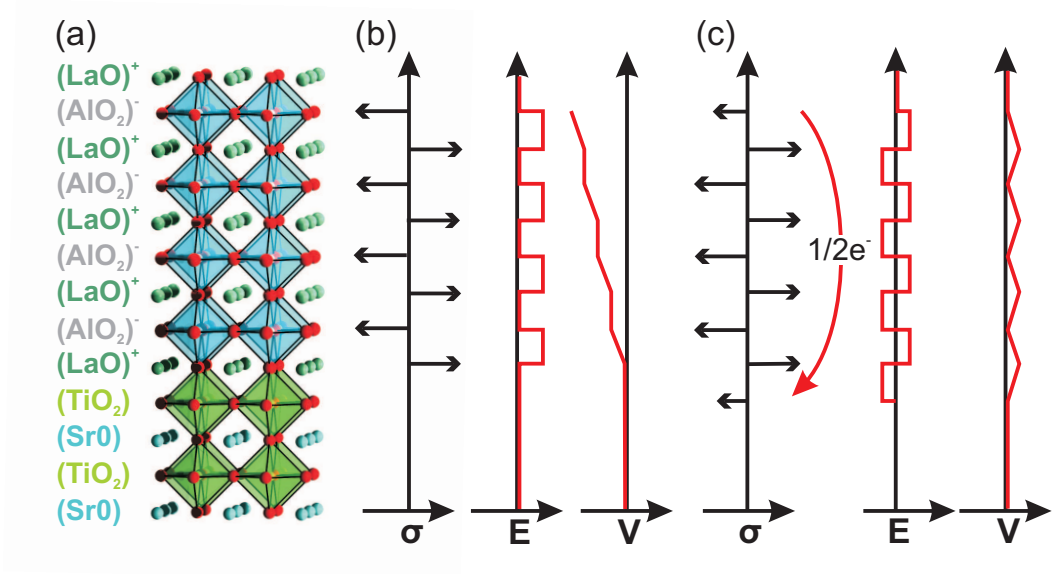

Figure 4.2.: The polar discontinuity at (a) a TiO_2/LaO interfaces is caused by the polar nature of the $LaAlO_3$ overlayer. (b) It can be seen that for the unreconstructed interface the alternating charges σ give rise to a change in the electric field $\mathbf{E}$. This results in a diverging electrostatic potential V. (c) A possible reconstruction involves the transfer of 1/2 electron per interface unit cell, resulting in a suppression of the potential build-up.

form facets or large surface unit cells due to vacancy ordering.[59] For the interface, substantial reconstructions and roughening could be expected. However, as an alternative to atomic reconstructions, electronic reconstructions can provide a solution to this problem.

It was suggested that when the potential build-up across the $LaAlO_3$ overlayer reaches the value of the effective band gap, electrons are transferred from O $2p$ orbitals at the top of the valence band at the $LaAlO_3$ surface to the Ti $3d$ conduction band. This should lead to the accumulation of $1/2e^-$ per unit cell at the interface for compensation[4] and should yield convergent potentials (see Figure 4.2(c)). The extra half electron creates a n-type $(LaO)^+/(TiO_2)^0$ and a p-type $(AlO_2)^-/(SrO)^0$ interface. However, there is no conductivity observed for the p-type interface as there are no atoms with available mixed valence states. This interface can, however, be compensated by the introduction of vacancies[60] and interface reconstruction/roughening.[61]

As intriguing as this model may be, there is scientific evidence against it. For example for a thickness below the critical limit for conductivity the potential would be expected to be uncompensated. This should give rise to a potential

build-up of 0.6 to 0.9 V/ML.,[62,63] however, such a potential has not yet been observed.[64–66] Thus, several slightly more complex mechanisms have been proposed such as interdiffusion or intermixing at the interface,[67] formation of a conductive intermediate phase, strain-induced lattice distortions,[68,69] intrinsic doping with electrons[70] and the formation of oxygen vacancies.[61,71]

Although the term "2-dimensional electron gas" is used frequently, the conductive interface actually has a finite thickness. Basletic *et al.*[72] studied cross sections of differently prepared interfaces with conducting-tip atomic force microscopy (CT-AFM). The experiments prove that the conductivity is clearly related to the $SrTiO_3$ side of the interface and the thickness of the conductive layer was found to be less then 7 nm. The true dimensions are surely smaller due to convolution with the tip. Estimates via the sheet carrier density yield a thickness of 1 nm ($\sim$ 2–3 $SrTiO_3$ unit cells). This observation is confirmed by IR-ellipsometry measurements by Dubroka *et al.*[73] They found the 2DEG to be concentrated in the $SrTiO_3$ substrate with a full width at half maximum of 2 nm. Angle-dependent HAXPES measurements of the Ti 2*p* core level were performed by Sing *et al.*[74] The Ti 2*p* core levels of conductive titanates exhibit a shoulder on the low binding energy side. Under the assumption that every Ti^{3+} dopes the $SrTiO_3$ with one electron, the Ti^{3+}/Ti^{4+} ratio is a measure of the carrier density. Depending on the sample preparation conditions they obtained thicknesses between 0.4 nm and 30 nm and sheet carrier densities between $3\times10^{13}\,\mathrm{cm}^{-2}$ and $2\times10^{14}\,\mathrm{cm}^{-2}$.

Until now, the formation of such a 2DEG could be shown for polar oxide overlayers other than $LaAlO_3$ such as $LaGaO_3$[29,75] and $NdGaO_3$ (cf. Table 4.1), but only using $SrTiO_3$ as the substrate. Hence the effect seems to be intrinsically related to $SrTiO_3$. The critical overlayer thickness for conductivity was found to be identical for those films. This is not straightforward since the dielectric constants and hence the expected potential build up are most likely not identical. However, recent results by Reinle-Schmitt *et al.*[76] show that the critical thickness increases linearly with the decreases of the charge density in the layers of the polar material. In their case the variation of the charge density was achieved by depositing films of a series of solid solutions of the polar and a non-polar materials $LaAlO_3$ and $SrTiO_3$.

The potential build-up is strongly influenced by subtle structural changes in the overlayer. It was shown by DFT calculations that polar distortions can help to reduce the potential build-up with increasing film thickness[68,77,78] since they reduce the effective charge of the individual layers. Lattice distortions are therefore of crucial importance to explain the 2DEG in terms of the polar catastrophe model. Experimental evidence was found by diffraction as well as microscopic techniques. Vonk *et al.*[79] performed a SXRD study at elevated temperatures. Their results show that the films grow undistorted at deposition temperature. Upon cooling the cation distances at the interfaces increase to more then 4 Å while the oxygen atoms

move towards the interface. At the same time, in the $SrTiO_3$ substrate, the $TiO_{6/2}$ octahedra contract along their principal axis and the Ti is displaced off-center. SXRD studies by Pauli *et al.*[69] indicate that the polar distortions decrease for thicker $LaAlO_3$ overlayers. On the other hand, an analysis by direct methods in the same group[67] was interpreted as a sign for intermixing. High-resolution TEM was employed to obtain real-space images showing an expansion of the $LaAlO_3$ unit cell at the interface[80] and a buckling of metal oxide planes.[57] The Jahn-Teller like distortion of the $TiO_{6/2}$ octahedra was confirmed by linear dichroism in X-ray absorption spectroscopy[81] to result in the expected energy splitting of the Ti $3d$ out-off-plane and in-plane orbitals. Nevertheless, distortions alone do not provide a straightforward explanation for the conductive layer.

X-ray diffraction measurements are complicated by the low electron density of oxygen (8 electrons) and Al (13 electrons) in comparison to the heavier Ti (22 electrons) and La atoms (57 electrons) which makes diffraction intrinsically insensitive to the positions of oxygen and aluminum. This is exemplified by a series of simulated (11ℓ) CTRs for a 5 ML thick $LaAlO_3$ film on $SrTiO_3(001)$ in Figure 4.3. In the consecutive simulation steps, the oxygen content was lowered systematically, ultimately resulting in oxygen-free LaAl. Cation positions were kept in their ideal perovskite-like positions. The small variations between the different simulations are very hard to detect and demonstrate the low sensitivity to oxygen.

One aim of the study presented here is to elucidate the distortions expected for these interfaces by use of the XSW imaging technique (see Section 4.4). Fourier coefficients of the atomic density distribution are measured for all elements of the film and model-free real space images are obtained by inverse Fourier transformation. A comparison of an insulating 2 ML thick and a conductive 5 ML thick $LaAlO_3$ film will be discussed in Section 4.4.

Another important aspect are oxygen vacancies in the $SrTiO_3$ substrate,[82,83] which are known to be created in bulk $SrTiO_3$ by annealing in a reducing atmosphere. In the case of the $LaAlO_3/SrTiO_3$ interface, these vacancies may be produced in various ways such as (i) annealing at low oxygen pressures during deposition, (ii) bombardment by energetic particles created in the PLD process, (iii) oxygen uptake by the $LaAlO_3$ film and (iv) other processes like field-effect induced vacancies[84] in the potential of the $LaAlO_3$ overlayer. The first contribution can be reduced by deposition at high oxygen pressures while the second contribution can not be avoided effectively. A detailed study of the PLD process with an ultra-fast camera revealed that the plasma has sufficient energy to break Ti-O bonds.[29] Theoretical density functional calculations indicate that the formation of oxygen vacancies may be favored by the polarity of the $LaAlO_3$ overlayers.[60]

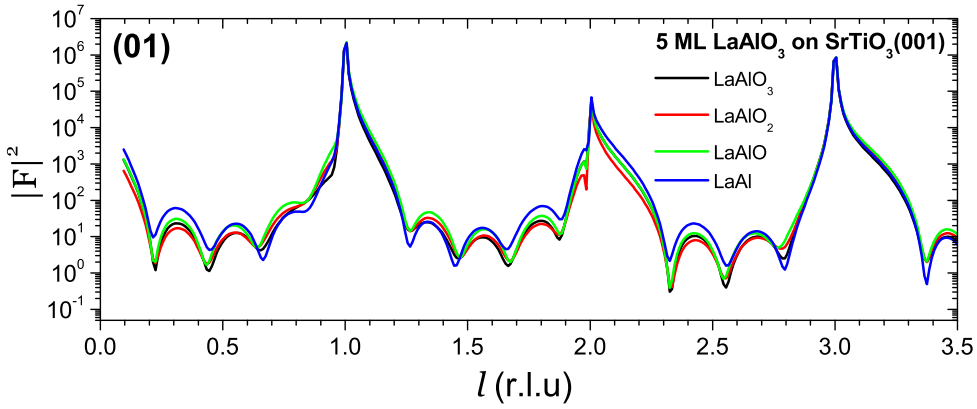

Figure 4.3.: Simulations of the (01ℓ) CTR of $SrTiO_3$ with a 5 ML $LaAlO_3$ overlayer (black). In the consecutive CTR simulations one oxygen was removed per unit cell without changing the cation positions leading to $LaAlO_2$ (red), LaAlO (green) and LaAl (blue).

A conductive interface is formed for amorphous $LaAlO_3$ overlayers. Due to the lack of crystalline order in an amorphous layer there will be no potential build-up. This observation of conductivity was understood as the result of oxygen uptake in the slightly oxygen-deficient $LaAlO_3$ film after the deposition process. Similar processes cannot easily be excluded for the crystalline interface.[85] Many groups try to minimize the contributions by oxygen vacancies in a post annealing step at high oxygen pressure ($\sim 1\,\mathrm{mbar}$). Bare $SrTiO_3$ substrates do not show vacancies after being exposed to $LaAlO_3$ deposition conditions. To summarize, contributions by oxygen vacancies cannot be excluded with certainty. Nevertheless, a mechanism based solely on vacancy formation is not able to give a straight forward explanation of characteristic features of the 2DEG such as the critical thickness. The question whether vacancies arise as a response to the potential or if they are one of the causes for the 2DEG formation remains unsolved.

Table 4.1.: Overview of the growth conditions used by various groups as reported in the literature. Besides $LaAlO_3$, films of $LaGaO_3$, $LaTiO_3$, $LaVO_3$, $NdGaO_3$ and $KTiO_3$ have been grown recently.

material	**fluence** (Jcm^{-2})	**rep. rate** (Hz)	**pressure** (mbar)	**temperature** (°C)	**citation**
$LaAlO_3$	1	2	1.33×10^{-3} –1.33 $\times10^{-5}$	800	Ohtomo[4]
	...	...	wide range	850	Brinkman[86]
	1.6	...	1×10^{-4} – 1.33 $\times10^{-5}$	815	Siemons[87]
	1	10	5×10^{-2}	770	Willmott[67]
	...	...	4×10^{-4}	850	Vonk[79]
	0.6	1	1.66×10^{-4}	800	Reyren[88]
	...	...	5×10^{-5}	770	Reyren[70]
	...	...	1.33×10^{-3} and 1.33×10^{-5}	800	Kalabukhov[71]
	3	5	1.33×10^{-6}	750	Nakagawa[61]
	3	...	1×10^{-4}	800	Savoia[89]
$LaGaO_3$	1.5–2.5	2	1×10^{-2} –1 $\times10^{-4}$	800	Perna[75]
$LaTiO_3$	3	4	1.33×10^{-5}	750	Ohtomo[90]
$LaVO_3$	2.5	4	1.33×10^{-8} –1.33 $\times10^{-2}$	500–900	Hotta[91]
	2.5	4	1.33×10^{-6}	600	Hotta[92]
$NdGaO_3$	1.5–2.5	2	1×10^{-2} –1 $\times10^{-4}$	800	Di Uccio[93]
$KTiO_3$	1.5	1/10	1×10^{-4}	750	Kalabukhov[94]

The fact that the 2DEG (i) is only found in the $SrTiO_3$ and does not extend into the overlayer and (ii) the interface can also be formed with other overlayer materials demands for a more detailed study of $SrTiO_3$ alone. In this light, it is important to realize that $SrTiO_3$ can be made n-type conducting by doping, e.g. with La, Nb, or oxygen vacancies.

Unlike a typical band semiconductor, which undergoes a rigid band shift upon doping, electron-doped $SrTiO_3$ has extended states in the band gap.[95–99] The behavior upon doping may be best explained by the Haldane-Anderson impurity model.[100,101] However, until now, first-principle calculations that comprehensively describe the electron doping behavior of $SrTiO_3$ are still lacking. Oxygen-deficient $SrTiO_3$ was investigated within the Hubbard model by Sarma *et al.*[97] In a later publication,[102] Shanthi and Sarma used a LMTO-ASA approach arguing that correlation effects should not be relevant because of the low electron concentration. Their study suggests that at low oxygen vacancy concentration the Fermi level moves up into the conduction band in a fashion resembling a rigid band shift, whereas localized states with substantial Ti 3*d* character appear in the band gap at higher concentrations as a result of oxygen vacancy clustering. This clustering is expected to result in distortions in the Ti 3*d* bands noticeable as a small hump close to the Fermi level.

A resonant XPS study of PLD grown 5% Nb:$SrTiO_3$[103] showed that the Fermi level has mainly Ti 3*d* character the O 2*p* derived density of states was found to be more dominant at higher energies $E_B \geq 1.5\,\mathrm{eV}$. Additionally, they report the presence of a weak Ti-derived in-gap state that resembles qualitatively the feature described for oxygen-deficient $SrTiO_3$.

Recent soft X-ray ARPES measurements[104,105] on weakly doped (weak annealing, Nb-doping) $SrTiO_3$ crystals showed the formation of surface bands. These surface bands were proposed to play a role at the $LaAlO_3/SrTiO_3$ interfaces. In the case of the Nb-doping a pronounced sensitivity to the incoming photon beam indicated photoinduced carriers. A similar behavior was observed by electrical measurements under X-ray light by Sing *et al.*[74] for the $LaAlO_3/SrTiO_3$ interfaces.

Further information about the conductive interface can be obtained by a combination of HAXPES with XSW. The combination of these techniques provides a large information depth and additionally allows the position in the unit cell of $SrTiO_3$ from where the photoelectrons originate to be identified. This site-specific PES analysis was recently used to analyze the VB of $SrTiO_3$[9] and to unravel correlation effects in the valence band of V_2O_3.[8]

It is instructive to compare the electron "doped" n-type interface with doped n-type bulk $SrTiO_3$ obtained by the substitution of Ti with Nb and by creating oxygen vacancies. The doping mechanisms for Nb:$SrTiO_3$ and $SrTiO_{3-\delta}$ are

significantly different. In the case of Nb:$SrTiO_3$ a Ti^{4+} ion is replaced by Nb^{5+} leading to a doping by 1 e^- per Nb-atom. The doped electron is hence associated with the Nb located at the Ti site and the next Ti atom is a second nearest neighbor. Each oxygen vacancy formally dopes 2 e^- and is a direct neighbor to 2 Ti atoms. From this simple picture we would expect differences in the electronic structure and hence the photoemission spectra for these two systems. Nb:$SrTiO_3$ would be expected to be closer to the scenario for intrinsic electron doping. The XSW method may be able to catch a fingerprint for the different origins of conductivity and thereby shed more light on the origin of conductivity at the $LaAlO_3/SrTiO_3$ interface. Section 4.5 presents a study where we determine, without any assumptions, which part of the photoelectron yield, observed in the band gap of $SrTiO_3$, originates from the Ti sites. We investigate an $SrTiO_3$ sample with five MLs of $LaAlO_3$ in comparison with oxygen-deficient $SrTiO_3$ ($SrTiO_{3-\delta}$) and Nb doped $SrTiO_3$ (Nb:$SrTiO_3$) samples and, therefore, can deduce a mixed origin from field-induced oxygen vacancies and intrinsic doping.

To conclude, a thorough XSW and XPS/HAXPES analysis may help elucidate details of the atomic and electronic structure at the interface. Samples of high structural perfection are needed for these experiments. The first part of this chapter presents the deposition process for these films and their characterization by SXRD as well as atomic force microscopy. The second section (see Section 4.4) presents an XSW imaging investigation of the distortions in an insulating 2 ML and a conductive 5 ML thick heterostructure. The last part of this chapter (see Section 4.5) focuses on a comparative valence band study of Nb-doped $SrTiO_3$ (Nb:$SrTiO_3$), oxygen-deficient $SrTiO_3$ ($SrTiO_{3-\delta}$) and a conductive $LaAlO_3/SrTiO_3$ interface. The experimental approach combines HAXPES with the XSW technique to characterize and better understand the differences between these samples and use this knowledge to draw conclusions about the $LaAlO_3/SrTiO_3$ 2DEG.

4.2. Sample preparation

Sample preparation and the preliminary characterization of the perovskite films on $SrTiO_3$ are described in this section. $LaAlO_3$ thin films were prepared by PLD in the SCL of the ID32 beam line and characterized by AFM and XRD. Despite the high quality of the epitaxial films grown at the ESRF no interface conductivity could be achieved on a routine basis. The reason for this remains unclear.

Films with state of the art electrical properties were provided by our collaborators from CNR-SPIN (Naples, Italy) and shipped to the ESRF. The film deposition procedure used in their lab will be outlined briefly. $NdGaO_3$ and $LaGaO_3$ thin

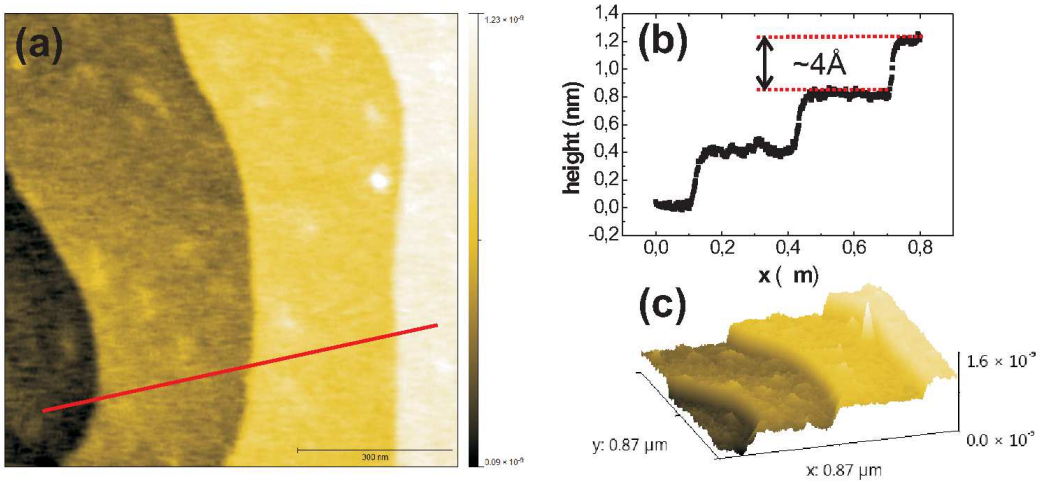

Figure 4.4.: (a) AFM micrograph of a BHF etched $SrTiO_3$ surface after recrystallisation. The line marks the position of (b) a line profile with sharp steps of unit cell height. Figure (c) shows a 3D perspective view of the surface.

films were grown on $SrTiO_3$ in addition. All of the films were characterized by SXRD and HAXPES (see Section 4.3) to ensure sufficient quality for XSW imaging experiments (see Section 4.4) and valence band studies (see Section 4.5).

4.2.1. $SrTiO_3$ surface preparation

Samples were grown on the Ti terminated (001) surface of edge oriented $SrTiO_3$ single crystal substrates. A procedure to obtain perfect single terminated $SrTiO_3$ surfaces was described by Kawasaki *et al.*[106] The process makes use of the different solubility of the TiO_2 and SrO planes in buffered hydrofluoric acid (BHF). Surfaces prepared this way exhibit deep etch pits but are single terminated. Koster *et al.*[107] reported a significant reduction of surface roughness by hydroxylation of the SrO sites by soaking in analytic grade demineralized water ultrasonically for 10 min prior to etching in BHF for 30 s. Remnants of the previous treatments are removed in a final rinsing step and subsequent annealing at 950 °C for 1 h in 1 bar molecular oxygen flow facilitates recrystallization.

Ohnishi[108] reported some refinements to this method. Annealing the substrate at temperatures above 300 °C leads to the reemergence of SrO on the surface and above 400 °C the Sr surface coverage saturates.[108] A re-etching of the substrate for 20 s in BHF or 10 min in water was shown to dissolve the SrO

thereby producing substrates that will be single terminated up to the $LaAlO_3$ deposition temperature of $\sim 800\,°C$.

Kareev[109] reported the creation of oxygen defects in the substrate from BHF etching compared to etching with a HCL-HNO_3 mixture. Substrates prepared in this route were soaked in deionized water at 70 °C for 20 to 25 min followed by etching for 30 s in HCL-HNO_3 (HCl:HNO_3 = 3:1) both in the ultrasonic bath. The etching step was followed by 30 min of annealing at 1000 °C under atmospheric conditions.

According to Erdmann,[110,111] at least 7 different surface reconstructions can be distinguished by LEED. These reconstructions occur as a function of the annealing temperature and serve as an indicator for the coverage by SrO or TiO_2. Hence, in theory, a controlled annealing step should be able to create a TiO_2 terminated surface without any chemical treatment. However, this route has not been considered in the published literature.

For the samples presented in the following, we followed the route described by Koster *et al.*[107] $SrTiO_3$(001) single crystal substrates were soaked ultrasonically in demineralized water for 10 min and etched in BHF for 30 s. The demineralized water was produced by a Millipore Elix system (R=10 – 15 MΩ/cm and pH 6 – 7), and the BHF solution was from Merck (NaH_4F:HF = 87.5:12.5 with pH 5.5). For the recrystallization, the samples were placed in a quartz glass tube under controlled O_2 flow and heated to 950 °C for a minimum of 1 h in a muffle furnace.

An AFM micrograph of a $SrTiO_3$ surface prepared in this way is presented in Figure 4.4. The image shows a surface with four terraces. The step edges are clearly defined and have a height of ~ 3.9 Å. This confirms that single terminated surfaces can be prepared by the preparation conditions described above.

4.2.2. Preparation of oxygen-deficient and Nb-doped $SrTiO_3$

For the valence band deconvolution presented in Section 4.5 a 2 % Nb-doped $SrTiO_3$ (Nb:$SrTiO_3$) and $SrTiO_{3-\delta}$ samples were measured for comparison to a 5 ML $LaAlO_3$ film.

The Nb:$SrTiO_3$ crystals (CrysTec, Berlin, Germany) were cleaned with ethanol and then annealed for 1 h in 1 bar oxygen flow at 850 °C to quench any oxygen vacancies. An undoped $SrTiO_3$ single crystal was rendered oxygen deficient by annealing for 2.5 h at 1050 °C in UHV ($< 5 \times 10^{-9}$ mbar). The $SrTiO_{3-\delta}$ showed a clear $(\sqrt{13} \times \sqrt{13})$R33.7° LEED pattern as shown in Figure 4.5. This pattern is

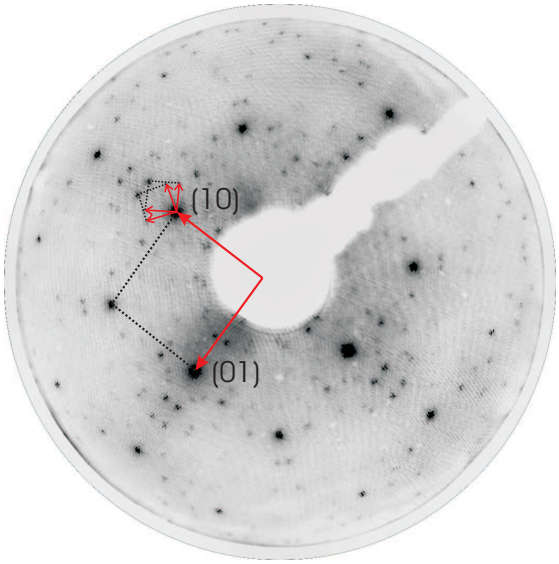

Figure 4.5.: Negative photograph of the LEED screen of a high-temperature annealed oxygen-deficient $SrTiO_3$ (001) surface. The image was obtained at room temperature with an electron energy of 129 eV. The $SrTiO_3$ unit cell is indicated by its lattice vectors. The lattice vectors of the $(\sqrt{13} \times \sqrt{13})$R33.7° superstructure are indicated around the (10) reflection.

typical for oxygen reduced samples annealed to temperatures above 1050 °C with a nearly perfectly TiO_2 terminated surface .[112]

These samples were transferred in air to the ultra-high vacuum (UHV) HAXPES endstation at ID32 within minutes and loaded into the UHV chamber. Photoelectron spectra confirmed that the samples were free of contaminants.

4.2.3. Films grown at the ESRF

$LaAlO_3$ thin films were deposited in the PLD chamber in the surface characterization laboratory of ID32. Substrates were annealed at deposition temperature and exposed to the oxygen atmosphere for several minutes prior to deposition. Deposition temperatures (T_{Dep}) of 750 °C to 820 °C and an oxygen atmosphere of 5×10^{-5} mbar were chosen in accordance with the literature (see Table 4.1). One laser pulse was found to be equivalent to $\sim$ 0.7 Å $LaAlO_3$ by calibration with reflectivity measurements. The target substrate distance was set to 5 cm. Some films were subjected to a tempering step at deposition temperature for up to 15 min. After deposition, the films were cooled in the deposition atmosphere to

room temperature. $LaAlO_3$ single crystals and sintered polycrystalline $LaAlO_3$ pellets (Kurt J. Lesker Company, Pittsburgh, USA) were used as targets.

The effect of cooling time and an annealing step at deposition temperature were studied systematically in SXRD and AFM experiments. Three samples with a nominal thickness of 8 ML are presented in the following. The first sample is representative for $LaAlO_3$ cooled freely from $T_{Dep}=820\,^\circ$ to room temperature (RT). This results in exponential cooling curves with very high cooling rates (15 °C/min) when the heater in turned off. The second sample was cooled in a controlled manner at an intermediate rate (10 °C/min) while a third sample, representative for samples held at T_{Dep} for ∼10 min to facilitate crystallization, was subjected to a slower cooling rate(5 °C/min).

An AFM image for the sample that was allowed to cool freely from T_{Dep} is presented in Figure 4.6(a). The 7 μm×7 μm image shows a stepped sample topography with an irregular step width. The step edges appear rough. A line profile along the red line is shown in Figure 4.6(b) and reveals steps with a 1–2 ML height. Additionally, areas of erratic topography (marked with arrows) accumulate close to step edges. Reciprocal space maps (Fig. 4.6(c)) in the hk-plane at $\ell = 0.15$ were measured for this sample. Powder rings at distances 1, $\sqrt{2}$, $\sqrt{3}$ and 2 are clearly visible. They correspond to the (001), (110), (111) and (002) lattice planes.

For these fast cooling rates the films are not completely ordered. AFM images reveal rough step edges and areas with an uneven morphology. The in-plane reciprocal space maps reveal the formation of powder rings and hence confirm that parts of the film are poorly oriented. The relatively high intensity of the out-of-plane (111) powder ring shows that the disorder is not constrained to misalignment in the **ab**-plane.

Figure 4.7(a) shows a 2.3 μm×2.3 μm AFM image of the sample, held at elevated temperatures for a longer period and subjected to a slow cooling. The AFM micrograph shows a structured topography with two predominant directions. Many step edges form 90 ° angles. The scan direction is at 45 ° to the crystallographic axes. Since the surface steps predominantly span angles of 45 ° with the scan direction it is clear that most edges follow the cubic [001] and [010] directions. The average direction of the terraces deviates from the crystallographic orientation and appears to be defined by the miscut direction of the substrate or a gradient in the film thickness. Terraces are several hundred nm wide. A line scan (Fig. 4.7(b)) reveals step heights of up to 3 nm (∼ 8 ML).

The pronounced step bunching of up to 8 ML indicates significant surface diffusion at the growth temperature since the bare substrate exhibits mostly 0.4 nm steps. The faces of the cubic form {001} appear to be energetically most favorable.

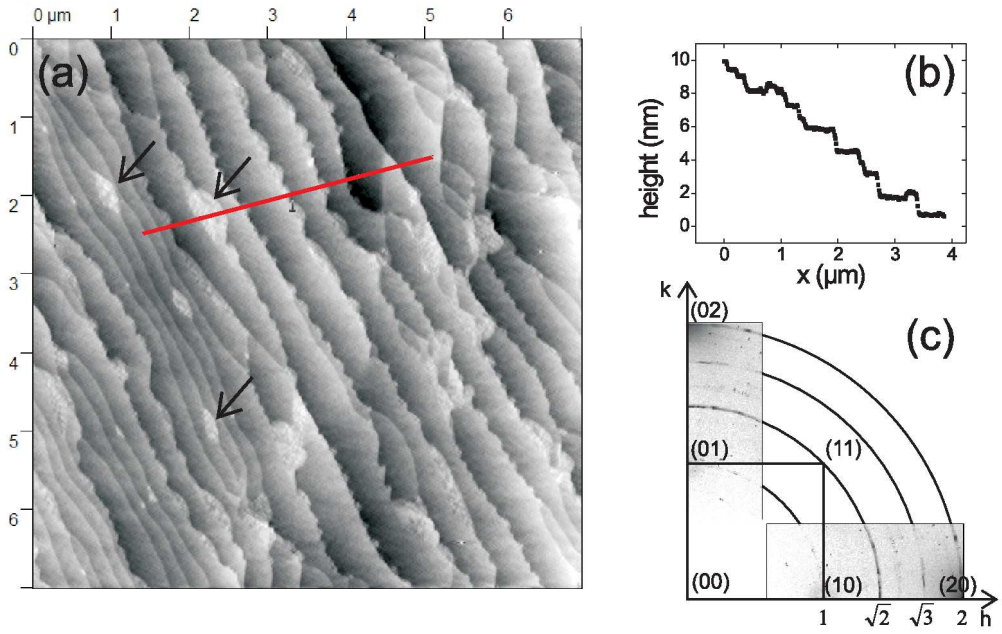

Figure 4.6.: Characterization of a 8 ML $LaAlO_3$ film allowed to cool freely from T_{Dep} to room temperature. (a) AFM image showing irregular steps and areas with disordered material (arrows). The red line marks the position of (b) a line profile with sharp steps. (c) 2d-scan in the hk-plane reveals powder rings.

It could not be distinguished whether the bunching is driven by surface energy minimization or to compensate for strain induced by the lattice mismatch.

In comparison, the sample cooled to room temperature at an intermediate rate (10 °C/min) shows a very homogeneous surface topography in a $1\,\mu m \times 1\,\mu m$ AFM micrograph (Fig 4.7(c)). The terrace width is reduced to a few tens of nm. Step edges are very smooth and their orientation appears to be dominated by the miscut direction. In the line profile shown in Figure 4.7(d) the average step height of ~ 0.4 nm corresponds closely to the unit cell size of $LaAlO_3$. Note, that there is a dislocation visible in the center of the AFM micrograph.

The unit cell (or integer multiple) step heights in all three samples points to a single terminated $LaAlO_3$ surface. From arguments of charge balance, assuming perfect TiO_2 termination of the $SrTiO_3$ substrates, we can conclude that the $LaAlO_3$ films are AlO_2 terminated. From the homogeneous terrace width and the unit cell step height we can conclude that the best growth conditions are achieved for intermediate cooling rates.

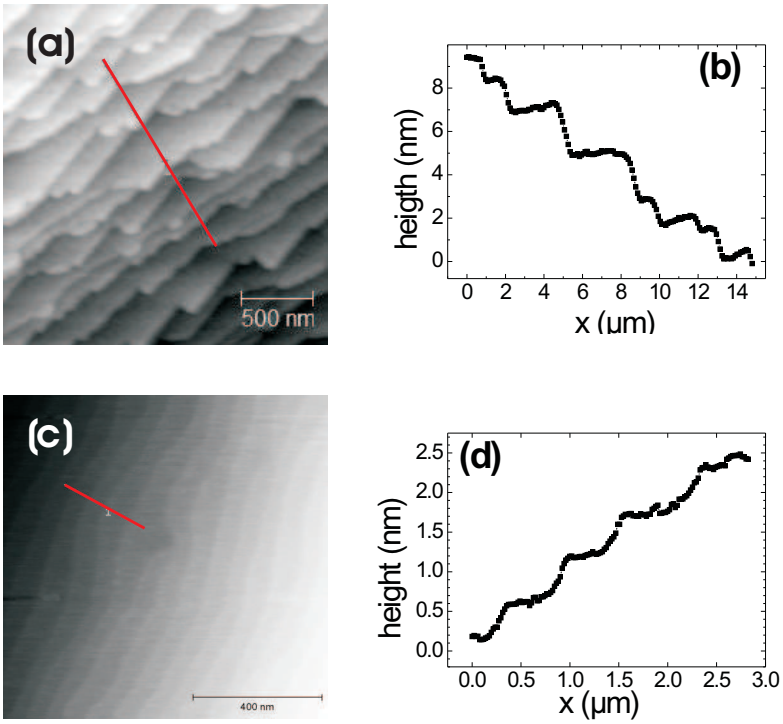

Figure 4.7.: AFM images and profiles of ∼8 ML thick $LaAlO_3$ films deposited at 820 °C. The cubic axes are 45 ° to the scanning direction. (a) tempered for 10 min, cooling time 2 h with corresponding profile (b) showing several nm steps. (c) 1 h cooling time and no tempering. The line profile (d) reveals ∼ 0.4 nm unit cell steps.

4.2.4. Films grown in CNR-SPIN

Films were prepared by PLD on TiO_2-terminated $SrTiO_3(001)$ substrates held at a temperature of 800° in 3×10^{-3} mbar molecular oxygen and a cooling rate of (2 to 3) °C/min. It was found that samples grown at higher pressures (10^{-1} mbar) did not show significant differences, whereas at 0.1 mbar the interfaces were not conducting. Furthermore, the substrate surface quality influenced the electrical properties. In addition to the $LaAlO_3$ films, thin films for $LaGaO_3$ and $NdGaO_3$ were prepared as well. Electrical characterization of all these samples showed a clear jump in the conductivity at a critical film thickness of 4 ML. More details on the growth conditions and the results of the electrical characterization are described in the literature.[29,75,89]

The structural and electrical properties of these samples were significantly better than those of the best samples prepared at the ESRF. This is partially due to the sophisticated growth monitoring by means of RHEED in the PLD system in Naples. A differential pumping system protects the sensitive filament

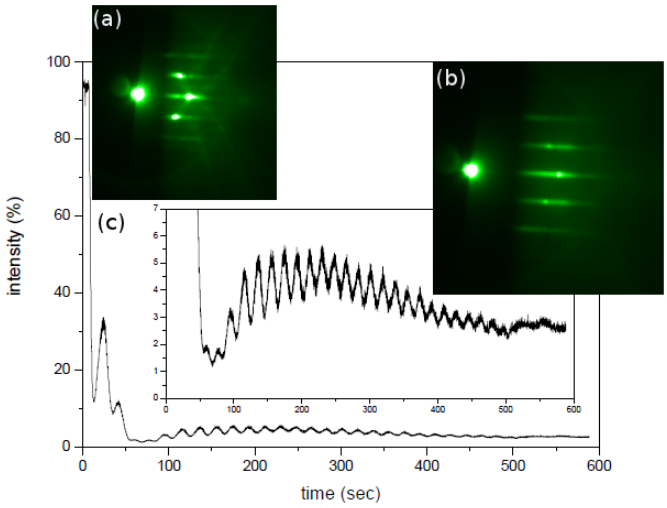

Figure 4.8.: RHEED investigations during PLD growth of a $LaGaO_3$ film on $SrTiO_3$. (a) The photograph on the left shows the characteristic RHEED pattern of the clean $SrTiO_3(001)$ surface prior to deposition. (b) The right photograph shows an image of the RHEED screen during/after $LaGaO_3$ deposition. (c) The variations in the specular reflectivity are clearly visible up to the end of the deposition process after 500 s. For better visibility the low-intensity part is zoomed in the inset.

of the RHEED electron gun allowing the growth process to be observed in-situ even at elevated oxygen partial pressures. An example of a RHEED data set is shown in Figure 4.8. The color photographs were taken from the RHEED screen of the clean $SrTiO_3$ surface (left) prior to deposition and during deposition (right). The specular reflection as well as first-order Bragg reflections are visible in these photographs. The intensity of these reflections is recorded as a function of deposition time and shows characteristic intensity fluctuations as a function of surface roughness during film deposition. Assuming layer-by-layer growth, the number of oscillations is a direct measure of number of deposited MLs. Furthermore, the width of the reflections is a indicator of the structural quality of the deposited overlayer. Clear RHEED oscillations were observed for all of the samples investigated.

4.3. Characterization of the perovskite films

Perovskite thin films were studied by SXRD in EH1 at ID32. Additionally, HAXPES measurements were performed in EH2 of ID32. The films had a nominal thickness of 6 and 12 ML $LaAlO_3$, $LaGaO_3$ and $NdGaO_3$.

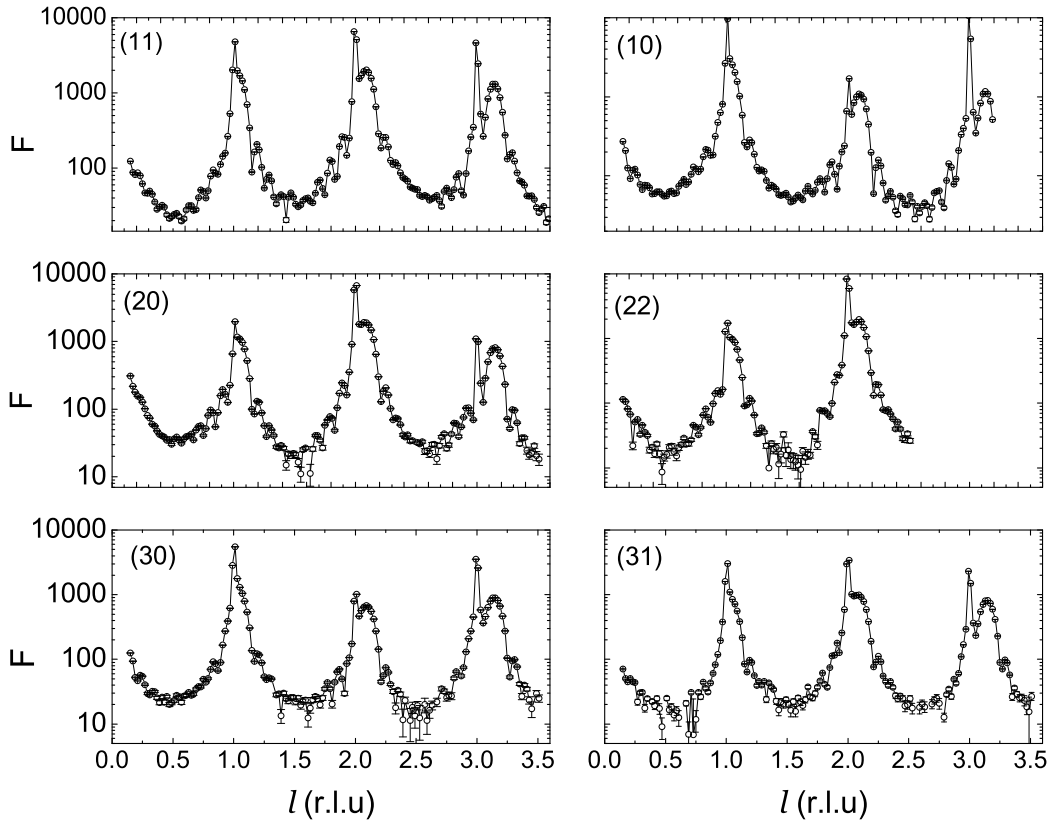

Figure 4.9.: Angle-integrated CTR scans for a nominally 12 ML thick $LaAlO_3$ film grown in Naples, Italy.

4.3.1. Surface X-ray diffraction measurements on $LaAlO_3$, $LaGaO_3$ and $NdGa0_3$ films

Crystal truncation rods (CTRs) were measured by angular scans in Θ as a function of ℓ. Superstructure rods were measured by ℓ-scans. Due to the cubic symmetry of the substrate three groups of CTRs are expected to give physically identical results: (i) all rods with h and k even (e.g. (24ℓ)) (ii) all rods with h and k odd (e.g. (13ℓ)) and (iii) all CTRs with mixed h and k (e.g. (12ℓ)). Differences within these groups arise only due to changes in the measurement geometry. All reflections are indexed with respect to the cubic $SrTiO_3$ substrate.

Integer rods

Scans along the integer CTRs for nominally 12 ML thick films are shown in Figure 4.9 for $LaAlO_3$ and Figure 4.10(a) and (b) for 12 ML $LaGaO_3$ and $NdGaO_3$

respectively. The CTRs show typical oscillations corresponding to a thickness of ~ 10 ML for $LaAlO_3$ and $LaGaO_3$ and ~ 13 ML for $NdGaO_3$. The pronounced oscillations up to high ℓ confirm the epitaxial, pseudomorphic growth of a highly coherent oxide overlayer and an abrupt interface.

The average position of the $LaAlO_3$ ($hk3$) peak at $\ell = 3.144$ r.l.u. corresponds to an average mismatch of 4.7 % or a out-of-plane lattice constant of 3.73 Å. For $LaGaO_3$ the peaks of the substrate and overlayer coincide nearly perfectly giving strong evidence for nearly perfect agreement of the cubic $SrTiO_3$ and pseudo-cubic $LaGaO_3$ lattice constants. From the average position of the $NdGaO_3$ ($hk3$) peak at $\ell = 3.052$ r.l.u. follows an average mismatch of 1.75 % or an out-of-plane lattice constant of 3.83 Å. The values found for the out-of-plane lattice constants are smaller than the values found in bulk samples (see Table 2.1).

Superstructure reflections are visible on the CTRs of $NdGaO_3$ and are indicated by arrows in Figure 4.10(b). Further measurements at half-integer positions were performed to elucidate their nature.

Superstructures of $LaGaO_3$ and $NdGaO_3$

The measurements on the $NdGaO_3$ films revealed the presence of superstructure reflections on the integer rods. Figure 4.10(b) shows the (1 1 ℓ) truncation rod with superstructure reflections at half-integer positions marked by the arrows. The additional reflections indicate a doubling of the out-of-plane lattice constant. This is consistent with a film growing with a $(\sqrt{2} \times \sqrt{2})$R45 ° superstructure. Figure 4.11 illustrates that further reflections are expected for rods with h and k both half-integer. As an example, the (½ ½ ℓ), (1½ ½ ℓ) rods are shown in Figure 4.12(a-d). Peaks are visible at the expected positions.

Additional peaks are also observed on the (0 ½ ℓ) rods. A representative in-plane scan of a $NdGaO_3$ sample in k along (2 k 0.05) is shown in Figure 4.10(c). Several reflections appear along this line scan. The reflections at half-integer positions cannot be explained by a $(\sqrt{2} \times \sqrt{2})$R45 ° superstructure. They indicate a doubling of the in-plane lattice constant and hence point to the **c**-axis being aligned in the surface with one of the $SrTiO_3$ in-plane axes **a** and **b**. The observed reflections correspond to a (2×1) double-domain superstructure. (see Fig. 4.11) This leads to the conclusion that two film growth orientations are competing. The comparable intensity in symmetrically equivalent reflections indicates that there is no preference for either orientation. From the in-plane width of the superstructure reflections we can estimate a domain size of ∼170 Å.

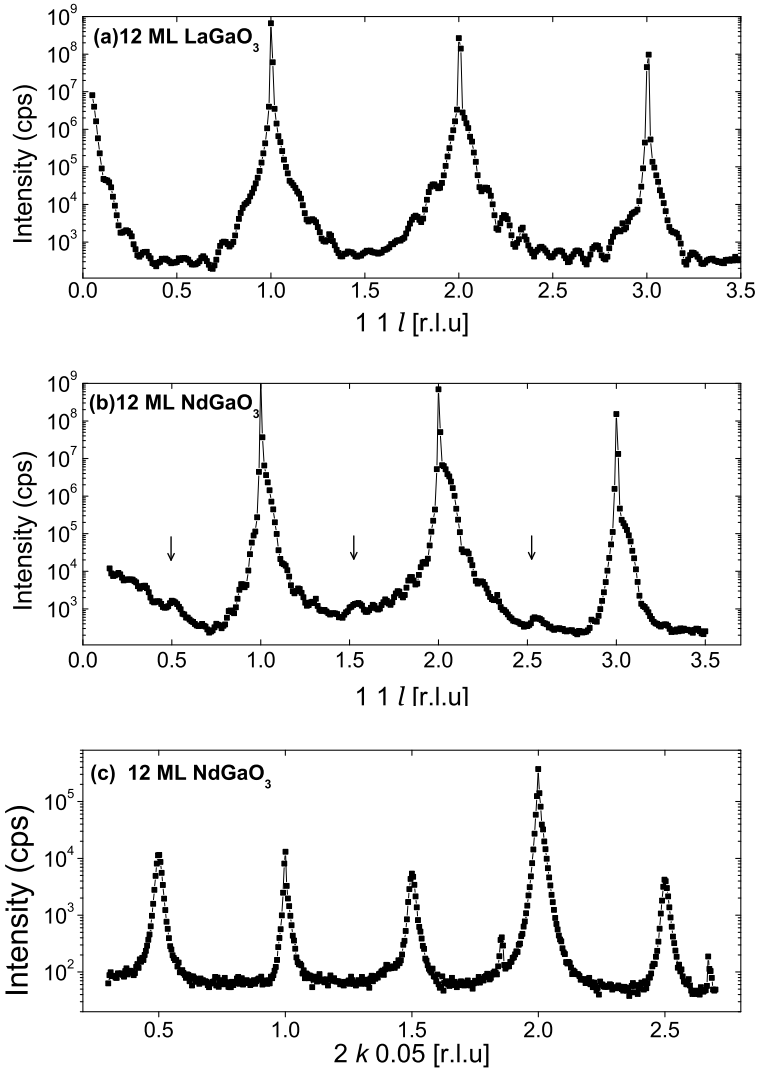

Figure 4.10.: ℓ-scan along the (1 1 ℓ) rods of nominally 12 ML thick films (a) $LaGaO_3$ and (b) $NdGaO_3$ show pronounced thickness oscillations. For the $NdGaO_3$ film superstructure reflections at half-integer ℓ values are marked with arrows. An in-plane scan (c) for the $NdGaO_3$ film along (2 k 0.05) shows symmetrical peaks at integer and half-integer positions.

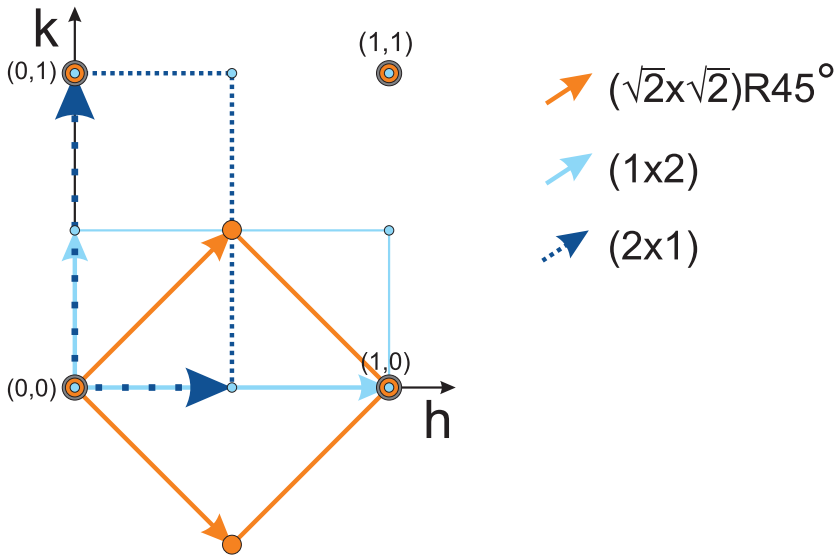

Figure 4.11.: The epitaxial relations of the orthorhombic films to the cubic $SrTiO_3$ substrate.

In the $LaGaO_3$ samples we could not find any evidence for the $(\sqrt{2} \times \sqrt{2})R45^\circ$ superstructure. This was confirmed by the absence of the superstructure peaks on the ℓ-scans at integer h and k in Figure 4.10 (a) and other reflections that are unique to this superstructure, like ($1/2$ $1/2$ 1) (see Fig. 4.12(a)). The $LaGaO_3$ films grow in a pure (2×1) double domain structure. Sharp spikes in the spectra were found to belong to powder rings. Similar features can sometimes be found for $LaAlO_3$ films (see also Fig. 4.6(c)) and have been assigned to poorly oriented grains on the surface.

To summarize, the distribution of the superstructure spots cannot be explained by one simple model. For $NdGaO_3$ a combination of two different epitaxial relationships for the orthorhombic overlayer is necessary to explain all of the observed reflections. For the thicker film, the $NdGaO_3$ superstructure reflections shift to lower ℓ-values and the peak widths decrease. Similar to the substrate rods, oscillations are found for the superstructure rods. These three observations are evident from Figure 4.12(f)) showing the ($0 1/2 \ell$) superstructure rod for the 6 ML and 12 ML thick $NdGaO_3$ films in comparison.

For both $LaGaO_3$ and $NdGaO_3$ the oscillations on the superstructure rods were found to match those on the integer rods and correspond to the thickness of the films. Therefore, both superstructures are present over the whole film thickness.

The width of the peaks give an additional estimate of the film thickness. For the 6 ML $NdGaO_3$ film the average width is 0.102 r.l.u. ±0.0124 r.l.u., for the

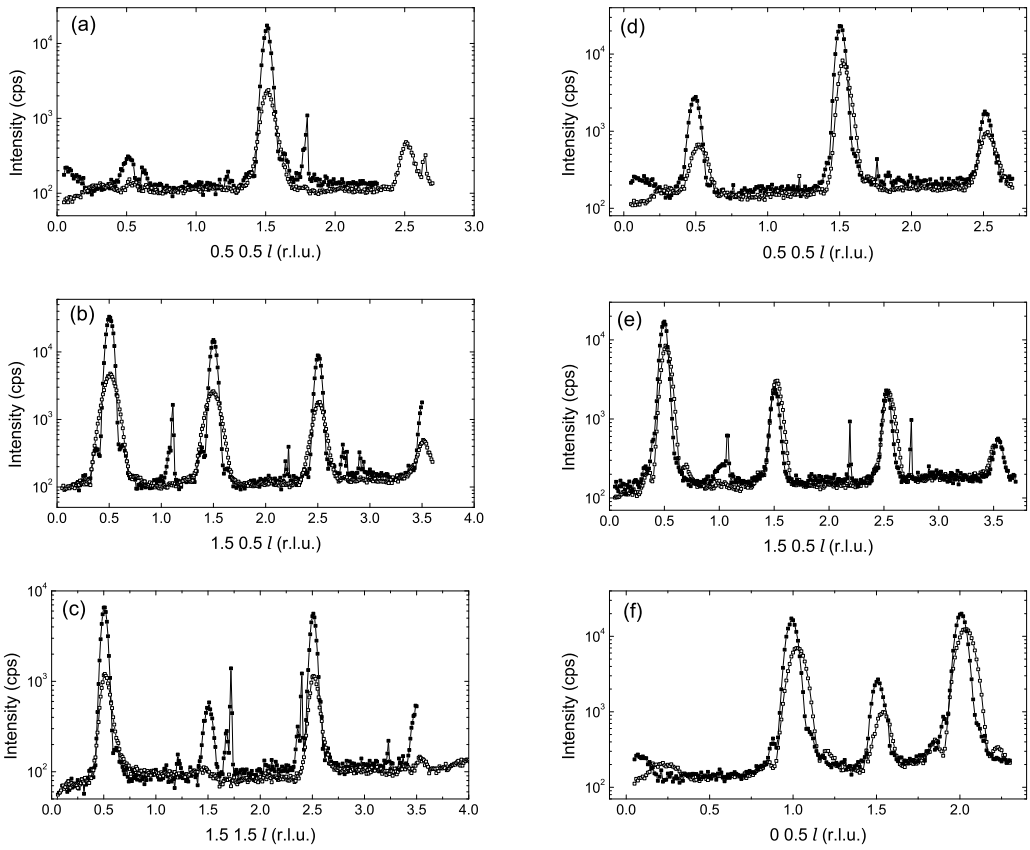

Figure 4.12.: Scan in ℓ along the superstructure rods for two different film thicknesses (open symbols: 6 ML, closed symbols: 12 ML) (a-c) for $LaGaO_3$ and (d-f) for $NdGaO_3$.

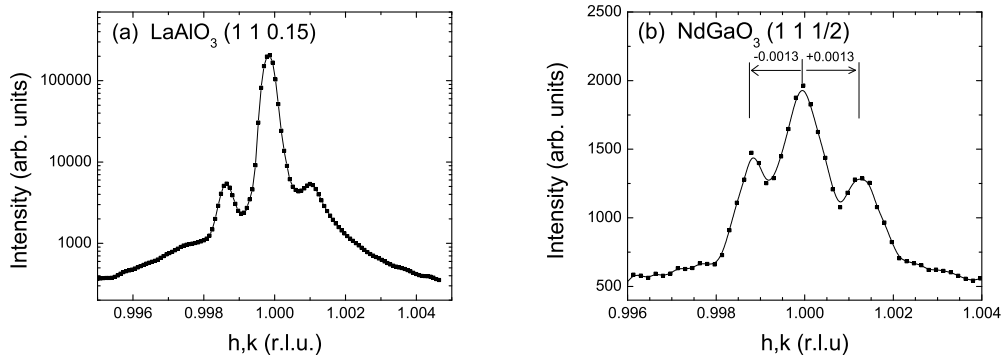

Figure 4.13.: Projections of mesh scans in the hk-plane around the (11ℓ) CTR at $\ell = 0.15$ r.l.u. for a 5 ML $LaAlO_3$ film and $\ell = 0.5$ r.l.u. for a 6 ML $NdGaO_3$ film.

12 ML $NdGaO_3$ film the average width is reduced to 0.0757 r.l.u. $\pm$0.0045 r.l.u.. From these values we calculate thicknesses of 38.28 Å($\sim$ 9.8 UC) and 51.5 Å($\sim$ 13.2 UC) respectively. The real thicknesses are overestimated, especially for the thinner film, indicating other contributions to peak broadening are present such as mosaicity and strain.

A detailed structural analysis of the different oxide films would have been interesting. However, due to the multidomain structure the time for the acquisition of a reasonable data set would have exceeded the amount of available beam time.

Satellite peaks

Double peaks are visible in angular scans through the CTRs. Reciprocal space maps (RSMs) were measured around the (11ℓ) reflections at $\ell = 0.15$ r.l.u. and 0.5 r.l.u. in the hk-plane. All RSMs appear to be stretched in the hk-direction. The stretching is due to the instrument resolution function which, in this geometry, is mainly defined by the in-plane detector slits. For better comparison projections of the RSMs are shown in Figure 4.13(a) and (b) for $LaAlO_3$ and $NdGaO_3$.

Detailed analysis around the (11ℓ) Bragg reflection revealed a fine structure in the tails of the Bragg reflections. Additional intensity is distributed symmetrically around the in-plane Bragg peak at (1 1 0.15) of the $LaAlO_3$ film as well as at higher ℓ at a constant distance of $\sim$ 0.002 r.l.u.; for $NdGaO_3$ (1 1 ½) the splitting is 0.0013 r.l.u. i.e. slightly smaller. This corresponds to a periodic modulation in the film or the substrate with a periodicity of $\sim$ 300 nm and $\sim$ 200 nm for $LaAlO_3$ and $NdGaO_3$ respectively.

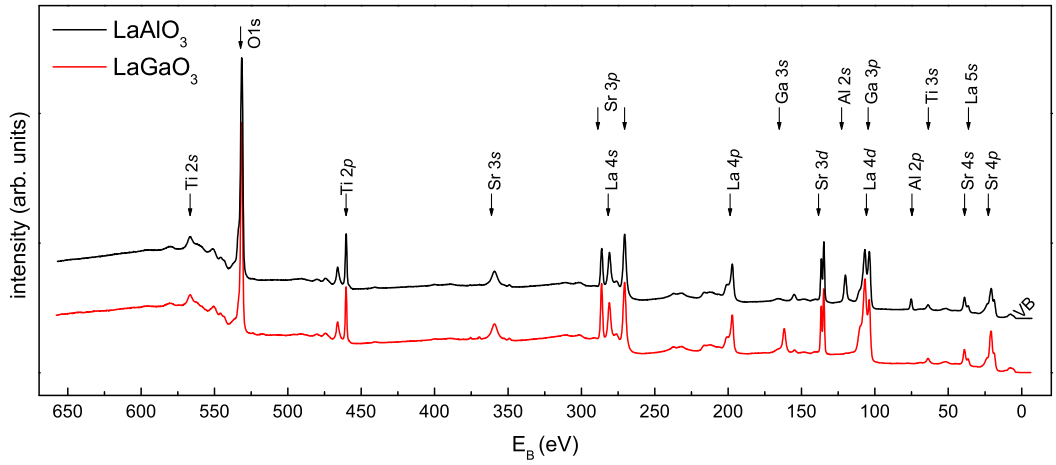

Figure 4.14.: Comparison of HAXPES survey spectra for 5 ML thick $LaAlO_3$ (black, top) and $LaGaO_3$ (red, bottom) films for the binding energy range from 660 eV to −5 eV measured with a beam energy of 2.75 keV. The spectra are offset to improve the visibility of the peaks.

The satellite peak can arise from (i) a periodic dislocation network[113] in the overlayer or (ii) periodic distortions in the $SrTiO_3$ substrate.[114] Boschker *et al.*[114] observed similar features on 8–19 nm thick $LaAlO_3$ films. They argue that in their $LaAlO_3$ samples the dislocation density necessary to explain the observed satellites does not agree with the in-plane mismatch they observed in their samples.

In the case of $NdGaO_3$, the intensity at and around the (1 1 ½) reflection originates mainly from the $NdGaO_3$ film. Contributions from the $SrTiO_3$ can be excluded. The satellites have to originate from a periodic dislocation network in the $NdGaO_3$ film. We are inclined to argue that the satellites in the $LaAlO_3$ film also originate from dislocation networks in the overlayer.

4.3.2. Characterization by hard X-ray photoelectron spectroscopy

HAXPES spectra were recorded from the $LaAlO_3$, $NdGaO_3$ and $LaGaO_3$ thin film samples. Survey spectra from 6760 eV to −5 eV binding energy are presented in Figure 4.14 for 5 ML thick $LaAlO_3$ and $LaGaO_3$ films. The individual core levels are marked by arrows and the corresponding orbitals are indicated. The spectra show all of the expected core level lines from the film and the substrate and a weak carbon contamination probably due to the exposure to air. The substrate peaks are still very well visible.

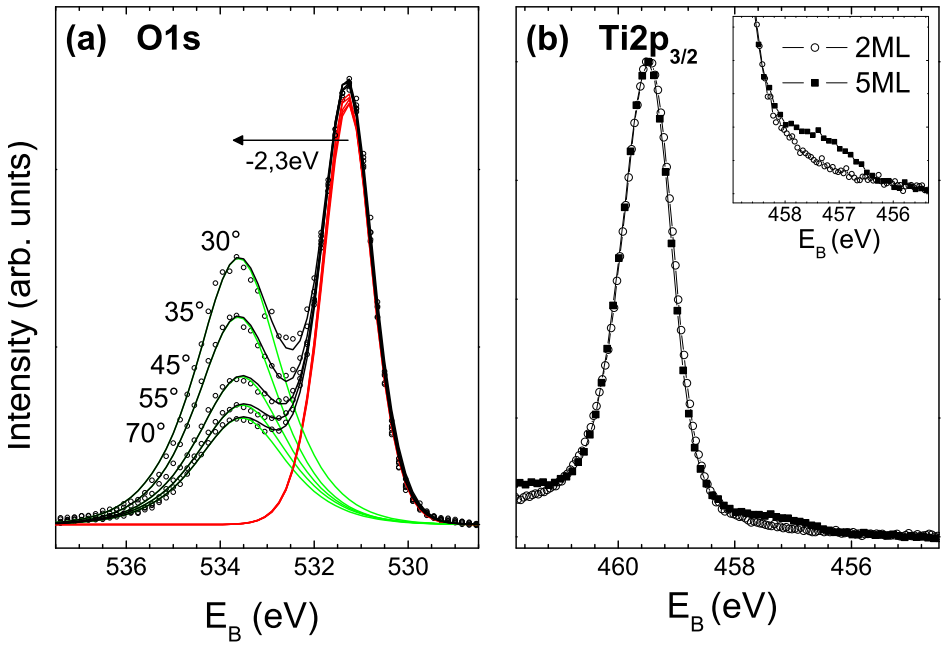

Figure 4.15.: (a) O 1*s* core level spectra show a high binding energy shoulder with a pronounced angle dependence indicative of OH-groups adsorbed on the $LaAlO_3$ surface. (b) Ti 2*p* spectra from $LaGaO_3$ in comparison to a $LaAlO_3$ film.

In particular the O 1*s* and Ti 2*p* core levels show additional features and in the valence band region a signature of the 2DEG is expected close to E_F. In fact, data from both the 5 ML and the 12 ML thick $LaAlO_3$ films reveal the presence of a clear Fermi level and a weak feature $\sim 1.3\,\text{eV}$ below E_F. Equivalent results were also found for $LaGaO_3$ films grown on $SrTiO_3$. A detailed discussion will be presented in Section 4.5.

Despite the good diffraction data measured for the $NdGaO_3$ films, HAXPES measurements remained very challenging due to charging problems that result in shifts of the core level positions. This suggests, that conductivity was not preserved during the transport to the ESRF. Nevertheless, core level spectra for O 1*s* and Ti 2*p* were measured also on one $NdGaO_3$ film.

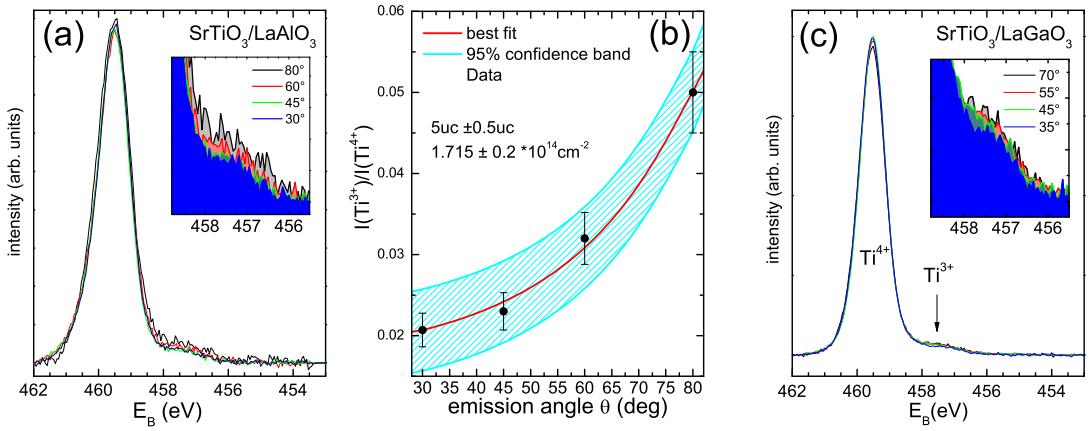

Figure 4.16.: Angle dependent Ti $2p$ spectra for (a) $LaAlO_3$ and (c) $LaGaO_3$ thin films. (b) shows best fit results of Eq. 4.1 to the $I^{(3+)}/I^{(4+)}$ ratio. The 95% confidence band is shaded in light blue and contains the error bars estimated from multiple measurements

O 1s core levels

A series of O 1s core level spectra for different take-off angles is shown in Figure 4.15(a). The spectra are exhibit 2 components. The main line is found at a binding energy of 530.5 eV and the second component has a $\sim$ 2.3 eV higher binding energy. The high-energy component has a pronounced angle dependence suggesting that this contribution originates from the surface. In agreement with observations on other metal oxide surfaces (see also Chapter 6 for similar features on $a_{0.65}Sr_{0.35}MnO_3$ films) and the $LaAlO_3/SrTiO_3$ samples,[115] the additional feature is assigned to surface bound hydroxyl groups.[1]

Ti 2p core levels

For all samples, independent of the doping mechanism, Ti $2p$ core levels exhibit a shoulder associated with Ti^{3+} was found at $\sim$ 2.3 eV lower binding energy of the Ti^{4+} main line.

[1]Samples exposed to air for the same amount of time seem to show a more pronounced hydroxide peak for thicker films (e.g. the 2 ML and 5 ML films used for the XSW imaging). OH-adsorption might be enhanced for thicker samples due to a higher remaining surface potential. Additionally, hydroxyl groups may adsorb more readily due to the positive charge accumulated on the surface[57] due to oxygen vacancies.

Figure 4.15(b) shows Ti $2p$ spectra for nominally 2 ML and 5 ML thick $LaAlO_3$ films measured at a beam energy of 3.2 keV. The resulting probing depth 3λ at normal emission is ~ 140 Å. The spectra show one strong peak originating from the Ti $2p_{3/2}$ line at a binding energy (E_B) of 459.5 eV and for the 5 ML film a shoulder is visible on the low binding energy side of the Ti $2p_{3/2}$ main peak. The shoulder is attributed to a reduction in valence state, i.e. $Ti^{4+} \rightarrow Ti^{3+}$ due to the electron doping at the $LaAlO_3/SrTiO_3$ interface.

Thick $LaGaO_3$ films show a similar shoulder as shown in Figure 4.16(c). $NdGaO_3$ films did not show any shoulder on the Ti $2p$ core level. The absence of the shoulder in the $NdGaO_3$ sample agrees with the observation of charging effects on this sample.

Ti $2p$ core levels were studied as a function of the emission angle (Fig. 4.16(a) and (c)). The angle dependent measurements show an enhancement of the Ti^{3+} feature for the surface sensitive geometries. A detailed analysis of angle dependent Ti $2p$ spectra was presented by Sing and coworkers.[74] The ratio of the main peak to the shoulder $I(3+)/I(4+)$ is described by

$$\frac{I(3+)}{I(4+)} = \frac{p\,[1 - \exp\,(-d/\lambda \cos\theta)]}{1 - p\,[1 - \exp\,(-d/\lambda \cos\theta)]} \tag{4.1}$$

where p is the fraction of Ti^{3+} ions per unit cell and d is the thickness of the conducting layer. Hence, the ratio p and thickness d can be obtained by fitting the equation against the experimentally obtained $I(3+)/I(4+)$ ratios. Under the assumption, that each electron at the interface cause the reduction of a Ti atom to Ti^{3+}, the sheet carrier concentration is obtained by multiplying p and d. As a matter of fact this is not totally true, because electrons trapped at vacancies will contribute to the Ti^{3+} states, but are too tightly bound to participate in the conduction process.[102] This should lead to an overestimate of the sheet carrier density.

For the 5 ML $LaAlO_3$ sample a thickness of ~ 5 ML for the 2DEG (Fig. 4.16(b)) and a sheet carrier density of $1.715 \times 10^{14}\,cm^{-2}$ is estimated. These values are in very good agreement with the results obtained from $LaAlO_3$ films by various methods[72,74] and are in excellent agreement with the electrical characterization of such samples.[89] The $LaGaO_3$ film also shows an angular dependence (see Fig. 4.16(c)) but it is much less pronounced. This indicates that the thickness of the conductive layer exceeds the probing depth. The chosen preparation conditions were the same as for $LaAlO_3$ films and did not allow bulk oxygen vacancy formation. It can be concluded that the conductive layer is confined to the interfacial region, however, extending to a depth exceeding the mean free path of the photoelectrons.

These measurements confirm (i) that only samples above the critical thickness show significant charge carriers, (ii) the charge carriers are confined to the interface

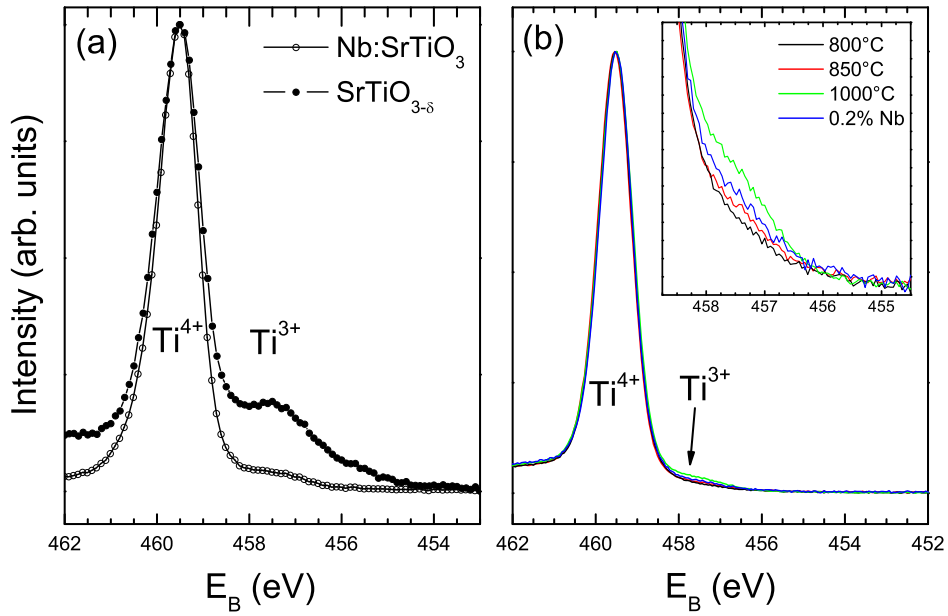

Figure 4.17.: Ti $2p$ core level spectra for (a) Nb:$SrTiO_3$ (open circles) and $SrTiO_{3-\delta}$ and (b) a series of Ti $2p$ core level spectra for $SrTiO_3$ annealed at increasing temperatures.

region and (iii) cannot be explained by vacancies distributed in the bulk of the $SrTiO_3$ substrate.

Figure 4.17(a) shows the Ti $2p$ spectra of the $SrTiO_3$ samples studied by XSW valence band decomposition in Section 4.5. The ratio of the main peak to the shoulder $^{I(3+)}/_{I(4+)}$ provides a measure of the charge carriers. For Nb:$SrTiO_3$ we obtain a ratio of 0.048±0.01 and for $SrTiO_{3-\delta}$ 0.318 ± 0.01. The average Ti^{3+}/Ti^{4+} ratio within the $\approx 2\,nm$ interface region is 0.053 ± 0.002 and thus is comparable to the carrier density which we measured on the Nb:$SrTiO_3$ sample.

In Figure 4.17(b) we present a series of Ti $2p$ spectra for $SrTiO_3$ samples subjected to different annealing temperatures (800 °C, 850 °C and 1000 °C) for $\sim 30\,min$ at pressures below $10^{-8}\,mbar$. This annealing treatment creates oxygen vacancies in $SrTiO_3$ bulk structure. A shoulder on the low binding energy side of the Ti $2p_{3/2}$ main peak develops as a function of annealing temperature. For comparison a 0.2 atm. % Nb-doped sample is shown as well. With increasing annealing temperature we observed that the samples became darker in color, consistent with the optical band gap becoming smaller.

4.3.3. Conclusions

Epitaxial films of $LaAlO_3$, $LaGaO_3$ and $NdGaO_3$ grow with high crystalline order on $SrTiO_3$. For the orthorhombic $LaGaO_3$ films, epitaxy occurs with the pseudo-cubic **c**-axis out-of-plane resulting in a $(\sqrt{2}\times\sqrt{2})R45^\circ$ superstructure. In $NdGaO_3$ the **c**-axis can be oriented in-plane, resulting in a (2×1) double-domain like superstructure with the **a** and **b**-axis pointing 45° away from the surface. The films show a larger **c** lattice constant for thinner films. Furthermore, we observed satellite structures around the film Bragg peaks indicating that a dislocation network assists in accommodating in-plane strain.

HAXPES measurements showed a hydroxide related high binding energy shoulder on the O 1*s* core levels for all samples. The low binding energy Ti 2*p* shoulder gives evidence of the filling of the interfacial Ti 3*d* bands. Analysis of the angle-dependent behavior shows that the shoulder originates from the interface region. The 2DEG thickness was found to be 5UC, with a sheet carrier density of $1.7\times10^{14}\,\mathrm{cm}^{-2}$, as obtained by fits to the angle-dependent data. These results agree very well with the literature[72–74] and transport measurements on samples grown under identical conditions.[89] For $LaGaO_3$, the conductive layer appears to be much thicker, but remains localized at the interface. $NdGaO_3$ films are not very stable under atmospheric conditions and show charging effects in XPS and the Ti 2*p* shoulder was not observed on these samples.

4.4. XSW-imaging of distortions in $LaAlO_3$

Structural details of $LaAlO_3$ films on $SrTiO_3$ were revealed using the XSW imaging technique. Model-free real space images were reconstructed, showing significant distortions in the $LaAlO_3$ overlayer. Subsequent model refinement yielded the lattice distortions along the interface with high precision and also revealed the OH adsorption site on the surface of the films. This investigation demonstrates that it is possible to determine the element-specific lattice distortions in metal oxide thin films with high resolution.

This section is focused on $LaAlO_3$ thin films below (2 ML) and above (5 ML) the critical thickness for conductivity. In addition, preliminary measurements on $LaGaO_3$ films are presented. The first part presents the analysis of the XSW modulated core level photoelectron yield for the five elements present in the film and the substrate. For each reflection and element the amplitude and phase of the Fourier coefficient of the elemental atomic distribution function is extracted. In the second part, 3-dimensional real space images of the atomic distribution are

reconstructed by direct Fourier inversion for each of the elements in the $LaAlO_3$ films. These images reveal significant atomic displacements and buckling of the cation-oxygen planes for both samples. The third part demonstrates how the individual positions of all of the oxygen and cation sites can be obtained with the help of a model refinement. The refined model was tested against SXRD data obtained from the same samples.

4.4.1. Extraction of Fourier components

The XSW modulated core level photoelectron yield was recorded for the La $3d$, Al $1s$, O $1s$, Sr $3s$ and Ti $2p$ core levels for seven different Bragg reflections. The circles in Figure 4.19 show the raw data for the 2 ML and 5 ML thick $LaAlO_3$ films. The differences in the yield curves for the cations in the film (La,Al) and the substrate (Sr,Ti) indicate deviations from the substrate positions for the elements in the film. Significant differences are apparent between the 2 ML and 5 ML thick samples. For the $LaGaO_3$ films the La $3d$, O $1s$, Ti $2p$ and Ga $3s$ core levels were studied for the $SrTiO_3$ (111) reflection. The circles in Figure 4.18 show the raw data for 6 ML and 12 ML $LaGaO_3$ films.

In the further analysis, for each reflection the amplitude, f_H, and phase, P_H, of one Fourier coefficient of the elemental atomic distribution function $\rho(r)$ were obtained by fitting Eq. 2.26 to the experimental photoelectron yield curves. The best fit results are plotted as lines in Figure 4.18 and Figure 4.19. The fitted values for f_H and P_H are summarized in Tables 4.2 and 4.3 for the $LaAlO_3$ films and in Table 4.4 for $LaGaO_3$. It should be noted that the values are close to those measured for the substrate cation on the same crystallographic site. The positions lie mostly below the $SrTiO_3$ position and also the coherent fraction is reduced. The similar coherent fractions indicate a similar degree of order with respect to the $SrTiO_3$ lattice. The high coherent fractions give further evidence of high coherence and good epitaxy.

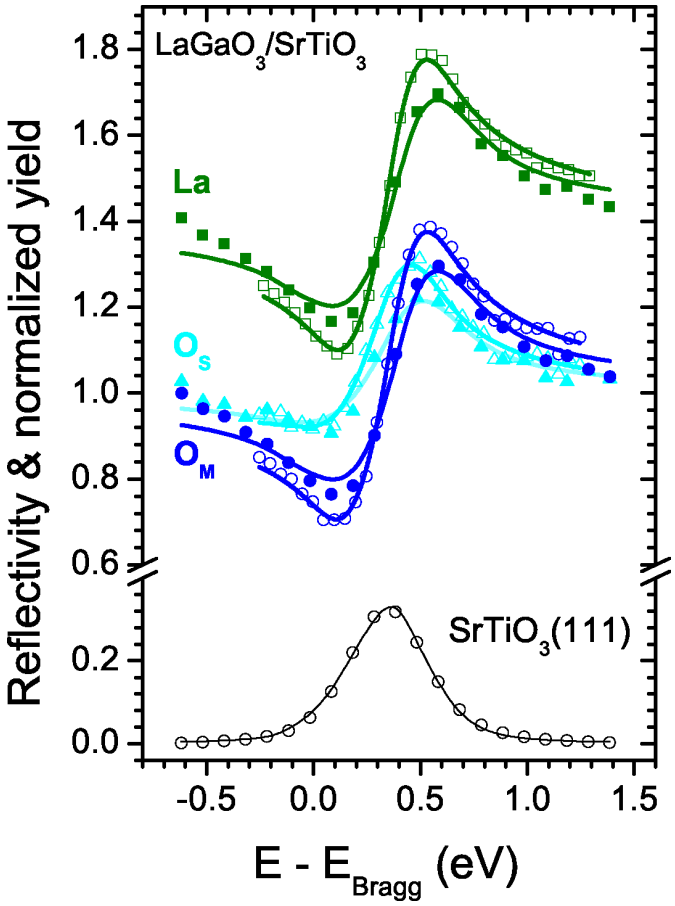

Figure 4.18.: XSW measurements of the La 3*d* (green) and O 1*s* core levels (dark: main peak; light: side peak) for the 6 ML (open symbols) and 12 ML (closed symbols) $LaGaO_3$ films using a $SrTiO_3(111)$ reflection in back scattering geometry (hν=2.75 keV). The curves for La are offset by 0.4 in y for better visibility.

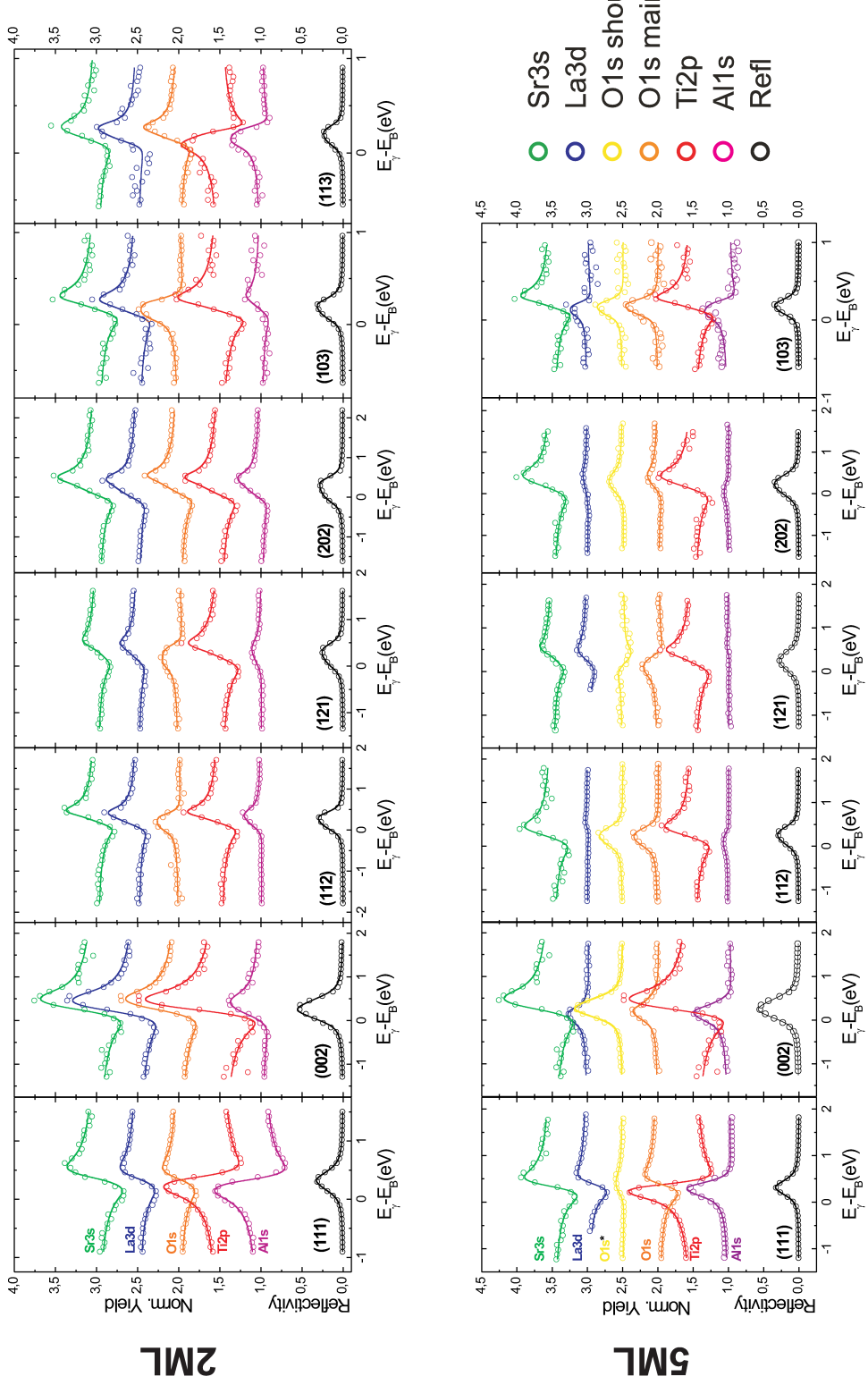

Figure 4.19.: Results from XSW measurements on a 2 ML and a 5 ML thick $LaAlO_3$ film. Data (circles) and best fits (lines) are shown for all elements in the film and substrate for the (111), (002), (112, (121),(113) and (103) reflections of $SrTiO_3$.

Table 4.2.: Best fit results for the XSW results of a 2 ML $LaAlO_3$ film. The corresponding fits and data are shown in Figure 4.19.

	Al 1*s*		**La** 3*d*		**O** 1*s*		**Ti** 2*p*		**Sr** 3*s*	
(hkl)	fH	PH	fH	PH	fH	PH	fH	PH	fH	PH
(111)	0.92	0.57	0.68	0.95	0.66	0.94	0.90	0.53	0.90	0.99
(002)	0.42	0.93	0.73	0.03	0.64	1.00	1.08	0.01	0.82	0.99
(112)	0.21	0.88	0.66	0.02	0.25	0.53	0.99	1.00	0.96	0.99
(121)	0.34	0.83	0.56	0.94	0.39	0.62	1.05	0.99	···	···
(202)	0.54	0.96	0.61	0.01	0.45	0.02	0.94	0.99	1.01	0.00
(113)	0.50	0.43	0.63	0.01	0.88	0.02	1.10	0.50	0.82	0.02
(103)	0.36	0.93	0.70	0.05	0.41	0.47	1.02	0.02	0.92	0.01

Table 4.3.: Best fit results for the XSW results of a 5 ML $LaAlO_3$ film. The corresponding fits and data are shown in Figure 4.19.

	Al 1*s*		**La** 3*d*		**O** 1*s* **main**		**O** 1*s* **side**		**Ti** 2*p*		**Sr** 3*s*	
(hkl)	fH	PH	fH	PH	fH	PH	fH	PH	fH	PH	fH	PH
(111)	0.38	0.44	0.77	0.9	0.86	0.93	0.32	0.87	1.13	0.49	0.79	0.99
(002)	0.27	0.63	0.37	0.73	0.26	0.73	0.086	0.34	···	···	···	···
(112)	0.45	0.75	0.56	0.8	0.15	0.45	0.09	0.41	0.99	0.99	0.96	0.99
(121)	0.56	0.80	0.65	0.89	0.42	0.64	0.7	0.73	···	···	···	···
(202)	0.54	0.76	0.57	0.80	0.53	0.86	0.31	0.84	0.95	0.99	0.89	0.98
(103)	0.43	0.57	0.30	0.67	0.21	0.40	0.085	0.48	···	···	···	···

Table 4.4.: Best fit results for the XSW data for 6 ML and 12 ML thick $LaGaO_3$ films for the $SrTiO_3$ (111)-reflection. The corresponding data and fits are given in Figure 4.18.

	6 ML		**12 ML**	
	P_H	f_H	P_H	f_H
La 4*p*	0.994	0.89	0.971	0.65
O 1*s*-1	0.995	0.89	0.971	0.661
O 1*s*-2	1.011	0.41	0.954	0.366
Ti 2*p*	0.502	0.97	0.505	0.96
Ga 3*s*	0.485	0.86	···	···

Removal of the oxygen contribution from the substrate

The O 1*s* spectra contain contributions from oxygen in the film and oxygen in the $SrTiO_3$ substrate. The position derived from the XSW data can be corrected for this factor to obtain the true position of the oxygen atoms in the film.

The Fourier components (f_H, P_H) for oxygen can be decomposed into a sum of the contributions from the film and the substrate using Eq. 2.34. The relative contributions from the film and the substrate $I_{\mathrm{LaAlO_3}}$ and $I_{\mathrm{SrTiO_3}}$ were estimated from Eqs. 2.21 and 2.22.

For the perovskite films the mean free path varies only slightly for the different materials. Setting $\lambda_{\mathrm{SrTiO_3}} = \lambda_{\mathrm{LaAlO_3}} = \lambda_A$ and $I^{\infty}_{\mathrm{LaAlO_3}} = I^{\infty}_{\mathrm{SrTiO_3}}$ reduces Eqs. 2.21 and 2.22 to

$$I_{\mathrm{SrTiO_3}} = \exp^{-d/(\lambda_A * \sin\theta)} \quad (4.2)$$

$$I_{\mathrm{LaAlO_3}} = 1 - \exp^{-d/(\lambda_A * \sin\theta)}. \quad (4.3)$$

The take-off angle, the mean free path λ, and $\mathrm{I_{LaAlO_3}/I_{SrTiO_3}}$ ratio are summarized for all of the relevant reflections (hkl) in Table 4.5.

In the following only the substrate-corrected Fourier coefficients will be employed.

4.4.2. Results from 5 ML and 12 ML thick $LaGaO_3$

The (111) reflection is tilted with respect to the surface, thus information on the coherence in both in-plane and out-of-plane direction are accessible in this geometry. Nevertheless, the XRD results presented above showed that the films

Table 4.5.: Experimental parameters for each reflection (*hkl*) the photon energy $h\nu$, the take-off angle θ, the inelastic mean free path λ, and the substrate/film ratio are given.

(hkl)	hν	θ	λ	ratio 5 ML	ratio 2 ML
(1 1 1)	2.75	45	41.5	0.490	0.678
(0 0 2)	3.17	6	46.6	0.014	0.096
(1 1 2)	3.89	35.26	55	0.278	0.848
(1 2 1)	3.89	65.9	55	0.660	0.797
(2 0 2)	4.49	45.0	61.9	0.620	0.771
(1 0 3)	5.02	18.43	67.9	0.378	0.588
(1 1 3)	5.27	16.43	70.6	0.351	0.565

are uniformly strained in-plane. Consequently, no in-plane displacements are expected and the coherent position can be directly translated to a position along the **c**-axis.

For distances larger than the XSWs periodicity, the coherent position does not give a unique answer. Structural information is averaged over the entire film thickness. Assuming a linear displacement with distance from the interface, we can estimated the mismatch to the sites of the extended $SrTiO_3$ lattice. The coherent position of 0.97 found in the 12 ML film corresponds to approximately 0.48 % mismatch per ML. For the 6 ML film the position of 0.994 corresponds to a mismatch of $\sim$ 0.4 %. The smaller mismatch for the thinner film indicates a possible expansion of the unit cell closer to the interface due to the build-up of electrostatic charge. A similar behavior was observed by diffraction for the $NdGaO_3$ films and in the imaging results of the $LaAlO_3$ films presented in the following.

Although the orthorhombic $LaGaO_3$ structure exhibits distortions between the $GaO_{6/2}$ octahedra, the octahedra themselves remain nearly undisturbed (bond angle 90.3 ° and 89.7 °). Therefore, the oxygen distribution around the cation sites can be approximated to be symmetric with respect to the (111) lattice planes. Thus, coherent positions are expected to be identical for the lanthanum A-site and oxygen. In comparison, the multiple oxygen sites with respect to the $SrTiO_3$(111) lattice planes are expected to reduce the coherent fraction. The XSW results show identical coherent positions and fractions for O and La. At first sight, this would indicate undistorted octahedra. But, there are significant contributions from the $SrTiO_3$ substrate to the signal.

For a quantitative approach, the contribution from bulk oxygen was estimated by comparing the core-level intensities from the $LaGaO_3$ film with measurements on Nb-doped $SrTiO_3$. The bulk contribution was found to be $\approx$45 % of the total

O1s signal and the measured Fourier components for oxygen were decomposed into the contributions from the film and the substrate.

The corrected values are f_H=0.424 and P_H=0.914. The average O position is hence about 0.22 Å below the lanthanum position indicating distortion of the LaO planes.

4.4.3. 3-dimensional real space images of $LaAlO_3$ films

Contrary to standard X-ray diffraction measurements, in the XSW technique the amplitude *and phase* of the Fourier coefficients of the atomic distribution function for each reflection are determined. Consequently, XSWs present an elegant way around the phase problem in X-ray crystallography. This means that, if a sufficient number of Fourier components are known, the atomic distribution function can be directly reconstructed by using Eq. 2.33. In this way model-free 3-dimensional images of the $LaAlO_3$ overlayers were obtained.

The SXRD measurements presented before in Section 4 confirmed a pseudomorphic growth of the $LaAlO_3$ overlayers for all film thicknesses. In this case the film will follow the substrate symmetry. The loss of periodicity at the surface reduces the bulk symmetry *Pm3m* to *P4mm* for the $SrTiO_3$ (001) surface. Applying this symmetry to the measured data gives 29 and 25 Fourier components of the atomic distribution function for each element for the 2 ML and 5 ML thick films, respectively.

From these data sets, model-free 3-dimensional real space images of the atomic distribution function were reconstructed for all of the elements in the samples. Figure 4.20 shows 3-dimensional views of the atomic distribution function and Figure 4.21 a set of contour plots cut along prominent planes in the structure. The images reveal significant atomic displacements with respect to the position in the $SrTiO_3$ substrate. The comparison for 2 ML (non-conducting) and 5 ML thick (conducting) samples show a significant increase of the overall atomic displacements with increasing film thickness. The center of the areas with maximum intensity are summarized in Table 4.6 and represent the average of all cation sites occupied throughout the film with respect to the substrate lattice. Positions are described with respect to the extended $SrTiO_3$ lattice.

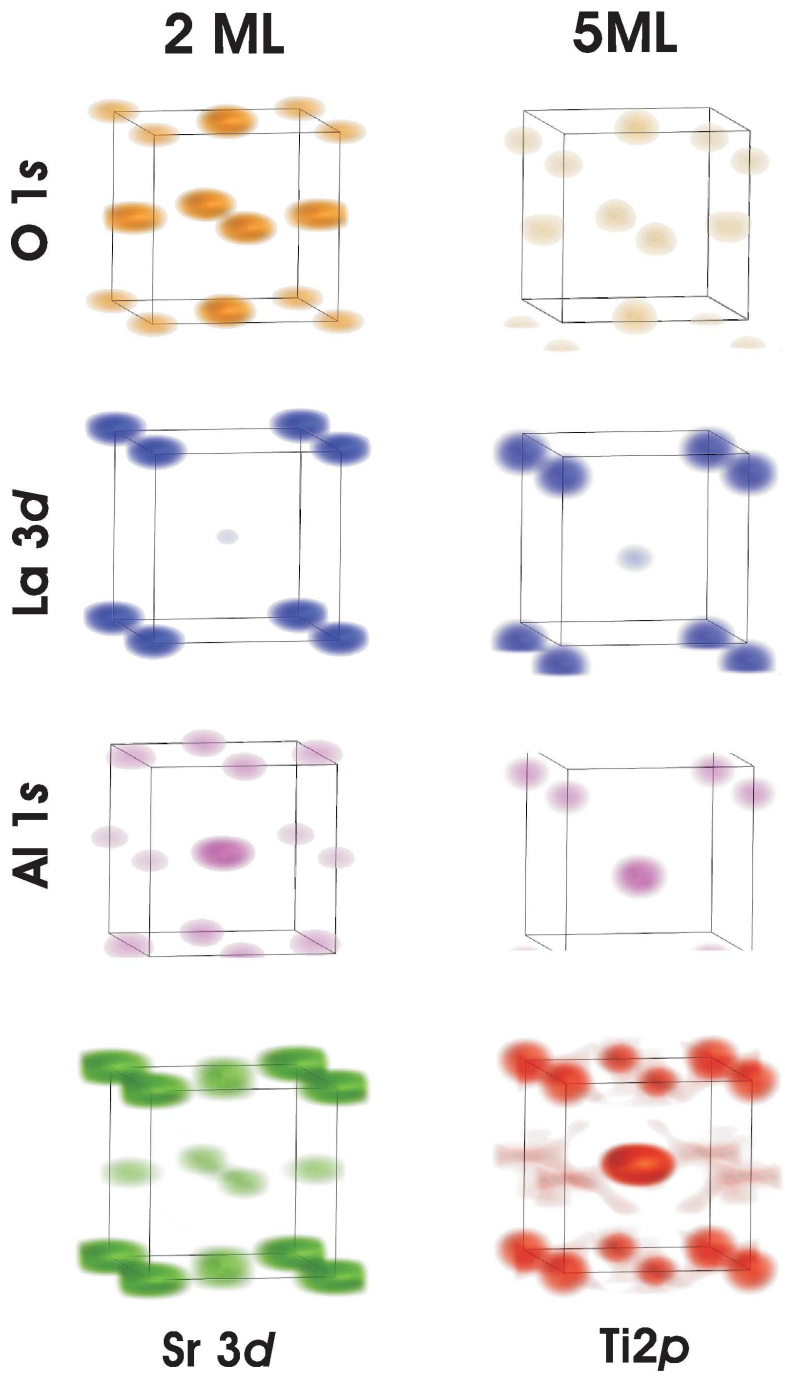

Figure 4.20.: Direct XSW images as calculated from the raw data for the 2 ML and 5 ML films. Artifacts due to missing Fourier components are apparent in these raw images. The black boxes indicate the unit cell of the extended $SrTiO_3$ substrate.

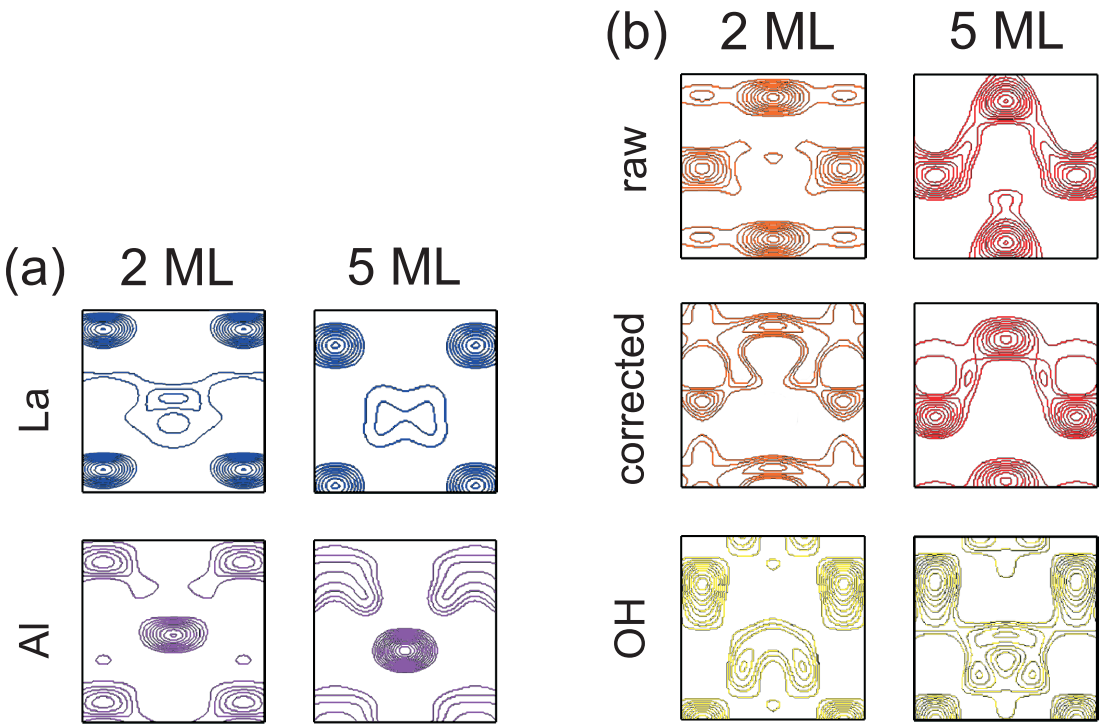

Figure 4.21.: Contour plots for 2 ML and 5 ML films for (a) the cations and (b) the oxygen. For oxygen, the plots were calculated from the raw data, the substrate corrected data and the OH-feature. The planes were chosen parallel to the **c**-axis and perpendicular to the **b**-axis. For La, the plane coincides with the cell corners, for oxygen and Al with the center of the unit cell.

Distortions and buckling

For both films we observe significant displacements of all atoms, as summarized in Table 4.6. We can distinguish between the oxygen atoms O_{Al} and O_{La} in the AlO_2-planes and the LaO plane and the respective buckling Δ_{AlO_2} and Δ_{LaO} in these layers. The results are shown in Figure 4.22.

For the 2 ML thick film we detect an outwards movement of the La atoms by 0.079 Å while the O_{La} shows a −0.048 Å downwards shift giving rise to Δ_{LaO} of 0.127 Å. In the AlO_2-plane the average Al position shifts −0.1 Å and the O_{Al} by −0.225 Å towards the interface giving rise to Δ_{AlO_2} of 0.122 Å.

For the thicker film all positions are shifted towards the interface. Displacements in the AlO_2 plane are more pronounced; Al shows a shift of −0.538 Å, the

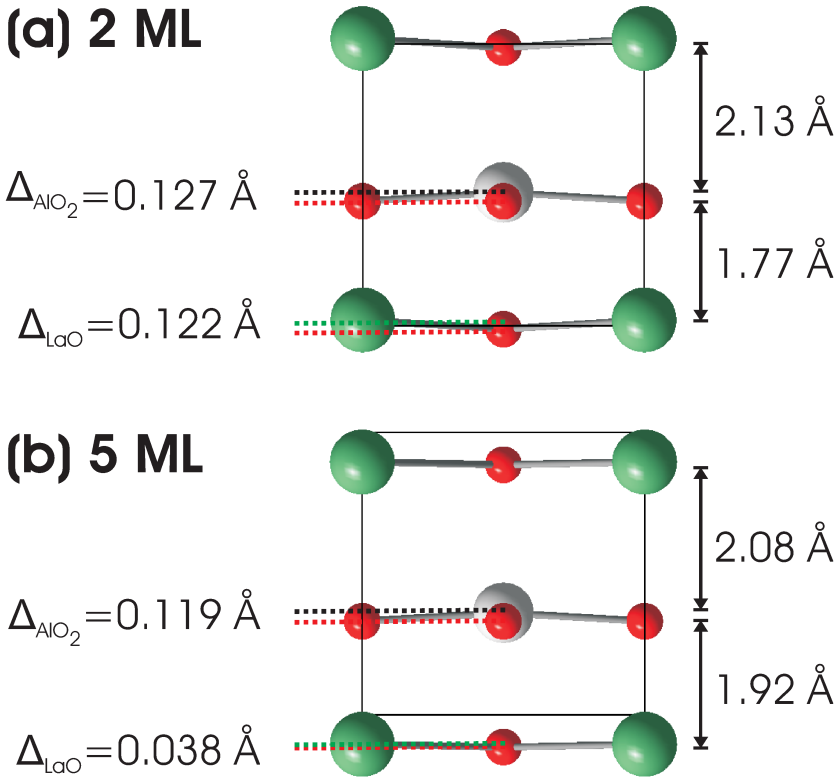

Figure 4.22.: Distortions in the $LaAlO_3$ films in a ball-stick model for (a) the 2 ML and (b) the 5 ML thick film. Positions as extracted from the real space imaging. The buckling Δ_{LaO} and Δ_{AlO_2} are shown as well as the average distance of the AlO_2 and $LaAlO_3$-planes. The black lines indicate the unit cell of the extended $SrTiO_3$ substrate.

O_{Al} of −0.656 Å resulting in Δ_{AlO_2} of 0.119 Å. The La is shifted by −0.405 Å and the O_{La} by −0.194 Å. The average buckling in the LaO plane amounts to 0.04 Å.

The distortions in the $LaAlO_3$ film are expected to reduce the potential build-up due to a reduction of the charge density of the individual layers. Figure 4.23 shows a schematic drawing of the potential build-up in the $LaAlO_3$ film. The effect of buckling is sketched by the blue arrows that show the reduced charge density per layer. The figure on the right shows the resulting reduction in the potential build-up.

The measurements of the positions of the AlO_2 and LaO planes reveal larger relative displacements for the AlO_2-plane. This results in variations in the inter-planar distances. It can be seen from Figure 4.22 that the AlO_2-plane has a shorter distance to the LaO plane on the interface side than to the plane on the surface

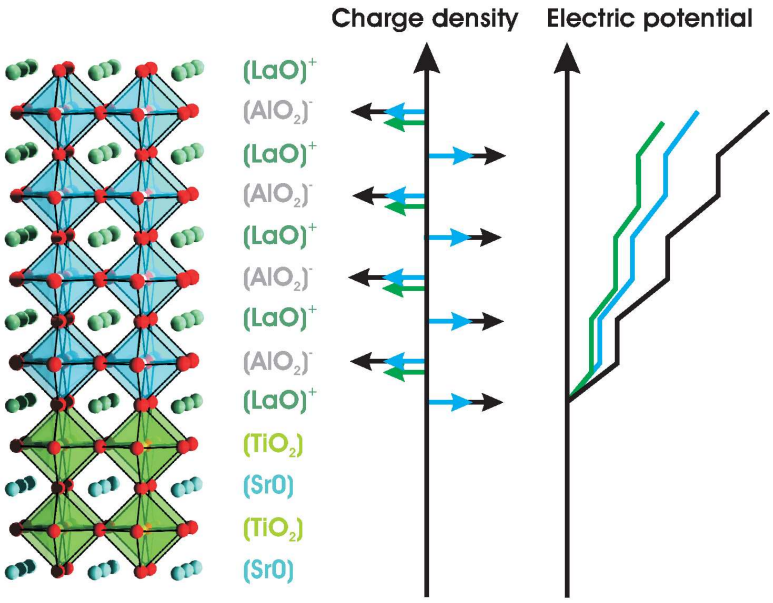

Figure 4.23.: Distortions lead to a reduction of the electrostatic potential build-up in two ways; (i) distortions in the metal oxide planes lead to a reduction of the charge density (blue) (ii) modulation in the distances of the LaO and AlO_2 planes (green lines).

side. Under the assumption that the gradient of the potential is unchanged by this structural modification, the reduced distance will give rise to a smaller overall potential build-up as illustrated in Figure 4.23 by the green lines.

The distortions are most certainly an expression of the polar nature of $LaAlO_3$ and the resulting potential. Interestingly though, in our measurements we did not see any effect of core-level peak broadening or peak shifts as a function of film thickness, indicating a full compensation of the electrostatic potential. Thus, for the thicker film a larger displacement would be expected, which was not observed. This indicates that a partial compensation has been facilitated by the distortions and, for the thicker film, there is another compensation mechanism involved. This observation agrees qualitatively with the SXRD results presented by Pauli *et al.*[69]

Variation of unit cell volume

The average of the positions extracted for all atoms in the 2 ML thick film are about 0.07 Å below the $SrTiO_3$ positions. This corresponds to a $LaAlO_3$ **c** lattice

Table 4.6.: Average cation positions as measured in the real space images obtained by direct transformation. Δz is the displacement from the positions in the extended $SrTiO_3$ lattice.

	2 ML		**5 ML**	
	z	Δ z (Å)	z	Δ z (Å)
Al	0.4736	−0.103	0.3623	−0.538
O_{Al}	0.4423	−0.225	0.3319	−0.656
Δ_{AlO_2}	0.0313	0.122	0.0304	0.1187
La	1.0202	+0.079	0.8963	−0.405
O_{La}	0.9877	0.048	0.8866	−0.443
Δ_{LaO}	0.0325	0.1269	0.0097	0.038
OH	···	···	0.7883	−0.827

constant $\mathbf{c}_{LaAlO_3}$ of 3.83 Å. This value is only slightly larger than the $LaAlO_3$ bulk lattice constant of 3.821 Å. Structural characterization confirmed the perfect in-plane strained growth of the films and hence $\mathbf{a}_{LaAlO_3} = \mathbf{b}_{LaAlO_3} = \mathbf{a}_{SrTiO_3}$. The data indicate an increase of the $LaAlO_3$ unit cell volume. This is counter intuitive since one would expect a decrease in $\mathbf{c}_{LaAlO_3}$ to keep the unit cell volume close to the bulk values.

In the 5 ML film, the average atomic downwards displacement is ~ 0.51 Å. Assuming a linear increase of the atomic displacement as a function of distance from the interface and an equal occupation of all sites, we estimate a downwards shift of 0.2 Å/ML, which translates to an out-of-plane mismatch of 5 % or a $\mathbf{c}_{LaAlO_3}$ of 3.7 Å. The $LaAlO_3$ **c** lattice constant for the 5 ML thick film is hence contracted. This estimate agrees very well with SXRD measurements of a 12 ML thick $LaAlO_3$ film. From the average position of the $LaAlO_3$ ($hk3$) peak at $\ell = 3.144$ a mismatch of 4.7 % or a $\mathbf{c}_{LaAlO_3}$ of 3.73 Å was estimated. This contraction leads to volume conservation as a response to the in-plane tensile strain.

Contribution to the O $1s$ signal by adsorbed OH-groups

As previously mentioned the O $1s$ spectra contain an additional component on the high binding energy (E_B) side due to surface-bound OH-groups. Where possible, the two contributions were separated by a two component fit. The 2 ML thick film showed only a small side component, especially for measurements at high photon energies and large take-off angles, and it was not possible to obtain a complete

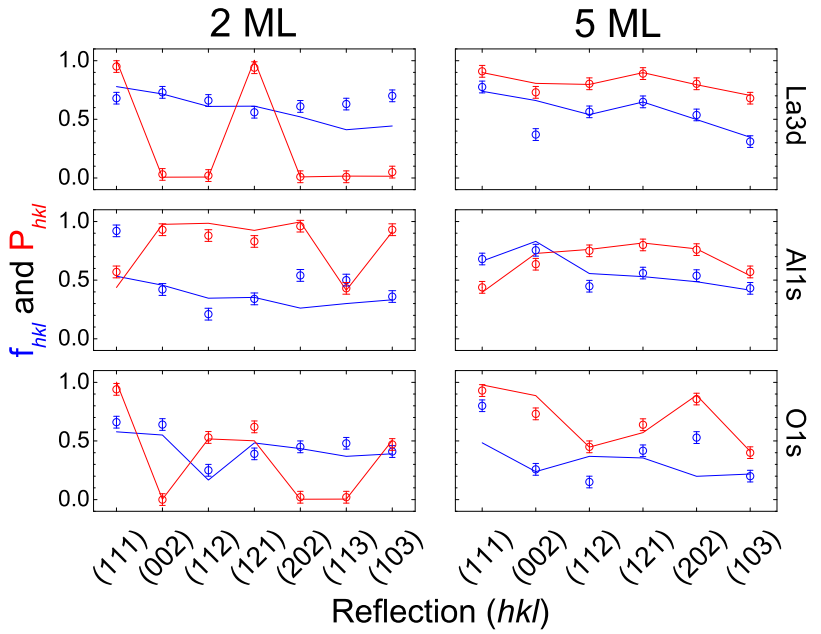

Figure 4.24.: Overview of the XSW data sets. The open symbols show the experimental data and lines represent the best fit to P_H (red) and f_H(blue) in the model refinement.

data set. For the 5 ML film the modulated photoelectron yield for the oxygen was analyzed separately for the 2 components. The resulting yield curves and the best fits are shown in Figure 4.19. Cuts through the real space images of oxygen along the faces of the $SrTiO_3$ unit cell in Figure 4.21 show some weight at the position (0, 0, 0.79) in reference to $SrTiO_3$. This position cannot be due to oxygen in the sublattice of a perovskite film and further support OH-groups.

Ideally, the $LaAlO_3$ surface is AlO_2 terminated. In the refinement step presented below, we identify the Al position in the top layer to be at $z \sim 0.25$. This indicates that the oxygen of the OH-group is sitting about 2 Å above the AlO_2-plane and has 4 nearest Al neighbors.

Images calculated from the "substrate-corrected" Fourier components for the 5 ML film, show intensity at the position identified for OH, although the hydroxyl contribution was removed. In the real space images for the 2 ML film, a relatively high intensity is identified around (0, 0, 0.87) although no clear side components were identified. Hence, the peak fit with two Voigt functions is not adequate to describe the situation. The OH-groups do not simply contribute a single peak with a clearly defined E_B.

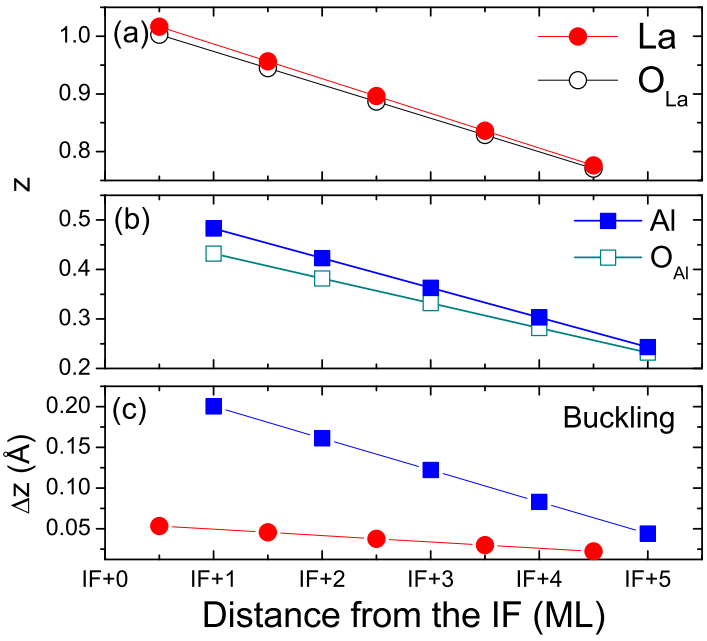

Figure 4.25.: Vertical positions normalized by the $SrTiO_3$ lattice parameter for (a) La atoms and (b) Al atoms of the 5 ML thick film as obtained from the model refinement. (c) The buckling of the cation–oxygen planes. The x-axis represents the distance from the TiO_2/LaO interface in monolayers.

4.4.4. XSW model refinement

This section presents the results obtained by a model refinement using the experimentally measured Fourier coefficients. This analysis step allows individual cation sites and artifacts introduced in the images due to missing Fourier components to be identified. XSW probes the entire thickness of the film and as a result information is averaged and individual cation sites cannot be readily extracted. In order to derive a structural model, a model refinement was performed (Eq. 2.35). The contribution from the atomic sites at different depths was estimated from Eq. 2.36. In the refinement, only the z-position in the unit cell was varied. For the 5 ML films, free parameters were reduced by coupling the atomic positions in a linear way depending on the distance from the interface. The displacements in the different layers can be coupled in other ways (e.g. exponential, quadratic, or cubic), however, no significantly better agreement was found.

Structural model

The best fits to the measured f_H and P_H values are plotted in Figure 4.24, which shows very good agreement between the model calculations and the experimental data. The derived structural data are shown in Figure 4.25. The top two panels show the position for the cations La and Al and the respective oxygen atoms, relative to the extended $SrTiO_3$ lattice. The lower panel shows the buckling Δz calculated from the difference between the cation and oxygen positions. Positive values of the buckling indicate a relative movement of the oxygen atoms towards the interface.

The atomic positions are distributed around the average positions extracted from the direct images and show an increase of the displacement with increasing distance from the interface. The Al atoms show a stronger spread in position. The refinement indicates a decrease in the buckling with increasing distance from the interface.

The positions obtained in this refinement process can be tested against SXRD data from the same sample. CTRs were simulated using the structure obtained from the model refinement. A roughness factor in the β-model[34] of 0.25 was assumed. The comparison is shown exemplary for the (2 1 ℓ) CTR in Figure 4.26 for the 5 ML sample. The comparison shows a good agreement and the number and position of the interference fringes are correctly reproduced. The interference fringes in the simulated CTR are more pronounced. This may be explained by thickness variations in the real samples that were not accounted for in the XSW-derived model, since the XSW results are relatively insensitive to surface roughness, in contrast to the SXRD data.

Removal of artifacts

Real space images obtained by Fourier inversion may contain artifacts. These artifacts arise from the finite number of Fourier components in the calculation. Especially, at high symmetry points in the structure additional intensity is found. A priori, it cannot be identified whether this intensity is real and corresponds to the position of an atom or not. Nevertheless, we can clearly identify artifacts after the refinement step. Figure 4.27 shows for the 5 ML thick film the atomic density of La along the cell edge $(00z)$ with red circles and along the center of the cell at $(\frac{1}{2}\frac{1}{2}z)$ with black squares. As expected, high intensity is observed in the corners of the unit cell, corresponding to the La-site. In addition a weaker peak, close to the body centered position, is observed. The continuous lines show the density calculated from the model found in the refinement. There is a nearly

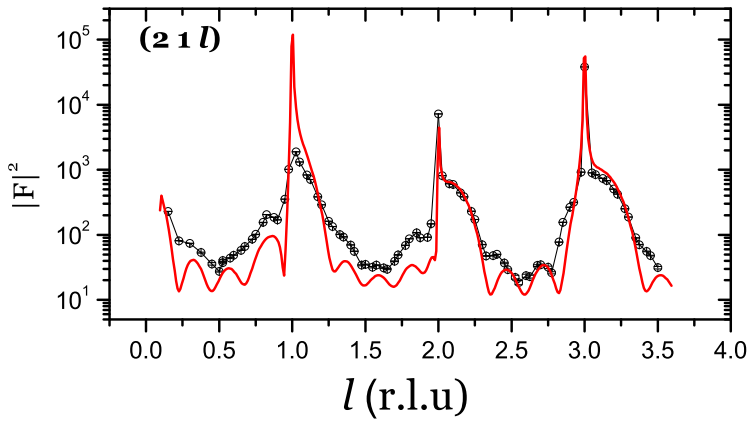

Figure 4.26.: Simulated (21ℓ) CTR for a 5 ML $LaAlO_3$ film using the positions obtained from the XSW model refinement (red line) compared to SXRD data acquired from the same sample.

perfect agreement between the model and the measured data. The peak found at $\frac{1}{2}\frac{1}{2}0.4$ is nicely reproduced by the model containing no La atoms along $\frac{1}{2}\frac{1}{2}z$. The additional intensity is caused by missing Fourier components and does not contain any useful structural information.

4.4.5. Conclusion

Direct images show significant distortions in thin films of $LaAlO_3$ grown on $SrTiO_3$(001). The distortions are more pronounced in samples below the critical thickness for conductivity. Furthermore, we found evidence for a volume expansion of thin $LaAlO_3$ films. Additionally, indications of lattice distortions in the metal oxide planes of $LaGaO_3$ were presented.

The combination of the lattice distortion and larger displacements towards the interface of the AlO_2 planes reduce the potential build-up in the $LaAlO_3$ overlayer.

Analysis of the O 1s core level spectra allowed us to separate the O 1s main line originating from the lattice ($SrTiO_3$ and $LaAlO_3$) and the a peak attributed to OH-groups at the surface. By means of XSWs, the adsorption site of OH-groups was identified above the Al-site. It was not possible to separate the oxygen signal from the $LaAlO_3$ film and the adsorbed OH-groups completely.

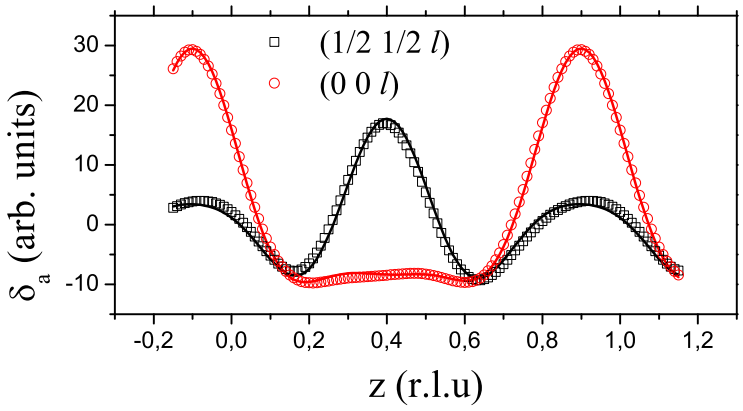

Figure 4.27.: La atomic density densities ρ_a along a unit cell edge in $00z$ (red circles) and along $\frac{1}{2}\frac{1}{2}z$ (black squares) as measured and simulated (line) for the 5 ML thick film.

In a subsequent refinement step the individual atomic positions of all of the atoms in the film were identified. The structural model was consistent with the SXRD data.

4.5. Site-specific spectroscopy of the 2DEG

The gap states of (2%) Nb:$SrTiO_3$, $SrTiO_{3-\delta}$ and n-type $LaAlO_3/SrTiO_3$ interfaces were studied by HAXPES in combination with XSW. In all three cases, photoelectron yield was observed homogeneously in the whole band gap. By employing X-ray standing wave excitation it was possible to separate the partial yields from the Ti and Sr/O lattice sites. For Nb:$SrTiO_3$ the spectral yield originates preferentially from the Ti site. For $SrTiO_{3-\delta}$ the yield is not site-specific except for an in-gap state, ascribed to oxygen vacancy clustering, which is associated with the Ti site. For the $LaAlO_3/SrTiO_3$ sample additional Ti associated yield is observed at the Fermi level, indicating the filling of the Ti d-band.

This section presents the site-specific deconvolution of gap states in $SrTiO_3$. In the first part the experimental details are outlined. The second part presents the data measured from the three samples and, in the following, the results of the deconvolution procedure are discussed. Finally, a number of conclusions are drawn from these measurements.

The material presented in this section is largely based on a paper which has been submitted for publication in Physical Review Letters.

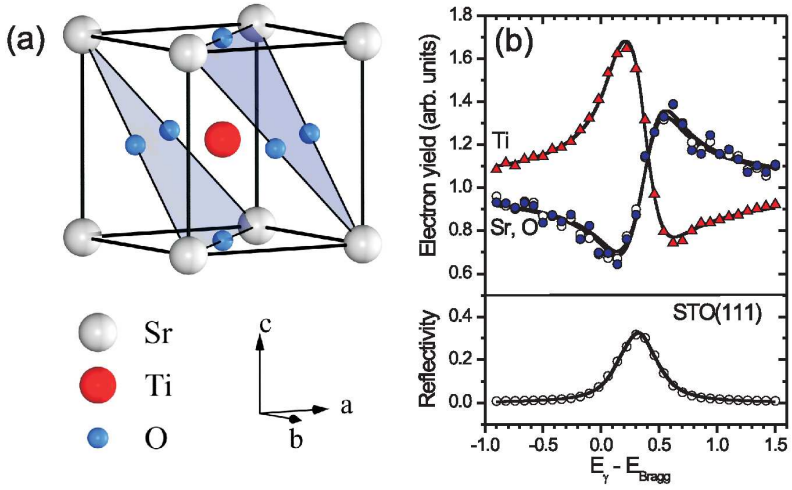

Figure 4.28.: XSW photoexcitation of a $SrTiO_3$ crystal. (a) Sketch of the cubic perovskite $SrTiO_3$ (STO) unit cell with the (111) lattice planes (b) An XSW energy scan employing the (111) reflection (energy scale is in eV). Upper panel: Ti $2p$, Sr $3d$ and O $1s$ photoelectron yield. Lower panel: $SrTiO_3$ reflectivity curve. The excitation energy is E_γ and E_{Bragg} corresponds to the Bragg energy (2.75 keV). At $E_\gamma - E_{Bragg} = 0.2$ eV the XSW maxima are on the Ti site and Ti $2p$ emission is maximal. At $E_\gamma - E_{Bragg} = 0.6$eV the XSW maxima are on the Sr,O sites and the Sr $3d$ and O $1s$ emission is maximal.

4.5.1. Experimental details

For the measurements the Si(111) double crystal monochromator was slightly detuned to reduce higher energy harmonics. In this way the photoelectron yield above the Fermi edge was reduced to a few counts per second. Any photoemission signal above E_F can only be due to high-energy photons arising from an inadequate suppression of higher harmonic radiation in the beamline. Further detuning of the monochromator crystals would have led to a loss in intensity. The remaining radiation only contributes a constant background over the scan area because no core levels excited by photons from the 3rd harmonic (8.25 keV) fall in the gap region. In addition, a contribution to the standing wave effect by the $SrTiO_3$(333) back reflection can be excluded because the reflection would be significantly sharper. Consequently, the background signal could be subtracted before the spectral decomposition. Measurements of the Ag Fermi level gave an overall energy resolution of ~350 meV.

We employed the XSW produced by the $SrTiO_3(111)$ reflection since in the [111] direction the Ti atoms and the Sr,O atoms occupy different planes (Fig. 4.28(a)). In this way the maxima of the XSW can be positioned such that photoelectrons are excited from either the Ti or the Sr,O sites. This is demonstrated in Figure 4.28(b) which shows the photoelectron yield from the strontium, titanium, and oxygen core levels of $SrTiO_3$ with XSW excitation.

4.5.2. Site-specific yield close to the Fermi edge

Spectra measured close to the Fermi level for $SrTiO_{3-\delta}$ and Nb:$SrTiO_3$ are shown in Figure 4.29. The XSW maxima were tuned to the Ti-site of the $SrTiO_3$ structure. For both samples, photoelectrons originating from states within the whole $SrTiO_3$ band gap region are observed. The spectra for Nb:$SrTiO_3$ and $SrTiO_{3-\delta}$ are qualitatively similar. For the $SrTiO_{3-\delta}$ sample an in-gap state is clearly visible $\approx 1.3\,\mathrm{eV}$ below the Fermi edge. The experimental data were fitted (see Fig. 4.29) with a exponential decay function to account for the slope of the valence band, a Fermi edge function (step function convolved with a Gaussian) and, in the case of the O-deficient samples, a Gaussian function to account for the in-gap state. The experimental width of the Fermi edge is comparable to the energy resolution for both samples.

In the following the site-specific contributions to the spectral yield are obtained by a deconvolution procedure.

4.5.3. Deconvolution of gap states

With the help of Eq. 2.32 the spectra can be deconvolved as described in detail in Section 2.6.2. This procedure allows the site-specific partial yields corresponding to the Ti and Sr,O sites to be retrieved. The partial yields are proportional to the partial DOS (p-DOS). However, the site-specific partial yield cannot be directly translated into p-DOS values because the site-specific cross sections are unknown. However, conclusions can be drawn from comparing results for the different samples. Furthermore, XSW measurements of the $SrTiO_3$ valence band by Thiess *et al.*[9] allow estimating that on converting photoelectron yield to p-DOS the Ti $3d$ to O $2p$ ratio increases by a factor of about 1.5.

Figure 4.30 shows the XSW HAXPES results for the two doped samples for which we recorded three spectra each (Fig. 4.30(a) and 4.30(b)): One without XSW effect (open circles), one with the maxima on the Ti planes (blues squares) and one with the XSW maxima on the Sr,O planes (red triangles). The lines show

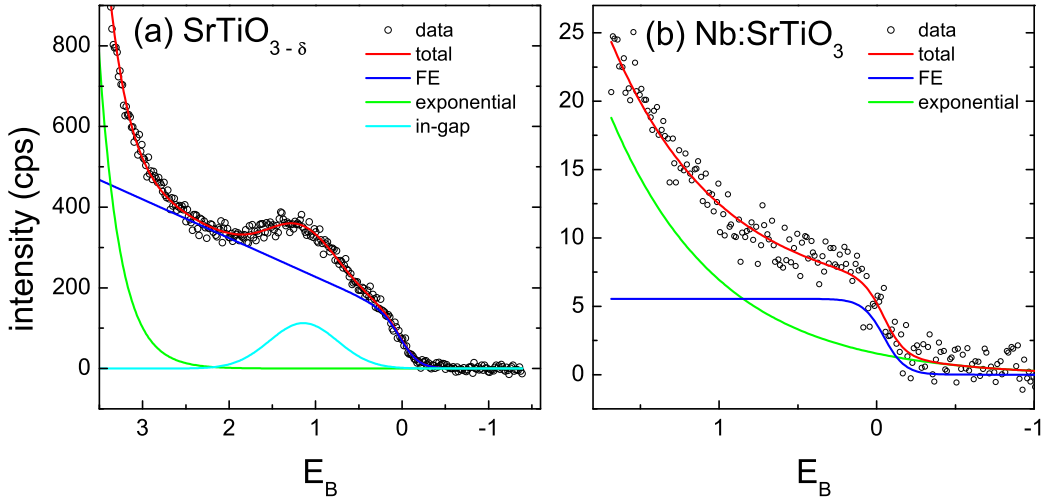

Figure 4.29.: Photoelectron spectra measured close to E_F with the XSW maxima tuned to the Ti-sites. A Fermi function and an exponential decay function were fitted to the data. For the $SrTiO_{3-\delta}$ sample a Gaussian function was used to fit the in-gap state. The best fit curve is drawn in red.

the result of the fits as described above. The insets show a close-up of the −0.4 eV to +0.4 eV binding energy region.

The results of the deconvolution are presented in Figure 4.30(c) and Figure 4.30(d) for the Nb:$SrTiO_3$ and the $SrTiO_{3-\delta}$ samples.

$SrTiO_3$ doped with Nb

In the case of Nb:$SrTiO_3$, the yield in the band gap reacts to the position of the XSW within the $SrTiO_3$ unit cell and the spectra look remarkably different depending on whether the XSW maxima coincide with the Ti or the Sr,O planes.

For the Nb:$SrTiO_3$ sample, the deconvolved spectra in Figure 4.30(c) reveal that, close to E_F, the emission of the shallow carriers originates mostly from the Ti/Nb site. The finding that the DOS near E_F is derived mostly from Ti/Nb agrees well with the resonant XPS study of PLD grown Nb:$SrTiO_3$ by Ishida *et al.*,[103] where the states at the Fermi level were found to have predominantly a Ti 3*d* character. The states appear to be mainly delocalized, with some preference for the Ti site in the $SrTiO_3$ unit cell.

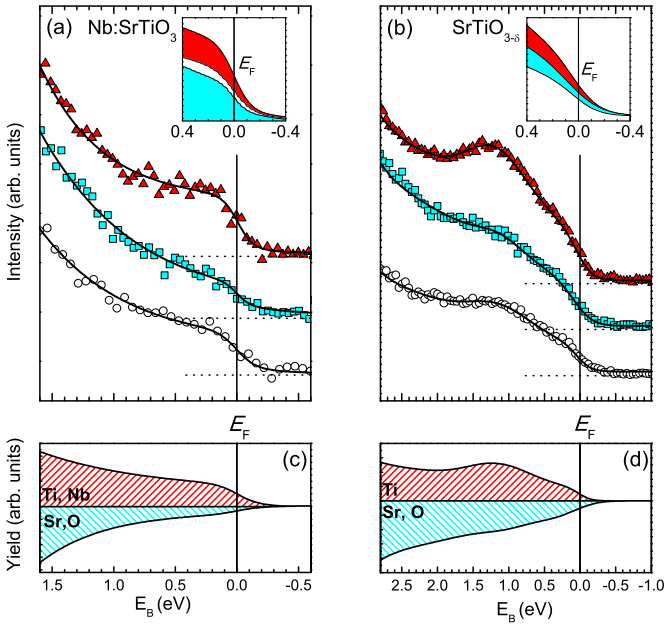

Figure 4.30.: Photoelectron spectra close to E_F under XSW excitation for the Nb:$SrTiO_3$ (a,c) and the $SrTiO_{3-\delta}$ (b,d) samples. Upper panels (a,b) background subtracted raw spectra (symbols) and fitted curves for XSW maxima at the Ti sites (red/dark grey) and Sr,O sites (blue/light grey) and without XSW excitation (white). The spectra are vertically shifted for clarity. Insets in (a) and (b) show a zoom close to E_F. The lower panels (c and d) show the yield decomposed in the contributions from the Ti (red/dark grey) and Sr,O sites (blue/light grey).

$SrTiO_3$ doped by oxygen vacancies

For the $SrTiO_{3-\delta}$ sample the DOS over the same E_B range shows a pronounced effect on the in-gap state (Fig. 4.30(b)). The modulation close to E_F is much less pronounced than in the Nb:$SrTiO_3$ case.

Looking at the deconvolved partial yields, it can be seen that there is a significantly larger contribution from the O/Sr site than in the Nb:$SrTiO_3$ sample. Figure 4.30(d) shows clearly that the in-gap state is mostly localized at the Ti sites. However, the analysis also suggests that the $SrTiO_{3-\delta}$ sample has a significant contribution from O $2p$ states in the conduction band below E_F, much greater than predicted by calculations.[97,116]

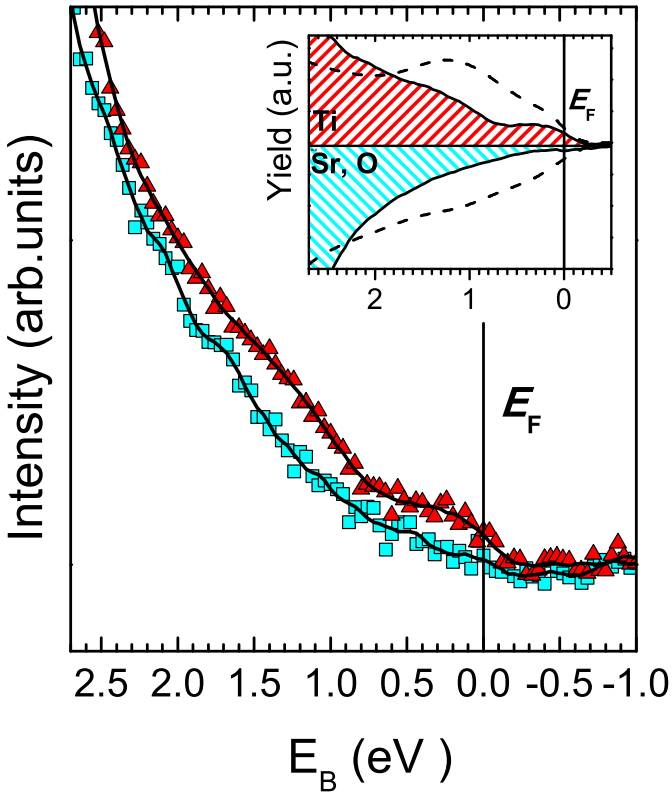

Figure 4.31.: HAXPES spectra close to the Fermi level under XSW excitation for a 5 ML thick $LaAlO_3$ film on $SrTiO_3$. Red triangles, XSW maxima at the Ti sites; blue squares, maxima at the Sr,O sites. The inset shows deconvolved partial yields. The dashed line is the curve from the $SrTiO_{3-\delta}$ sample shown in Figure 4.30(d).

$LaAlO_3/SrTiO_3$ heterointerface

Figure 4.31 shows HAXPES spectra recorded with the XSW maxima tuned to the Ti site and the SrO_3 plane for a $LaAlO_3/SrTiO_3$ interface. The photoelectron yield shows a strong response to the XSW. As it is the case for the doped $SrTiO_3$ substrates, density of states is found in the band gap up to the E_F, giving direct proof of charge carriers at the interface. In particular, when the XSW maxima are at the Ti site, the Fermi edge can be clearly identified and a weak in-gap state at $E_B \approx 1.3\,eV$ becomes visible. The site-specific yields obtained by deconvolution are shown in the inset of Figure 4.31 and exhibit similarities to those of both the $SrTiO_{3-\delta}$ and the Nb:$SrTiO_3$ samples.

It is evident from Figure 4.31 that the substantial density of states at the Fermi level is associated mainly with the Ti site. This is a clear indication of partially filled Ti $3d$ states crossing the Fermi level and is in agreement with an intrinsic electronic reconstruction scenario, such as field doping. In such a case, the electrons at the bottom of the conduction band are expected to occupy the t_{2g} orbitals, predominantly the $3d_{xy}$ state.[62,68,117] The strong Ti $3d$ character near E_F resembles the Nb:$SrTiO_3$ case (cf. Fig. 4.30(c)).

On the other hand, the weak in-gap state detected at $E_B \approx 1.3$ eV resembles in terms of binding energy and site-specificity the in-gap state of the $SrTiO_{3-\delta}$ sample suggesting the presence of oxygen vacancies at the $LaAlO_3/SrTiO_3$ interface.

4.5.4. Conclusions

The carrier density observed for the $LaAlO_3/SrTiO_3$ sample has two contributions. A large fraction appears to result from intrinsic electron doping from the polar $LaAlO_3$ layer, whereas the remaining part originates from oxygen vacancies, all occurring within a 2 nm (5uc) interfacial region in the $SrTiO_3$. Cation intermixing at the interface was found to be insignificant,[57] allowing us to rule it out as a major contributor to the carrier density near E_F. As to the effects of the detected oxygen vacancies in the $SrTiO_3$, the donated electrons occupying the in-gap state at 1.3 eV are expected to be trapped and do not contribute to the conductivity.[102] Furthermore, close to E_F the yield and thus the DOS of the $LaAlO_3/SrTiO_3$ interface (Fig. 4.31 inset) exhibits much less O/Sr character than for the $SrTiO_{3-\delta}$ case (Fig. 4.30(d)). Thus, we are inclined to argue that in the $LaAlO_3/SrTiO_3$ sample the oxygen vacancies in the $SrTiO_3$ do not play a dominant role in the overall carrier density of the 2DEG.

Nevertheless, the vacancies must be stabilized by the particular properties of the $LaAlO_3/SrTiO_3$ system, in agreement with the idea of a charge compensation mechanism,[60] since oxygen vacancies are not stable in $SrTiO_3$ under the chosen growth conditions.[71] Oxygen vacancies created by field effects have also been reported in the context of the development of novel MIM devices.[84] The oxygen uptake by the $LaAlO_3$ overlayer was suggested due to the conductive interfaces of $SrTiO_3$ with amorphous $LaAlO_3$.[85] With increasing vacancy concentration the electrons are trapped at the in-gap states and no longer contribute to the conductivity.[102] This sets a natural limit to the conductivity achievable while maintaining the same 2DEG thickness.

In summary, by combining HAXPES and XSW we obtained site-specific photoelectron spectra near the Fermi level from the bulk of electron-doped $SrTiO_3$ crystals and from the $LaAlO_3/SrTiO_3$ buried interface. We identified the Ti $3d$-

band filling at the $LaAlO_3/SrTiO_3$ interface as predicted by the polar catastrophe but a noticeable carrier concentration seemingly originates from oxygen vacancies in the interface region. This finding suggests that more than one mechanism is at work to compensate the electric field arising from the polar $LaAlO_3$. This explains the absence of significant band bending in the $LaAlO_3$ layer.

4.6. Summary

High quality thin films of the polar oxides $LaAlO_3$ and $LaGaO_3$ were grown on Ti-terminated $SrTiO_3(001)$ surfaces. At the interface a conductive layer is formed as a response to a diverging potential build-up as the polar overlayer thickness is increased. Previous studies showed that this interfacial conductivity is only observed for overlayer thickness above 4 ML of $LaAlO_3$. In the results presented in here, a low binding energy feature was observed in the Ti $2p$ core levels for both types of samples. Its presence indicates a reduction of the Ti valence in agreement with the idea of interfacial doping. Angle-dependent measurements confirm that the feature originates from the interface and furthermore, it was only observed for samples below the critical thickness.

In HAXPES measurements weak signatures of charge carriers filling the band gap up to E_F were observed. Comparison of the site-specific partial photoelectron yield of the interface for oxygen-deficient and Nb-doped $SrTiO_3$ samples showed strong similarities. The pronounced Ti character close to E_F is similar to the Nb:$SrTiO_3$ sample and indicates that the Ti $3d$ states cross E_F giving further evidence for an intrinsic doping scenario. However, a feature resembling the in-gap state observed in the $SrTiO_{3-\delta}$ sample was identified in the interface sample. In Nb:$SrTiO_3$, with a comparable charge carrier density, this in-gap feature was not observed. Hence, it can be interpreted as a unique fingerprint for an oxygen vacancy related density of states. In agreement with the missing Ti $2p$ shoulder, thinner samples, grown under similar conditions did not show any intensity in the band gap within the experimental resolution. The formation of oxygen vacancies as a result of the growth conditions can hence be excluded. Thus, the electron gas consists of two contributions, one fraction results from intrinsic electron doping from the polar $LaAlO_3$ layer, the remaining part originates from oxygen vacancies induced by the polar overlayer, all occurring within a 2 nm (5uc) interfacial region in the $SrTiO_3$.

By means of XSW imaging the polar distortions were imaged for a 2 ML and a 5 ML thick $LaAlO_3$ film. The results show that polar distortions and a modulation of the inter-planar spacing occurs in both samples. Indications for polar distortions were also observed for $LaGaO_3$ films. These distortions are more pronounced for the thinner sample. Distortions were reported as a possible mechanism for suppression of the potential build-up. Thus, the weaker distortions in the thicker sample indicate that the potential build-up is partially compensation by another mechanism. In agreement with the site-specific valence band spectroscopy, one mechanism may be the formation of oxygen vacancies at the interface. There are only a few mechanisms that can explain the critical thickness in combination with vacancy formation. One effect is the creation of vacancies due to a field-effect.

O 1*s* core levels show a hydroxide related high binding energy shoulder on all films. Analysis of the O 1*s* core level spectra permit separating the O 1*s* main line originating from the lattice and the peak attributed to OH-groups on the surface. The high XSW coherent fractions indicate an ordered adsorption mechanism. Using the XSW imaging technique, the adsorption site of OH-groups was identified to be $\sim$2 Å above the Al-site.

Furthermore, it was shown that high quality epitaxial films of the orthorhombic compounds $LaGaO_3$ and $NdGaO_3$ form superstructures on $SrTiO_3(001)$ surfaces. For $LaGaO_3$ films, epitaxy occurs with the pseudo-cubic c-axis out-of-plane resulting in a $(\sqrt{2} \times \sqrt{2})R45^\circ$ superstructure. In $NdGaO_3$ the c-axis can be in-plane oriented in addition, resulting in a (2×1) double domain like superstructure with the a and b axes pointing 45° away from the surface. Moreover, we observed satellite structures around the film Bragg peaks that give indications for a dislocation network to accommodate the in-plane strain.

The $LaGaO_3$ films show several of the characteristic features displayed by $LaAlO_3$. The critical thickness for conductivity and sheet carrier densities are comparable. Both samples exhibited a shoulder in the Ti 2*p* spectra and there is evidence for distortions in the $LaGaO_3$ overlayer. These results support similar mechanisms for the formation of the conductive interface as in the case of $LaAlO_3$.

5. Superlattices of $CaCuO_2$ with $SrTiO_3$

This chapter presents HAXPES measurements on artificial superconducting (SC) superlattices (SLs) based on insulating $CaCuO_2$ and $SrTiO_3$ blocks. The measurements provide evidence that the electrostatic potential build-up that arises due to the polar nature of $CaCuO_2$, is suppressed by oxygen redistribution in the alkaline earth interface planes. Under the measured band alignment conditions a direct charge transfer can be excluded. The proposed interface geometry leads to a zero average electric field in the $CaCuO_2$ block but results in a positive field in the $SrTiO_3$ block. This remaining potential may explain the observed shifts of the $SrTiO_3$ core levels. The oxygen content in the reconstructed interfaces can be increased under strongly oxidizing growth conditions resulting in hole doping of the cuprate block and the appearance of high temperature superconductivity (HTS).

Section 5.1 gives an introduction to the scientific background of complex metal oxide superlattices, in particular the case of $CaCuO_2/SrTiO_3$, and lays out the motivation for this work. Section 5.2 outlines the experimental conditions during the measurements and presents the chosen SC and non-SC SL samples. In the following, Section 5.3, HAXPES results are presented. $SrTiO_3$ core level spectra show a shift to lower binding energy (E_B) in the superlattice samples, which is more pronounced for superconducting samples. The band alignment, estimated from the positions of the core level peaks with respect to the valence band, rules out a direct charge transfer between $CaCuO_2$ and $SrTiO_3$. Metal core levels show additional components due to oxygen redistribution and additional oxygen uptake. The chapter closes with a concluding summary in Section 5.4.

Parts of the data presented in this chapter have been submitted for publication in Physical Review Letters and are currently under review.[10]

5.1. Introduction

Novel metallic, magnetic and superconducting 2D phases[118] can be found at the reconstructed interface between complex TMOs. Particularly interesting is the case of cuprate interfaces where charge redistribution involving CuO_2 planes may give rise to HTS. Standard HTS compounds like YBCO contain planes with Cu in a fourfold planar network known as an infinite layer (IL) structure. The IL blocks are separated by a perovskite-like block which acts as a charge reservoir (CR). When the CR is charge unbalanced by cation substitution or oxygen vacancies, charge carriers (electrons, holes) are exchanged between the two structural units, ultimately, giving rise to superconductivity in the CuO_2 planes.

This general principle can be used as a blueprint for the construction of artificial heterostructure superlattices by means of thin film deposition techniques. Two different compounds are deposited alternately where one may act as the IL and the other as a CR-block. This possibility has stimulated significant research as it may help not only in revealing the origin of HTS but may also yield new HTS systems and with the possibility of fine tuning the superconductive properties. $CaCuO_2$ is a promising candidate for this kind of structures since it has an IL structure where the CuO_2 planes are separated by bare Ca atoms.

Superconductivity has been reported in heterostructures made by a combination of $CaCuO_2$ and $BaCuO_2$ (BCO)[25,26] where BCO acts as the CR-block. The BCO structure is slightly more complex, including extra apical oxygen ions. A maximum T_C as high as 80 K was reported for heterostructures with 3 $CaCuO_2$ layers.[119] Superconductivity with a T_C of about 50 K has also been reported[120] in bilayers of the insulator La_2CuO_4 (LCO) and the metal $La_{1.55}Sr_{0,45}CuO_4$ (LSCO) after exposure to an ozone atmosphere. The superconductivity was found to be confined to a 1 to 2 unit cell thick[121] interface layer. More recently, superconductivity was found in $CaCuO_2/SrTiO_3$[27] and $CaCuO_2/La_{0.65}Sr_{0.35}O_3$ heterostructures.[28] Analogous to LCO/LSCO a T_C of about 40 K was obtained for heterostructures with 3 CuO_2 planes when the superlattices were grown under strongly oxidizing conditions.

The $CaCuO_2/SrTiO_3$ interface shows some similarities to the $LaAlO_3/SrTiO_3$ interface[4] presented in Chapter 4. In the case of $LaAlO_3/SrTiO_3$, a polar discontinuity arises at the non-polar/polar interface giving rise to an electrostatic potential, which diverges with increasing film thickness. Several mechanisms have been proposed for the suppression of this so called “polar catastrophe". The most popular being: Compositional roughening of the interface,[61] electronic reconstruction,[122] elemental interdiffusion[83] and buckling at the interface[69] among others. Hwang *et al.*[122] showed that, depending on the termination of the $SrTiO_3$ substrate, two non-equivalent interfaces are formed, each having a different

suppression mechanism. For TiO_2 terminated $SrTiO_3$ they propose a purely electronic reconstruction which involves the transfer of half an electron per unit cell to the TiO_2 interfacial plane. The resulting interface is conducting. For SrO terminated $SrTiO_3$ a purely atomic reconstruction is proposed, in which half an oxygen atom is removed from the SrO plane per unit cell. In this case the resulting interfaces are insulating.

Figure 5.1(a) shows a truncated structural model of an ideal $CaCuO_2/SrTiO_3$ heterointerface. Along [001] $SrTiO_3$ consist of formally neutral SrO and TiO_2 layers. The $CaCuO_2$ layers are strongly polar, with Ca and CuO_2 layers being alternately charged $\pm 2e$ (where e is the electron charge). In this case, the polar discontinuity is twice as large as for $LaAlO_3/SrTiO_3$ and will result in a rapidly diverging electrostatic potential (see Fig. 5.1(b)). Several examples for the suppression of a built-in potential are reported in the literature based on an atomic rearrangement at the interface, as in the case of the GaAs/Ge interface[123] and the $LaAlO_3/SrTiO_3$ interface.[61,67]

In the present case, a possible mechanism for the suppression of the interfacial electrostatic potential is based on a purely ionic mechanism, involving the redistribution of oxygen atoms between the non-equivalent -CuO_2-Ca/TiO_2-SrO- and -Ca-CuO_2/SrO-TiO_2- interfaces. This is illustrated on the right-hand side of Figure 5.1(c). In the initial report by Di Castro *et al.*[27] the interfacial electronic reconstruction in $CaCuO_2/SrTiO_3$ superlattices was discussed. X-ray absorption measurements at the Cu L-edge confirmed the hole doping of the Cu 3*d* bands. However, the origin of the interfacial charge redistribution was not explained.

In this chapter, HAXPES was used to identify the suppression mechanism of the diverging electrostatic potential. Oxygen redistribution at the interfaces creates multiple components in the core level spectra of the interfacial cations due to variations in the oxygen coordination. Furthermore, band-offsets were determined resulting from the interfacial dipole. This allows the origin of the doping of the CuO_2 planes and, in turn, the superconductivity in $CaCuO_2/SrTiO_3$ SLs to be identified. The results demonstrate that redistribution of interfacial oxygen, induced by the interfacial polarity, plays a fundamental role in the hole doping of the IL block, opening a new route to design superconducting heterostructures.

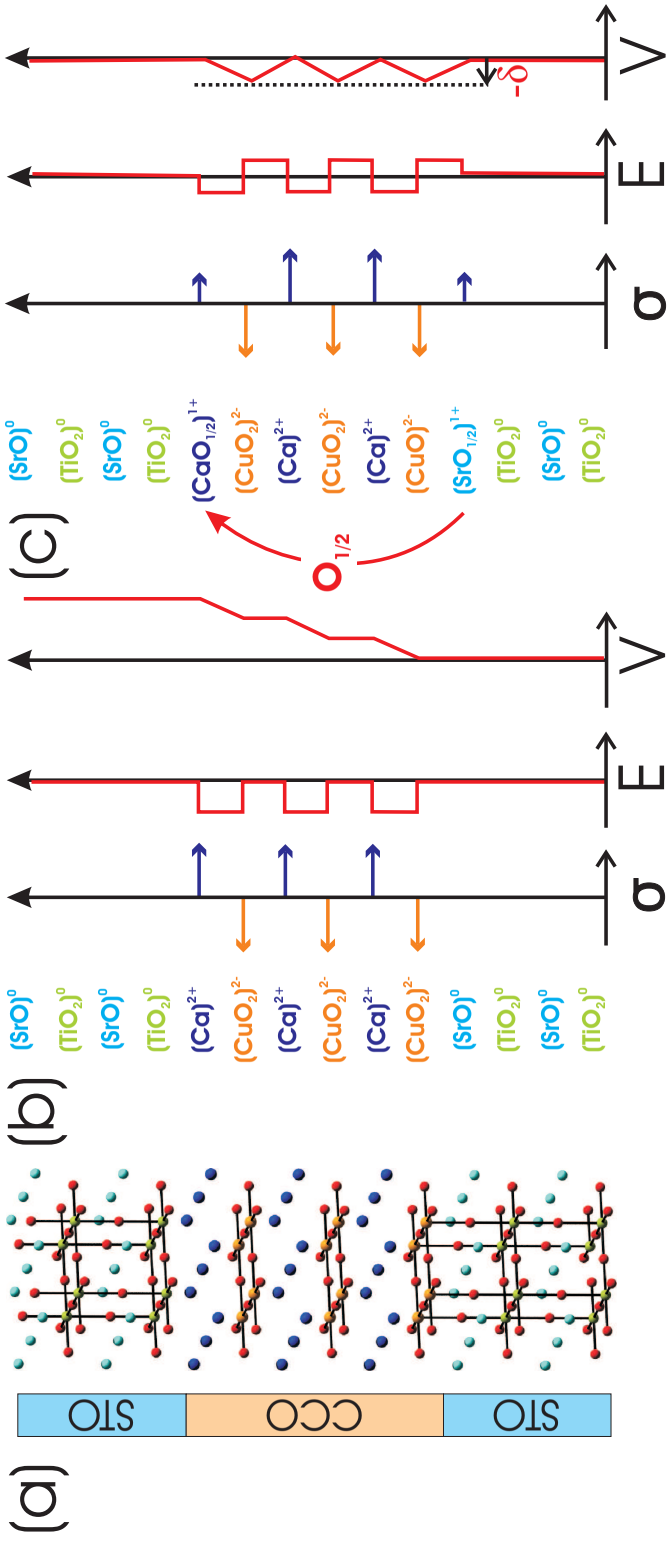

Figure 5.1.: (a) Schematic structure of $CaCuO_2/SrTiO_3$ SLs. Oxygen atoms are shown in red, Sr in light blue, Ti in green, Ca in blue and Cu in orange. The structure is made up of neutral (001) $SrTiO_3$ (STO) planes and $CaCuO_2$ (CCO) planes with alternating net charges (σ). The electric field (E) and the resulting electrostatic potential (V) are shown for (b) the unreconstructed interfaces and (c) the reconstructed interface. For the unreconstructed interface the electrostatic potential diverges with thickness. A suppression of the electrostatic potential can be facilitated by an ionic mechanism involving a redistribution of oxygen. The remaining electrostatic potential does not diverge but its average value is non-zero.

5.2. Experimental details

Following the procedure described by Di Castro *et al.*,[27] $CaCuO_2/SrTiO_3$ SLs made by 3 blocks of $CaCuO_2$ and 2 blocks of $SrTiO_3$ were grown on NdO_2 terminated $NdGaO_3(110)$ substrates by PLD. Two different kinds of SLs were studied: (i) non-SC samples grown in a weakly oxidizing atmosphere (oxygen pressure lower than 0.1 mbar) and (ii) SC samples with zero resistance temperature $T_C \sim 40\,K$ grown in a highly oxidizing atmosphere (oxygen and 12 % ozone at a pressure of about 1 mbar) that were rapidly quenched to room temperature at high oxygen pressure (about 1 bar). As reference, a bare $SrTiO_3$ substrate and a 10 nm thick $CaCuO_2$ film, grown on $NdGaO_3$ under conditions identical to those of the SC SL were measured. To avoid charging problems, the $SrTiO_3$ substrate was rendered slightly oxygen deficient by vacuum annealing.

Room temperature HAXPES measurements were performed at ID32. The electron emission angle was varied from 15 ° to 70 ° to vary the probing depth. Different excitation energies between 2.8 keV and 5.95 keV were used. The overall instrumental resolution was determined by measurements of the Au Fermi level to be better than 400 meV. The best resolution was achieved at 5.895 keV using the Si (333) post-monochromators.

5.3. Hard X-ray photoelectron spectroscopy

This part presents the HAXPES measurements on the SC $CaCuO_2/SrTiO_3$ superlattices. Owing to the polar nature of the $CaCuO_2$ interlayers a diverging electrostatic potential is expected at the interfaces. The measurements provide evidence for the redistribution of oxygen between the two non-equivalent interfaces resulting in a compensation of the electrostatic potential. Furthermore, the uptake of additional oxygen at the interfaces could be verified by the appearance of new core level components on the Ca $2p$, Sr $3d$ and Ti $2p$ core levels and the suppression of the non-local screening channel in the Cu $2p$ core levels.

5.3.1. Core level shifts

In Figure 5.2(a) photoelectron spectra for the energy range from -5 eV to 47 eV are shown for the metallic SC (blue) and an insulating non-SC (red) SL. In addition, spectra from the $CaCuO_2$ reference (black) and a $SrTiO_3$ (STO) substrate (green) are shown for comparison. The spectra from the superlattices contain the spectral

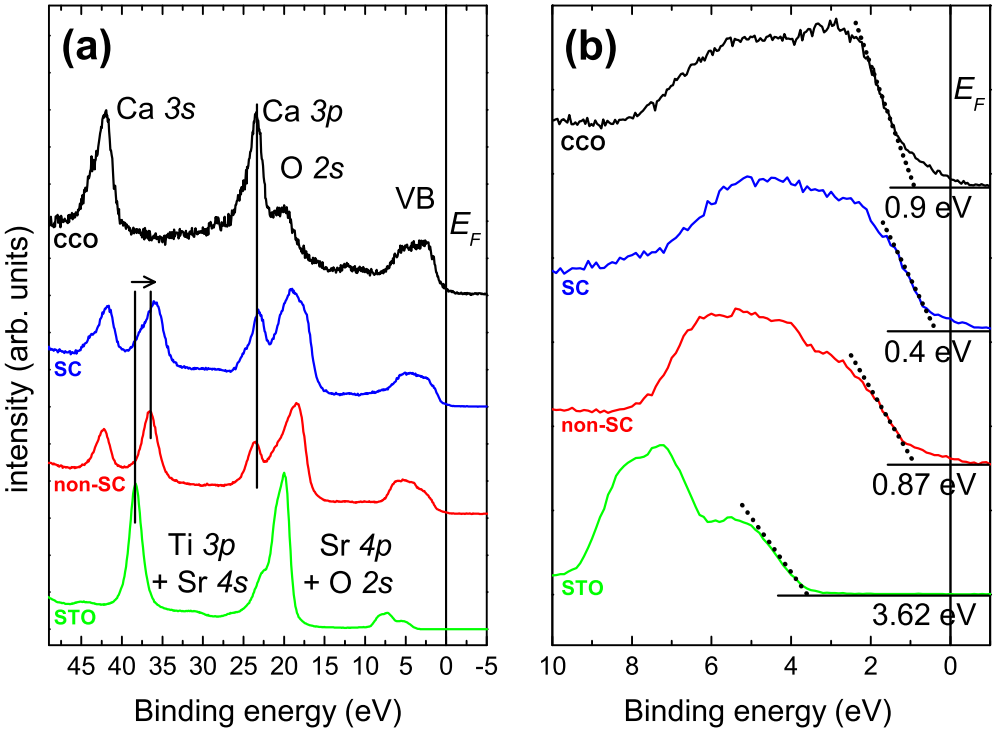

Figure 5.2.: (a) Core level spectra from 47 eV to -5 eV E_B and (b) valence band spectra of the SC SL, the non-SC SL, the $CaCuO_2$ (CCO) film grown in the same conditions as the SC SL and the $SrTiO_3$ (STO) substrate. Measurements were performed at 2.8 keV excitation energy with an emission angle of 70 °.

features of a combination from the pure $CaCuO_2$ (CCO) and the $SrTiO_3$ spectra, as expected. However, for the superlattices, a rigid shift of the Sr and Ti core levels by about 2 eV toward lower E_B is observed, while the positions of the Ca and Cu core levels is almost unchanged.

A possible explanation may be found in the proposed interface geometry. In the $CaCuO_2/SrTiO_3$ superlattice, the two interfaces -CuO_2-Ca/TiO_2-SrO- and -Ca-CuO_2/SrO-TiO_2- (Fig. 5.3 top) are not equivalent. From the cation stoichiometry the stable compounds $CaTiO_3$ and $SrCuO_2$ can form at the interface. At the -CuO_2-Ca/TiO_2-SrO- interface the Ca-plane belongs to the IL structure. However, by including an additional oxygen atom at the interface, $CaTiO_3$ can form, giving the possibility of a Ca-CuO_2-CaO/TiO_2-SrO- interface. Similarly, at the -Ca-CuO_2/SrO-TiO_2- interface the SrO-plane formally belongs to the $SrTiO_3$ block. A stable interface with a reduced oxygen content can be expected since $SrCuO_2$ also exists in the IL structure. Therefore, both the Ca- and Sr-interface planes may accommodate a variable content of oxygen ions: CuO_2-CaO_x-TiO_2

and CuO_2-SrO_y-TiO_2 (Fig. 5.3 bottom). In the case that x=y=0.5 the built-in potential is suppressed (see Fig. 5.1 (c)). However, even though the average electric field is zero and the potential gradient has been eliminated, this geometry produces a positive shift δ in the average potential of the $CaCuO_2$ block. Such a shift can be estimated to be of the order of 1 eV, half of the value of the electrostatic potential increase per unit cell, expected in the case of an unquenched electric field. The direction of the shift is correctly described by this model, however, the measured shift of ∼2 eV is underestimated. The effects of larger shifts in the SC SL are not sucessfully described in this model. Hence, there may be other mechanisms involved.

5.3.2. Band alignment

The band alignment between $CaCuO_2$ and $SrTiO_3$ can be calculated from the data shown in Figure 5.2(a) and the valence band maxima from Figure 5.2(b). A reliable estimate of the valence band offset (VBO) can be obtained by the procedure reported in references.[124,125] The VB maximum (VBM) with respect to the Fermi edge E_F in $SrTiO_3$ and $CaCuO_2$ reference samples is combined with the E_B of Sr 3d, Cu 3s, Ti 3s and Ca 3s core levels, and with their relative positions in the SL samples. The average value of the VBO is 1.4 eV ± 0.3 eV for the SC sample. Since the band gap of $SrTiO_3$ is 3.3 eV[13] and that of $CaCuO_2$ is 1.5 eV, the conduction band offset (CBO) is −0.4 eV (Fig. 5.4). The position of the VBM is obtained by linear extrapolation of the leading edge of the VB spectra shown in Figure 5.2(b). From this we can deduce the alignment conditions as illustrated in Figure 5.4. A direct charge transfer between the CB and VB of $CaCuO_2$ and $SrTiO_3$ can be excluded. Band doping, ultimately giving rise to superconductivity, must have a different origin.

5.3.3. Additional components in the metal core levels

Ti $2p_{3/2}$, Sr 3d and Ca 2p core levels

Figure 5.5 gives an overview of Ti $2p_{3/2}$ and Sr 3d core levels. The spectra contain multiple peaks which were deconvolved using a fitting procedure. The resulting peak positions and peak widths are summarized in Table 5.1.

The Ti $2p_{3/2}$ core levels could be fitted successfully with 2 components. The $SrTiO_3$ reference shows one strong peak centered at 459.5 eV and a weak shoulder at 2 eV lower E_B. The shoulder is related to Ti in a reduced valence state due to

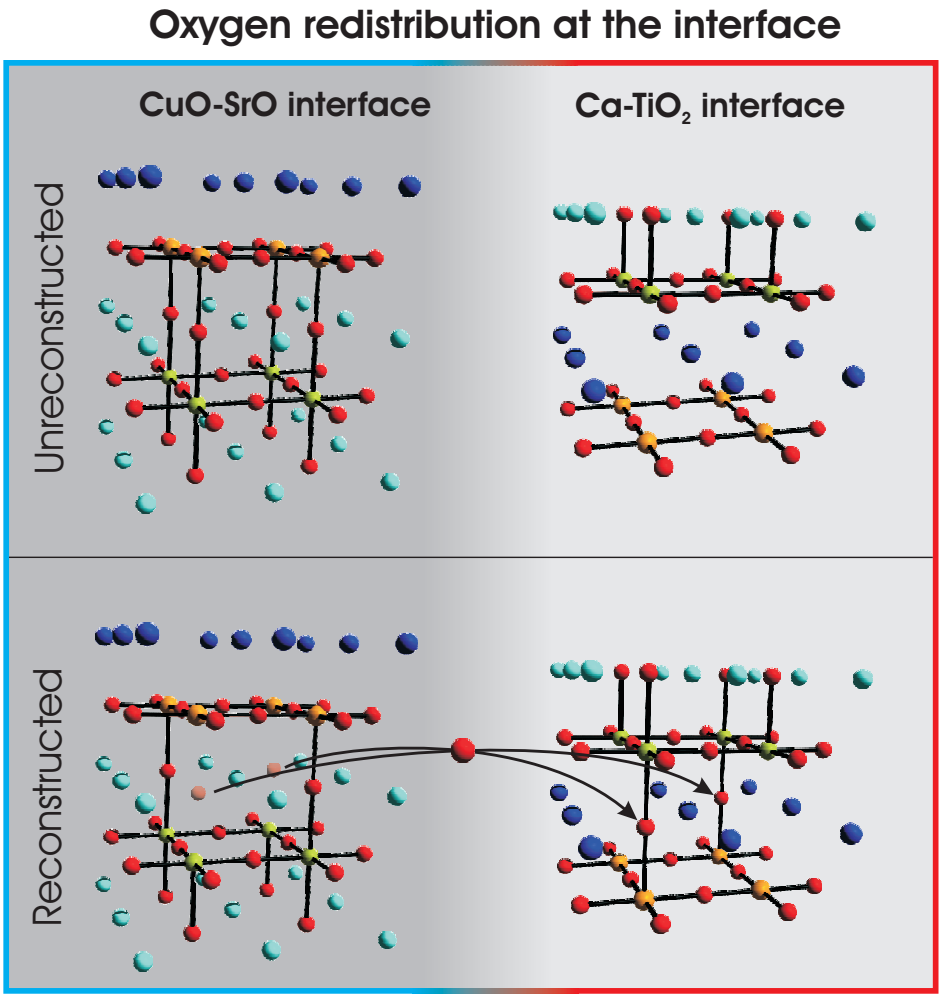

Figure 5.3.: Structural model for the truncated interface as shown in Figure 5.1. without reconstruction (top) and with a possible reconstruction (bottom) involving two oxygen atoms moving from the SrO layer to the Ca plane. This leads to a variable oxygen coordination of the metal atoms at the interface.

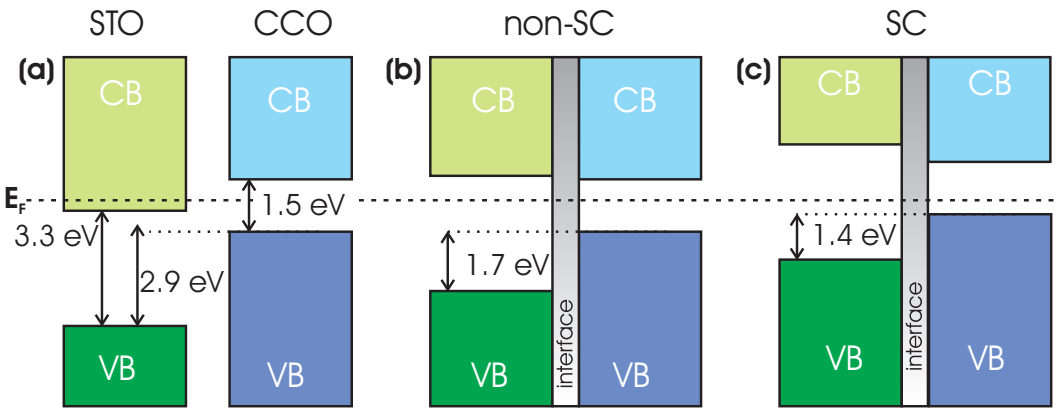

Figure 5.4.: Schematic diagram of the valence band (VB) and conduction band (CB) in (a) the uncoupled $CaCuO_2$ and $SrTiO_3$ reference samples, (b) the non-SC SL and (c) the SC SL samples. A direct charge transfer between the two blocks can be excluded.

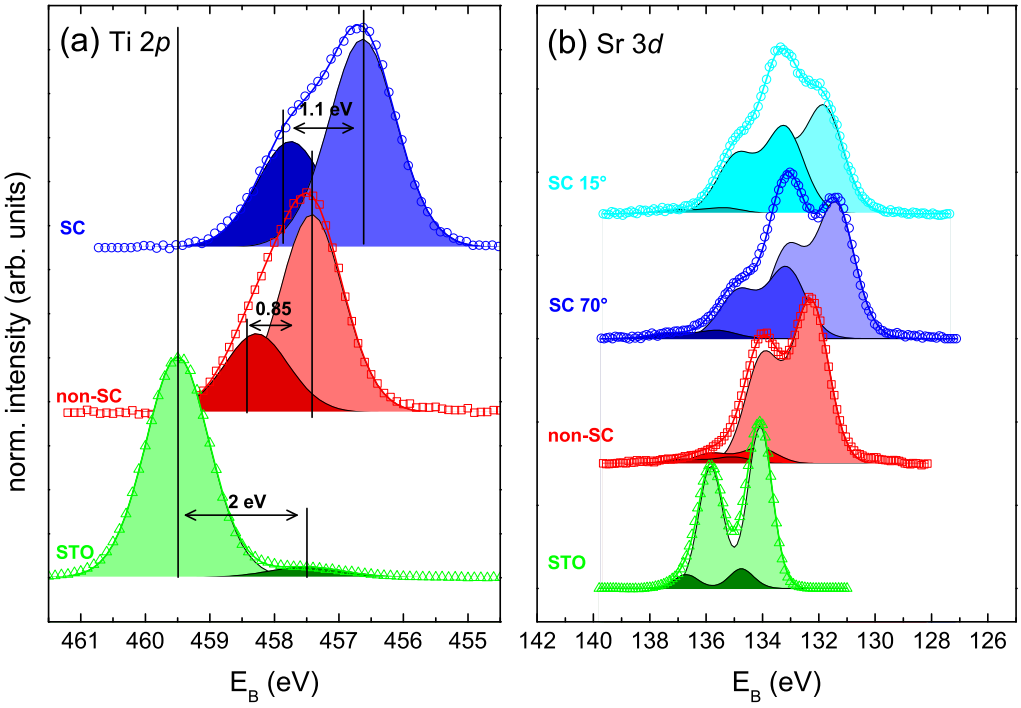

Figure 5.5.: (a) Ti $2p_{3/2}$ and (b) Sr $3d$ core level HAXPES spectra for the $SrTiO_3$ reference sample(bottom, green triangles), non-SC (middle, red squares) and SC (top, blue circles) SLs samples. The shaded areas show the deconvolved components and the thick solid lines the best fit curves. Measurements were performed at 2.8 keV excitation energy and an emission angle of 70 °.

the oxygen vacancies created during vacuum annealing. The superlattice samples show broader photoemission lines that can be deconvolved into 2 components with a splitting of 0.86 eV and 1.12 eV, for the non-SC and SC samples, respectively. The width of the components is 1.17 eV for non-SC and the annealed $SrTiO_3$. For the SC sample the width increases to 1.24 eV.

The Sr 3*d* core level spectra were deconvolved into 3 doublets. For the film samples the spin-orbit splitting was set to 1.7 eV as obtained from the $SrTiO_3$ substrate and the FWHM for all of the components was coupled. For the annealed $SrTiO_3$ sample, the individual components were found to have a width of 1.02 eV which increased to 1.48 eV for the non-SC sample and 1.57 eV for the SC sample. In addition, Sr 3*d* spectra, measured with a more surface sensitive geometry (take-off angle 15°), are shown for comparison. The overall width as well as the width of the individual components shows no significant broadening with respect to the measurements at 70°, while the intensity of the high binding energy components increased.

The Ca 2*p* core levels are composed from three doublets (see Fig. 5.6). In the fitting procedure, the spin-orbit splitting was fixed at 3.5 eV and the intensity ratio to 1:2. In the non-SC sample the components are shifted by 1.1 eV and 2.2 eV, in the SC sample the shift is 1.18 eV and 2.5 eV. The widths of the components are 1.26 eV and 1.38 eV, respectively.

To summarize, all SL spectra are made up from multiple components. The spectra have a strong low E_B component and up to two components at higher E_B, each shifted by about 1–2 eV. The strong low E_B peak shows a shift to lower E_B with respect to the reference sample. For the SC sample, this shift is more pronounced and the high E_B components gain in intensity.

As discussed in the introduction, at an ideal atomically abrupt interface between $CaCuO_2$ and $SrTiO_3$, the polar nature of the $CaCuO_2$ layers results in a strongly diverging electrostatic potential (cf. Fig. 5.1). The huge potential differences in each atomic plane should result in a severe broadening or even distinguishable components in the core level peaks as observed above.

However, as shown for Sr 3*d* in Figure 5.5(b), the peak width was found to be independent of the emission angle. The measurements at shallow emission angle probe mainly the top layers of the SL sample while at 70 ° the probing depth is about 3.6 times larger. The fact that no significant broadening of the core level lines for the larger probing depth was found, clearly shows that the built-in electrostatic potential has been suppressed. The multiple peaks in the core level spectra must therefore be of a different origin.

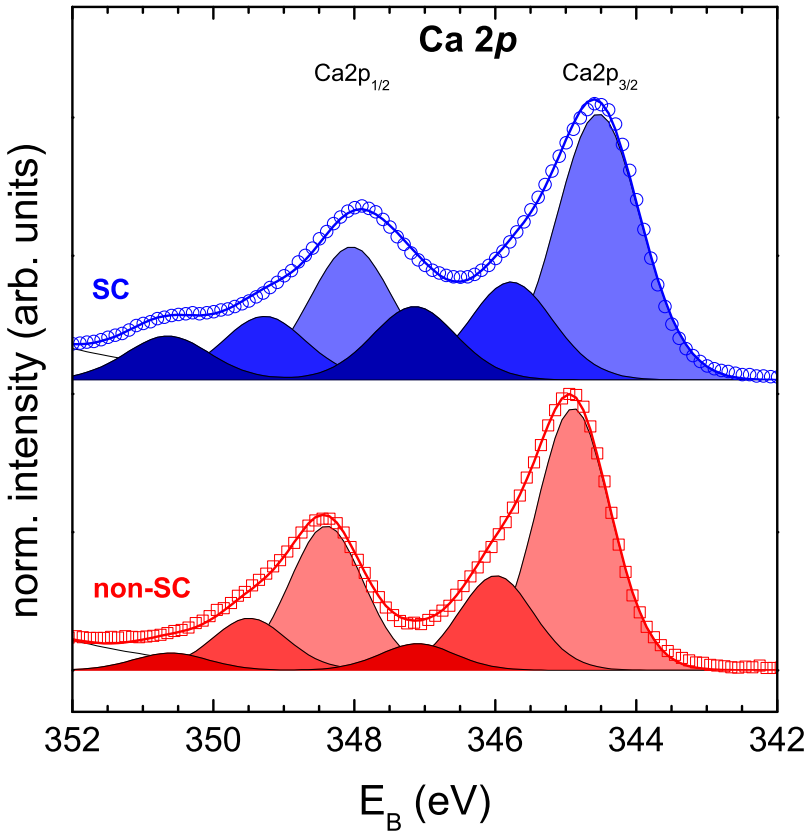

Figure 5.6.: Ca $2p$ core level spectra for (a) the SC sample (top, blue circles) and (b) the non-SC sample (bottom, red squares). The shaded areas show the deconvolved components and the thick solid lines the best fit curves. The high E_B components are more pronounced for the SC sample. Measurements were performed at 2.8 keV excitation energy and an emission angle of 70°

Table 5.1.: Summary of the results from the deconvolution of the Sr 3*d*, Ti 2*p* and Ca 2*p* spectra of the SL samples and the $SrTiO_3$ reference sample. The binding energy and energy widths of all of the components are given. ΔE is the energy shift of the higher E_B component with respect to the main line. For the core levels with a spin-orbit splitting only the position of the stronger component is given.

		SC			
		Component			width (eV)
		1	2	3	
Sr 3*d* 70°	pos (eV)	131.39	133.09	134.85	1.55
	ratio (%)	62.91	33.20	3.88	
	ΔE (eV)	···	1.743	2.47	
Sr 3*d* 15°	pos (eV)	131.78	133.17	135.40	1.60
	ratio (%)	53.55	43.44	3.00	
	ΔE (eV)	···	1.4	2.17	
Ti 2*p*	pos (eV)	458.58	457.4	···	1.24
	ratio (%)	33.76	66.24	···	
	ΔE (eV)	···	1.11	···	
Ca 2*p*	pos (eV)	344.52	345.7	347.02	1.38
	ratio (%)	36.90	14.90	10.74	
	ΔE (eV)	···	1.18	1.32	
		non-SC			
Sr 3*d*	pos (eV)	132.31	133.77	136.57	1.48
	ratio (%)	88.1	9.22	2.67	
	ΔE (eV)	···	1.46	2.8	
Ti 2*p*	pos (eV)	458.33	457.57	···	1.17
	ratio (%)	28.52	71.48	···	
	ΔE (eV)	···	0.86	···	
Ca 2*p*	pos (eV)	344.90	346.00	347.11	1.26
	ratio (%)	68.18	24.64	7.19	
	ΔE (eV)	···	1.10	1.11	
		$SrTiO_3$			
Sr 3*d*	pos (eV)	134.09	134.75	···	1.02
	ratio (%)	89.3	10.66	···	
	ΔE (eV)	···	0.66	···	
Ti 2*p*	pos (eV)	459.5	457.5	···	1.17
	ratio (%)	95.3	4.97	···	
	ΔE (eV)	···	2.0	···	

The significant differences between the non-SC sample and the SC sample indicate that the peak shapes depend strongly on the oxidation conditions during growth. This gives further support for the idea that oxygen redistribution plays a crucial role in creating superconductivity. In the SC sample the relative intensity of the additional high binding energy components are increased due to the enhanced oxidation.

The model of oxygen redistribution, as described above, is supported by the analysis of the Ca and Sr photoemission peaks. In the perovskite structure, the Sr^{+2} ion has a 12-fold cubo-octahedral coordination with oxygen. Similarly, in the ideal infinite layers structure, the Ca^{+2} ions have a 8-fold cubic coordination (the 2 oxygen ions in the Cu plane are missing compared to the perovskite structure). As a consequence, both the Sr $3d$ (in the perovskite structure) and the Ca $2p$ (in the IL structure) core levels give rise to a single well defined doublet in the HAXPES spectra. In the case where no reconstruction occurs in the $(CuCaO_2)_3/(SrTiO_3)_2$ superlattice, the Ca^{+2} and Sr^{+2} ions should maintain the same coordination as in the parent compounds without additional core level peaks. In fact, both the Sr $3d$ core levels (Fig. 5.5) and the Ca $2p$ levels (Fig. 5.6) show several components, possibly due to different Sr/Ca sites having a different oxygen coordination. We attribute such an effect to the presence of non-equivalent Sr^{+2} ions with (12−N) oxygen coordination and Ca ions with (8+N) oxygen coordination at the interfaces, with N ranging from 1 to 4. Similarly, the additional high E_B peak on the Ti $2p_{3/2}$ core level (Fig. 5.5) is observed in both the SC and non-SC SL samples. It can be associated with interfacial Ti sites. In agreement with this idea, the high E_B component of the Ti $2p$ increases in the SC film. This is interpreted as an increase of Ti in octahedral coordination.

The doping mechanism in this scenario is almost straightforward: both of the Ca and Sr-interfaces can accommodate a variable oxygen content x. When x is equal to 0.5 the structure is charge compensated. If during the deposition at very high oxygen/ozone pressure excess oxygen is introduced at the hybrid interfaces charge neutrality is preserved by leaving two holes in the valence band of $CaCuO_2$ for each extra oxygen ion (see Fig. 5.4(c)).

Cu $2p$ screening features

Further evidence of this scenario is given by the Cu $2p$ core level. A representative spectrum, including all peaks and satellite structures, is shown in Figure 5.7. The Cu $2p$ photoemission line shows a pronounced spin-orbit splitting into two components with an asymmetrical peak shape. In addition, each component is accompanied by a shake-up satellite. The following discussion will focus on the Cu $2p_{3/2}$ component.

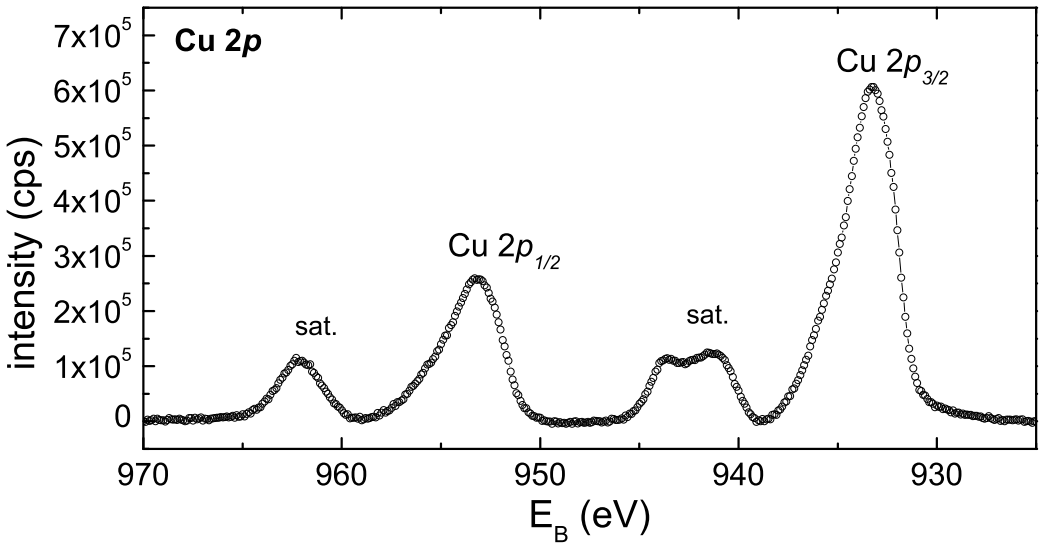

Figure 5.7.: Overview of the complete Cu $2p$ core level spectrum from the SC SL sample. The $2p$ core level has a large spin-orbit splitting between the Cu $2p_{3/2}$ and Cu $2p_{1/2}$ components and each component is accompanied by a pronounced shake-up satellite at higher E_B. The measurements was performed at 2.8 keV excitation energy and an emission angle of 70 °.

Table 5.2.: Binding energies of the components in the Cu $2p$ spectra shown in Figure 5.8.

SC 5.95 keV			
Component	pos (eV)	width (eV)	area (%)
A	932.90	1.41	23.52
B	934.09	1.78	44.18
C	935.66	2.49	32.30
SC 2.8 keV			
A	931.83	1.39	21.70
B	933.99	1.81	47.72
C	935.81	2.5	30.58
non-SC			
A	932.84	1.78	55.10
B	934.01	1.69	23.41
C	935.46	2.27	21.49

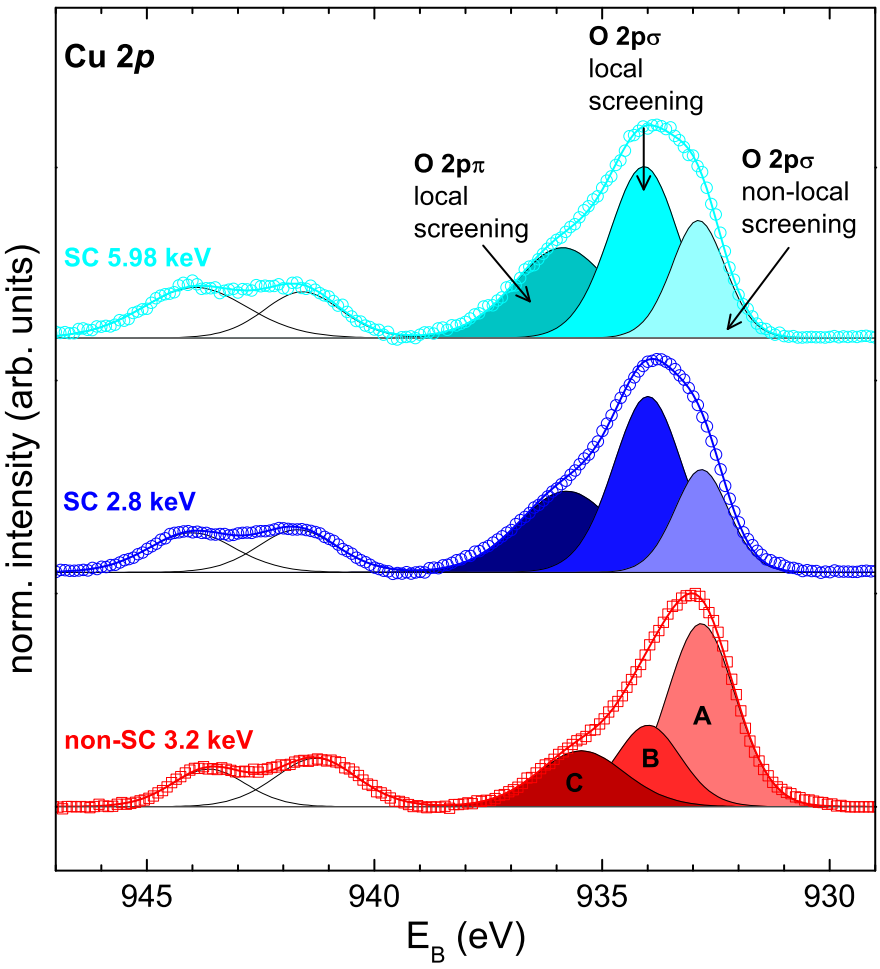

Figure 5.8.: Comparison between the Cu $2p_{3/2}$ spectra of a SC sample at two different excitation energies, 5.98 keV (top, light blue circles) and 2.8 keV (middle, blue circles) and a Cu $2p_{3/2}$ spectrum of a non-SC sample at an intermediate excitation energy, 3.2 keV (bottom, red squares). The shaded areas show the deconvolved components and the thick solid lines the best fit curves.

Figure 5.8 shows the Cu $2p_{3/2}$ spectra of a SC sample, with two different excitation energies (2.8 and 5.95 keV) and a spectrum for the non-SC SL at 3.2 keV. Measurements with an excitation energy of 3.2 keV result in a mean free path $\lambda = 34$ Å , for energies of 2.8 keV $\lambda = 30$ Å and for 5.95 keV excitation the mean free path is $\lambda = 65$ Å. Cu $2p_{3/2}$ spectra from both samples were deconvolved into 3 individual peaks, labeled A, B and C, in the following. The deconvolved components are plotted as shaded curves in Figure 5.8 and the peak positions and widths are summarized in Table 5.2. The most prominent variation is observed in the intensity of the features A and B for the SC and non-SC SL samples. The intensity of feature A drops significantly, from 55.1 % of the total Cu $2p_{3/2}$ intensity in the non-SC SL sample, to 21.7 % in the SC-SL sample. In contrast, the intensity of features B and C increases from 23.4 % and 21.5 % to 47.7 % and 30.6 % for the SC-SL sample. The differences between the measurements at different excitation energies for the SC SL sample are only minor, Features A and C gain slightly in intensity at higher energies.

There is a general consensus that a hole doped in the CuO_2 plane of a IL system moves mainly in the O $2p$ orbitals forming a Zhang-Rice singlet (ZRS). In the photoemission final state, a hole created on the Cu-site in the photoemission process will be pushed from the core hole site, owing to the core hole potential. It can be expected that this hole would also move mainly in the O $2p$ orbitals, leading to a final state with a hole in the O $2p$ core orbital on a Cu site. The positive charge is screened by valence electrons, predominantly from Cu $3d_{x^2-y^2}$ and O $2p_{x,y}$ orbitals.[126] The line shapes are determined by the contribution of these screening processes to the final state. Following the work by van Veenendaal,[43] two features in the Cu $2p$ spectra can be identified (see Fig. 5.8). The core hole site can be screened by: (i) electrons from the oxygen atoms surrounding the core hole site, known as a local screening process, giving rise to feature A or (ii) electrons from the ligand atoms surrounding a neighboring CuO_4 plaquette, leading to feature B, – non-local screening. The latter will give rise to a new ZRS on the neighboring CuO_4 plaquette.

An increase of the local screening at the expense of the non-local screening channel can be observed by comparing the relative intensity of local and non-local screening features (A/B) in the SC sample and the non-SC sample. This result is in agreement with hole doping of the SC sample. ZRS singlets are already present in the hole doped systems and the non-local screening is less effective, because such screening should form a new state with ZRS singlets. As a consequence, the non-local screening is compensated by an increased screening of the core hole by local electrons (local screening).

In the spectra in Figure 5.8 a third component C was identified. A possible explanation is given by the work of Okada and Kotani.[127] In their calculations, they observe a component at higher E_B if out-of-plane orbitals are included in

the local screening. The higher relative weight of feature C in the SC sample can be interpreted, in agreement with these calculations, as an increased oxygen concentration at the interface. The oxygen ions at the interface are apical to the copper atoms.

In agreement with previous reports[128] the spectral weight on the high E_B side (feature C) increased slightly when going to higher excitation energy. However, the overall differences of the spectra measured at different energies are only minor, therefore surface effects on the electronic structure are not relevant at the excitation energies used here.

5.4. Summary

The experimental results obtained by HAXPES allow us to draw several conclusions:

1. The band alignment was measured for the superlattice samples. Although there are significant band shifts there is no possibility for a direct charge transfer between the valence and conduction bands of the two blocks. The charge carriers giving rise to conductivity must have a different origin.

2. The potential build-up expected for an unreconstructed, atomically sharp superlattice is effectively suppressed in both the SC and the non-SC samples. Although the potential build-up is suppressed, the alternating charge of the Ca and CuO_2 layers produces a shift of $\sim$1 eV for the $SrTiO_3$ core levels. This electrostatic potential can partially explain the observed band realignment.

3. The metal core levels (Ca 2p, Sr 3d, and Ti 2p) show additional components. These components give evidence for variations in the oxygen coordination at the interface. The spectral weight of these components is larger in the SC SL sample confirming the uptake of oxygen at the interface.

4. Cu 2p core levels show multiple peaks due to different screening channels. The non-local screening channel is suppressed for the SC SLs due to the presence of Zhang-Rice singlets on the first neighbor CuO_2 plaquette. A high E_B component is observed in all spectra. It can interpreted in terms of screening by out-of-plane O 2p orbitals. Its increase in the SC SL sample give further evidence for oxygen uptake at the interface.

5. The oxygen content in the reconstructed interfaces may be increased under strongly oxidizing growth conditions resulting in hole doping of the cuprate block

and thus in the appearance of HTS. The present study shows that the presence of a strong native polar discontinuity at the interface can be a key ingredient for the synthesis of novel cuprate HTS heterostructures.

6. Electronic properties of oxygen-deficient $La_{0.65}Sr_{0.35}MnO_{3-\delta}$ films

The modification of the electronic structure of $La_{0.65}Sr_{0.35}MnO_{3-\delta}$ samples upon oxygen vacancy creation ($\delta \approx 0, 0.07, 0.12$) was studied by HAXPES experiments at room temperature (300 K) and at low temperatures (86 K). An oxygen deficiency has a pronounced effect on the transport properties, e.g. the conductivity and the metal–insulator transition temperature (T_{MI}) decrease significantly. HAXPES measurements for oxygen-deficient samples show that the Mn 3*d* valence band states shift to higher binding energies (E_B). This results in an overall decrease of the valence band width as a result of the reduced charge carrier density. The well-screened state at the Mn 2*p* core level is present in the as-grown samples but disappears in $La_{0.65}Sr_{0.35}MnO_{3-\delta}$. This indicates a decrease in the hybridization of the Mn 3*d* and the doping-induced states. The lack of a clear band gap formation for oxygen-deficient $La_{0.65}Sr_{0.35}MnO_{3-\delta}$ above T_{MI}, is not compatible with polaron formation but rather with a Mott variable-range hopping mechanism, which is also supported by the transport data. The large electron probing depth of hard X-ray photoelectron spectroscopy is of crucial importance for these investigations because modifications in the electronic structure may occur in the near surface region.

Section 6.1 gives an introduction to the scientific background of the $La_{1-x}Sr_xMnO_3$ system. Experimental details are the subject of Section 6.2. The experimental results are presented in Section 6.3. First, the structural quality of the $La_{0.65}Sr_{0.35}MnO_{3-\delta}$ samples was confirmed by XRD and XRR measurements. Next transport measurements provided indications for a variable-range hopping mechanisms at room temperature. Finally, the HAXPES measurements revealed a decrease in the hybridization of the Mn 3*d* and the doping-induced states at the Fermi level, i.e. stronger carrier localization.

Parts of the work presented in this chapter have been accepted for publication in Physical Review B.[11]

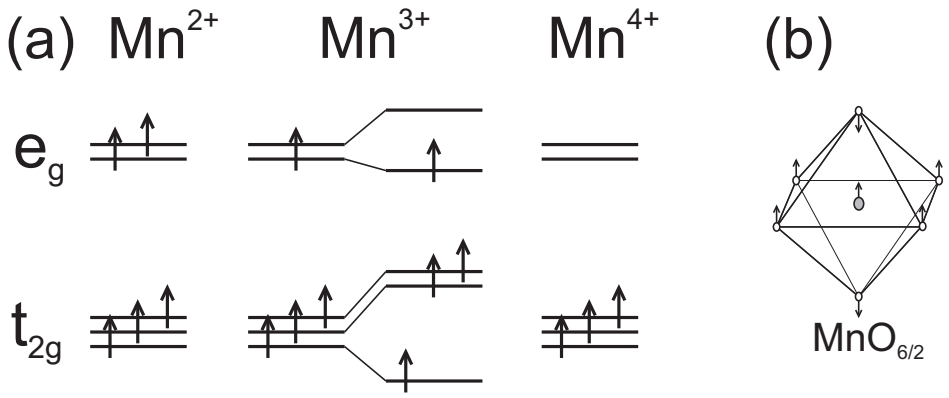

Figure 6.1.: (a) d-shell of the Mn^{2+} Mn^{3+} and Mn^{4+} is split into a low-energy t_{2g} and a high-energy e_g state due to the cubic crystal field. (b) A Jahn-Teller distortion of the $MnO_{6/2}$ octahedra results into a further splitting of the $_{2g}$ and e_g levels in Mn^{3+}. Figure adapted from Refs.[6] and.[5]

6.1. Introduction

The manganite group investigated here can be regarded as a solid solution with the general formula R_{1-x} B_x MnO_3 where R is a trivalent or divalent rare earth (e.g.: La, Nd, Pr, Sm) and B an alkaline earth metal (e.g.: Sr, Ca, Ba, Pb). Research on this group of materials has revealed phenomena such as colossal magnetoresistance,[18,19] tunneling magnetoresistance effect[129,130] and half metallicity.[20] The electronic properties of the manganite system depend sensitively on the doping level x and thus they have a rich phase diagram. Undoped (x=0) end members are antiferromagentic and insulating. However, the doped material shows a T_C and is metallic at low temperatures.

Manganates have the well known perovskite structure with the Mn in octahedral coordination with oxygen. The end members have pure Mn^{3+} or Mn^{4+} with a $3d^4$ and $3d^3$ configuration as shown in Figure 6.1(a). As described in Chapter 2, the structure is distorted due to steric effects and a Jahn-Teller-distortion (Fig. 6.1(b)). Consequently, the $3d$ levels are split into a t_{2g}^3 e_g^1 and t_{2g}^3 e_g^2 states, respectively. The electronic states are shown schematically in Figure 6.1(a) for the different valencies of Mn. When the end compound $LaMnO_3$ is doped with a divalent element such as Sr^{2+}, substituting for La^{3+}, Mn is transformed into a mixed-valence state and holes are introduced in the filled Mn $3d$ orbitals. Also the interatomic distances and angles are modified.

In the $LaMnO_3$-$LaSrO_3$ solid solution the most interesting properties (CMR, half metallicity) appear only in the doping range $0.17 < x > 0.5$.[131] Optimally

doped $La_{1-x}Sr_xMnO_3$ with $x \sim 0.33$ exhibits a spin polarization of 95% and a Curie temperature T_c for the transition between ferromagnetic metal and paramagnetic insulator phases of 370 K.

The coincidence of strong changes in conductivity as well as magnetic properties has attracted scientific interest for decades. The direct exchange (DE) mechanism was formulated in 1951 by Zener[132] and describes this unexpected interplay. The conduction process is thought to be a spin-coupled movement of two electrons. One electron hops from a Mn^{3+} to a neighboring oxygen atom while simultaneously a second electron hops from the oxygen to a neighboring Mn^{4+}. The localized t_{2g} and the itinerant e_g spins show a strong Hund's coupling which favors hopping of electrons with a spin parallel to the localized spin. The hopping of the electrons thus leads to the alignment of the spins and, consequently, to a coupled appearance of electrical conductivity and ferromagnetism.

Thin film samples are of great interest since UHV deposition techniques allow the chemical composition to be tuned precisely. In addition, strain induced by the substrate, can often modify the material properties with respect to the bulk. This can be explained in the DE mechanism since an increase (decrease) of the in-plane Mn-O bond length leads to a reduction (increase) of the hopping term between Mn^{3+}-Mn^{4+} and thereby reduces (increases) T_C.[133] For the manufacture of practical devices this may be of huge importance.

Effects like colossal magneto resistance (CMR),[18,19] found in the last decades, cannot be explained easily in the DE model. In the CMR effect, the resistivity of doped manganites (e.g. $x \sim 0.3$ for $La_{1-x}Ca_xMnO_3$) is reduced by a factor of 1000[134] when a high magnetic field is applied. The CMR effect occurs at relatively high temperatures making manganites potential candidates for devices that operate at room temperature. The high fields ~1 Tesla needed to produce this effect makes them technologically uninteresting for applications in sensors or read heads. However, trilayer junctions and polycrystalline materials, where lower magnetic fields are required to produce the magnetoresistance effect, are used successfully.[129,130] In sandwich structures with two manganite electrodes, separated by a thin insulating $SrTiO_3$ layer, the resistivity changes by more than 1800% depending on the spin alignment between the two layers. If the spins in the two layers are aligned parallel a low resistivity is found. If the spins are aligned anti-parallel the resistivity increases significantly due to scattering by the magnetic domain walls. The spins in one electrode can be flipped by an external field.

The tunneling magnetoresistance effect is exploited in spintronics devices, where the spin as well as the charge of the electrons are used to carry information. The possibility of extracting spin polarized electrons from manganites makes them

strong candidates for technological applications in the context of magnetic field sensing, read heads and spin injection.[21]

Besides their technological importance, doped manganites are attracting a considerable amount of interest from a theoretical point of view. The electronic properties of doped manganites can not be adequately described by the classical one-electron band theory[135] since they show strong electron correlation effects. For instance, lightly doped manganite ($La_{1-x}Sr_xMnO_3$ with $x < 0.1$) has a partially filled 3*d*-band and therefore would be expected to be a good conductor. However, due to correlation effects,[131] such a material is found experimentally to be antiferromagnetic and insulating. Correlation effects can significantly modify the electronic band-structure. For instance, in $LaMnO_3/SrMnO_3$ digital superlattices, the variation of the local charge carrier density, tuned by modifying the number of conducting interfaces, influences the $3z^2$-r^2 electron band width.[136,137] Although the band-width modifications in SC-manganite materials have been theoretically predicted,[138,139] only few experimental techniques are able to provide direct evidence of such profound changes in the electronic structure.

The electronic and magnetic properties of $La_{0.65}Sr_{0.35}MnO_3$ are known to react sensitively to chemical variations, but also to the oxygen content. It was shown experimentally that the oxygen content exhibits strong variations depending on deposition conditions and post deposition treatments which can lead to oxygen defects. The evolution of the charge carrier concentration as a function of oxygen deficiency can be studied by tracking the evolution of the out-of-plane lattice parameters.[140–143]

Here we present a HAXPES study of the electronic properties of SC manganite materials where only the charge carrier density is modified. Physical properties of these materials can be severely effected by extrinsic parameters such as chemical composition,[144,145] oxygen content[146,147] and substrate-induced strain,[148] making it difficult to distinguish between the individual contributions to the band-width modification. Our strategy hence focuses on a set of $La_{0.65}Sr_{0.35}MnO_{3-\delta}$ samples in which only the charge-carrier concentration is varied by slight variations of the oxygen content ($\delta \approx 0, 0.07, 0.12$).[140] The changes we observe in the valence bands of the manganite thin films therefore exclude all of the other extrinsic effects that may influence the physical properties of the samples.

X-ray diffraction confirmed that the films were uniformly strained with respect to the $SrTiO_3$ substrate. The reflections from the films had a constant rocking curve width for all of the samples giving evidence of unaltered crystalline quality. The evolution of the charge carrier concentration as a function of oxygen deficiency can be studied by tracking the evolution of the out-of-plane lattice parameters.[140]

Earlier reports on the effect of oxygen vacancies made use of SXPS and UPS. Picozzi *et al.*[149] published a combined experimental and theoretical study. However, the electronic and magnetic properties of manganites react sensitively to structural modifications[5,6] and contamination (i.e. hydroxyl groups, carbon, etc.) at their surfaces. Due to the high energy of the emitted photoelectrons, HAXPES is particularly well suited for analyzing the bulk electronic modifications of SC manganites as a function of specific parameters such as the charge-carrier density. Additionally, some features like the "well screened" feature of the Mn $2p$ core level are only observable by HAXPES below T_{MI}. This state arises from the response of the Mn $3d$ valence electrons to the creation of a Mn $2p$ core hole[43,44] and it is very sensitive to the level of doping by Sr, and hence represents an additional probe of the conduction electrons. Structural perfection is required for such a many electron response to occur and may be quenched close to the surface, and therefore can only be detected by means of HAXPES.[42,150]

Photoelectron spectra of the Mn $3s$ core levels exhibit exchange splitting which allows conclusions on the Mn valence state to be made.[40,41] The correlation between the Mn $3s$ splitting and the formal Mn valence (ν_{Mn}) has been studied systematically for manganites by X-ray photoelectron spectroscopy.[151,152] Based on the published data one can estimate the ν_{Mn} from the Mn $3s$ splitting. Furthermore, considering formal valencies of $+3$, $+2$ and -2 for La, Sr and O, respectively, allows the condition for charge neutrality to be calculated with $\delta = (x - \nu_{Mn} + 3)/2$.

No significant variations in the Mn $3s$ exchange splitting were found when the Mn valence was modified via the Sr doping concentration. An explanation for this may lie in the localization of the holes in the O $2p$ orbital.[151] The splitting should hence be more sensitive to oxygen defects and increase linearly with the oxygen vacancy concentration. Contrary to this, a soft X-ray study[149] reported an unphysical decrease in the exchange splitting due to the oxygen deficiency. The authors attributed this to surface effects. Reliable data can hence only be obtained from HAXPES measurements.

6.2. Experiment

$La_{0.65}Sr_{0.35}MnO_3$ thin films with a thickness of 40 nm were grown epitaxially on $SrTiO_3$ substrates by MBE[153] by our collaborators at TASC-INFM, Basovizza (Trieste), Italy in an atmosphere of $\sim 2.66 \times 10^{-5}$ mbar of O_2+5% ozone. This allows epitaxial manganite thin films with optimal magnetotransport properties to be grown without the need for post-deposition annealing.[153] Subsequently, vacuum annealing created different amounts of oxygen vacancies. The three samples presented in the following are an as-grown optimally doped sample (LSMO-A),

a slightly underdoped sample (LSMO-B) and a heavily underdoped (LSMO-C) film. The underdoped samples were obtained by a post-annealing treatment at 700 °C for different times (see Table 6.1).

Transport measurements were performed by Pasquale Orgiani and Alice Galdi at CNR-SPIN, Salerno, Italy by the standard four-probe dc technique using the Van-der-Pauw configuration with a pulsed bias and reversed current.[154]

X-ray reflectivity measurements were performed by Pasquale Orgiani using a Philips X'Pert-XRD analytic diffractometer equipped with a four-circle cradle. A Cu Kα_1 (λ = 1.5406 Å) source was used at 40 kV and 40 mA. The measurements confirm that the films are fully strained with respect to the $SrTiO_3$ substrate.[140]

Photoelectron spectra were collected at ID32 at the ESRF at excitation energies of 2.8 keV and 5.95 keV at room temperature and at 84 K. At an electron emission angle of 66 ° the probing depths were 15 nm and 27 nm, respectively. Further surface preparation steps were unnecessary. The instrumental resolution was determined by measurements of the Au E_F to be 200 meV at 5.95 keV and 350 meV at 2.8 keV. Valence band spectra were normalized to the incoming photon flux. Peak positions were extracted by fitting several Voigt functions after a Shirley background subtraction.

6.3. Results and discussion

6.3.1. Structural characterization

X-ray diffraction confirmed that the films were fully strained with respect to the $SrTiO_3$ substrate. The crystalline quality of all samples was confirmed by the constant rocking curve width of the film reflections.

For the samples studied here the out-of-plane lattice parameter were 0.384, 0.387 and 0.388 nm for the samples LSMO-A, LSMO-B and LSMO-C, respectively. The main panel of Figure 6.2 reports XRD data acquired around the specular (002) Bragg reflection of the film in terms of d-spacing. As clearly visible for the as-grown LSMO-A and the annealed LSMO-B samples, the width of the reflection is not affected by annealing. In the case of the sample LSMO-C, a narrower entrance slit (1/8" compared to 1/2") was used in order to increase resolution in the proximity of the substrate diffraction peak, thus explaining the lower intensity of the diffraction peak.

Table 6.1.: Sample preparation conditions.

Sample	Annealing time	T_{MI}
LSMO-A	0 min (as-grown)	> 500 K
LSMO-B	120 min	345 K
LSMO-C	240 min	270 K

The quality of the films is further confirmed by the low-angle X-ray reflectivity (XRR) measurements (inset of Figure 6.2). For as-grown LSMO-A, (black curve) interference fringes are clearly visible up to an angle of 2.5 degrees. Film thickness and surface roughness were analyzed using the Philips X'pert epitaxy package. Surface roughness was estimated to be in the range of a single unit cell of $La_{0.65}Sr_{0.35}MnO_3$, consistent with a pure layer-by-layer growth mode of the manganite films. In order to verify if the post-annealing process affects the surface roughness of our films, a manganite thin film was post-annealed twice for 120 min at 700°C. XRR data are shown in red in Figure 6.2 and show that the surface roughness does not vary substantially after thermal annealing. The root mean square (rms) roughness of ~ 0.7 nm obtained by fits to the data is less than two unit cells of $La_{0.65}Sr_{0.35}MnO_3$.

Additionally, FEG-SEM analysis showed smooth surfaces with no evidence for structural defects for both as-grown and annealed samples, thus confirming the XRR results. Moreover, FEG-SEM probe shows the absence of any foreign particles/grains therefore ruling out the formation of spurious amorphous phases induced by the post-annealing process.

6.3.2. Transport properties

The resistivity (ρ) was measured as a function of temperature for all three samples and the data are presented in Figure 6.3. The data show a low-resistivity regime at low temperatures followed by a strong increase in resistivity. For the oxygen-deficient samples LSMO-B and C the resistivity drops after reaching a maximum at T_{MI}. The resistivity of LSMO-A continues to increase slowly at higher temperatures.

The as-grown film (sample LSMO-A, black circles) shows the lowest resistivity of the three samples. At 20 K a resistivity of 0.06 mΩcm is measured and the maximum resistivity of 3.93 mΩcm is reached at 480 K. In the temperature range from 320 K to 370 K the data show a pronounced increase in resistivity by more than a factor 2. Nevertheless, no metal–insulator transition is observed up to the highest temperature measured.

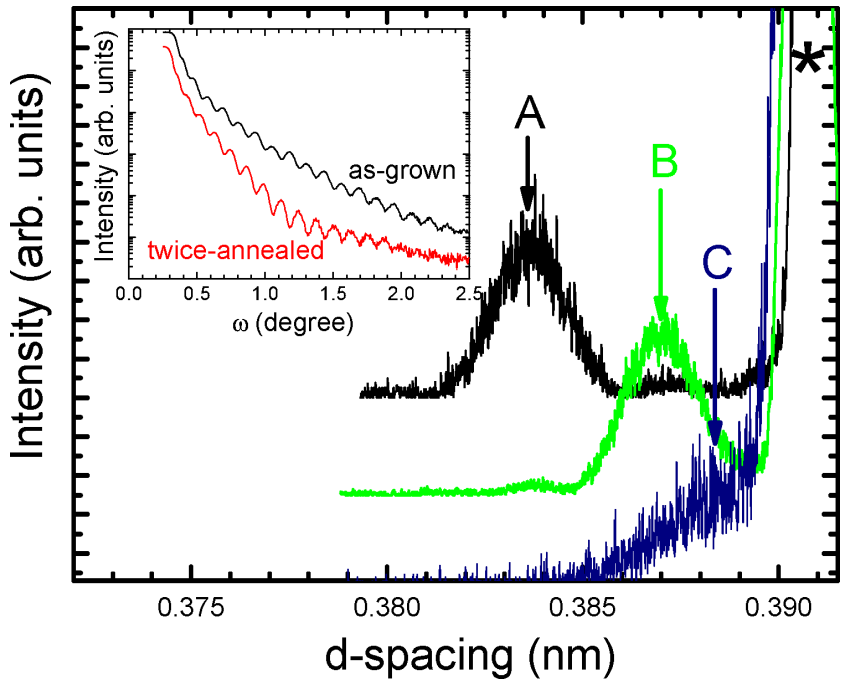

Figure 6.2.: XRD data around the (002)-symmetric Bragg reflection from a series of vacuum annealed $La_{0.65}Sr_{0.35}MnO_{3-\delta}$ films in terms of d-spacing. For higher resolution the entrance slit was closed for sample LSMO-C resulting in lower count rates. The inset shows low-angle reflectivity measurements of an as-grown $La_{0.65}Sr_{0.35}MnO_3$ thin film (black line) together with a $La_{0.65}Sr_{0.35}MnO_{3-\delta}$ thin film after thermal post-annealing cycles (red line). Data were obtained by a laboratory X-ray source — courtesy of P. Orgiani.

Following the annealing in vacuum (i.e. decreased oxygen content), the resistivity of the $La_{0.65}Sr_{0.35}MnO_{3-\delta}$ films increases and the T_{MI} moves to lower temperatures. For sample LSMO-B (green squares), T_{MI} is found at 345 K with a maximum resistivity of 11.21 mΩcm. For sample LSMO-C (red triangles) T_{MI} is found at 270 K with a maximum resistivity of 591.38 mΩcm. The HAXPES measurements were performed at room temperature (RT) and at 86 K. Figure 6.3 shows that at RT LSMO-A and LSMO-B are in a metallic state while LSMO-C is insulating. At 86 K, all samples are metallic but show clear differences i∼n resistivity.

The metallic and insulating behaviors of the ρ(T) curves (black line in the inset of Figure 6.3) were analyzed using the formulas ρ-$\rho_0 \propto T^{\alpha}$ and $\rho \propto \exp(T_0/T)^{\beta}$, respectively. The variables ρ_0, α, T_0 and β were used as free fitting parameters. In single crystals with a predominant electron-electron scattering process at low temperatures[19,131,155,156] a value of 2 is typically observed for α. A value of 2.5 is typically associated with a single-magnon scattering mechanism, as observed in

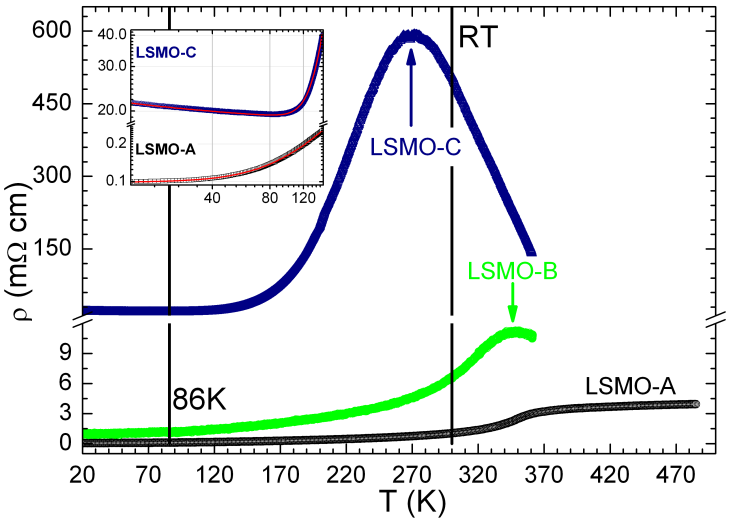

Figure 6.3.: Resistivity curves measured as a function of temperature for the three $La_{0.65}Sr_{0.35}MnO_{3-\delta}$ samples. See Table 6.1 for their different post growth annealing conditions. The two vertical lines at 86 K and 300 K mark the temperatures for the HAXPES measurements. The arrows indicate the metal–insulator transition temperatures. The inset shows the data in a log-log plot and the best fits (see text) of the low-temperature regime for LSMO-A and LSMO-C.

most thin films.[157,158] For the optimally doped LSMO-A sample the resistivity curve scales very well as T^{α} with $\alpha = 2.2$, thus giving a better agreement with an electron-electron scattering process. β provides insight into the basic physical mechanism of the insulating state. Specifically, values of 0.25 and 1 for β are associated with Mott variable-range hopping (VRH)[5,159] and the polaronic thermal activated[160] regime, respectively. As previously observed in low-disordered manganite systems,[161] here the VRH model better fits the experimental data in the proximity of T_{MI} while at higher temperatures (e.g. 400 K) polaron activation provides a better explanation, as there the hopping process may be more limited by the formation of polaronic quasi-particles with larger effective masses.

At low temperatures around 86 K, all of the samples exhibit metallic behaviour, nevertheless the most reduced sample LSMO-C shows a minimum in the resistivity curve (cf. inset of Fig. 6.3). Such a behavior can be interpreted as a localization phenomenon driven by temperature-dependent quantum corrections due to Coulomb interactions. Indeed, as previously reported,[162,163] quantum interference effects influence the transport properties of SC materials, thus determining a reentrant metal-to-insulator transition.

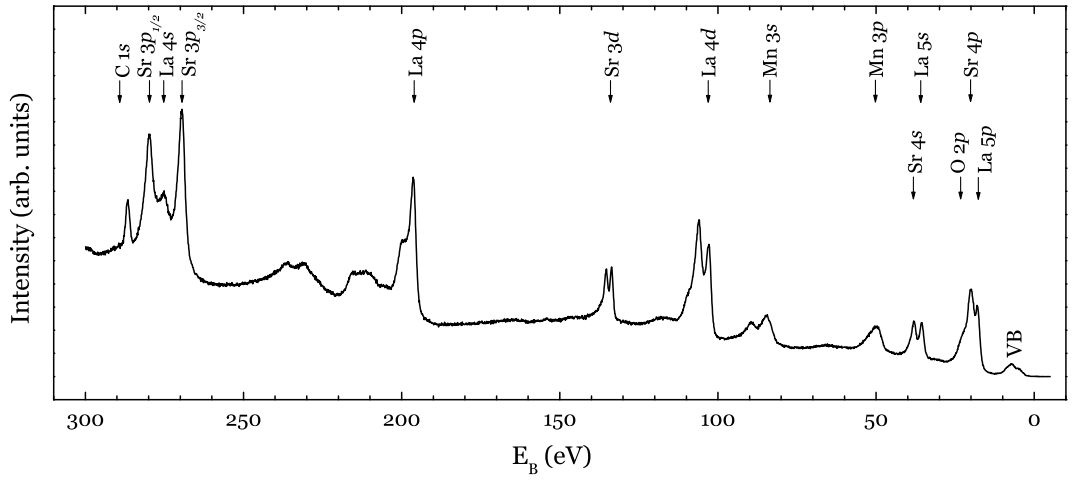

Figure 6.4.: HAXPES survey spectra for the LSMO-A film for the E_B range from 300 eV to -5 eV measured with a photon energy of 5.95 keV.

6.3.3. Photoelectron spectroscopy

A HAXPES survey scan in the E_B range -5 eV to 300 eV is shown in Figure 6.4. The individual core levels are marked by arrows and the corresponding orbitals are indicated. The spectra show all the expected core level lines from the film. The samples are free from contaminations except for a weak carbon contamination that can be detected by the presence of the C 1*s* core level, probably due to exposure to air. The substrate peaks are not visible.

In the following the O 1*s*, Mn 3*s*, Mn 2*p* and the valence band region are presented and discussed in more detail.

Oxygen core levels

Comparison of the core level intensities of Mn 2*p* and O 1*s* should reveal the oxygen deficiency. However, the O 1*s* peak is asymmetrical and shows a clear shoulder (Fig. 6.5). Best agreement was found by fitting with three Voigt functions. The main peak (1) is found at 530.5 eV, the first side component (2) at 531.2 eV and the second side component (3) at 533.5 eV. The ratio of the three components changes with annealing time. Component 3 gains in intensity for the samples LSMO-B and -C. A measurement of LSMO-C at lower energies (more surface sensitive) is represented as a line in Figure 6.5 and shows an increase of component 3. Therefore, this feature can be attributed to OH-groups on the surface. Similar features are well documented for many metal oxide surfaces. Feature 2 may be

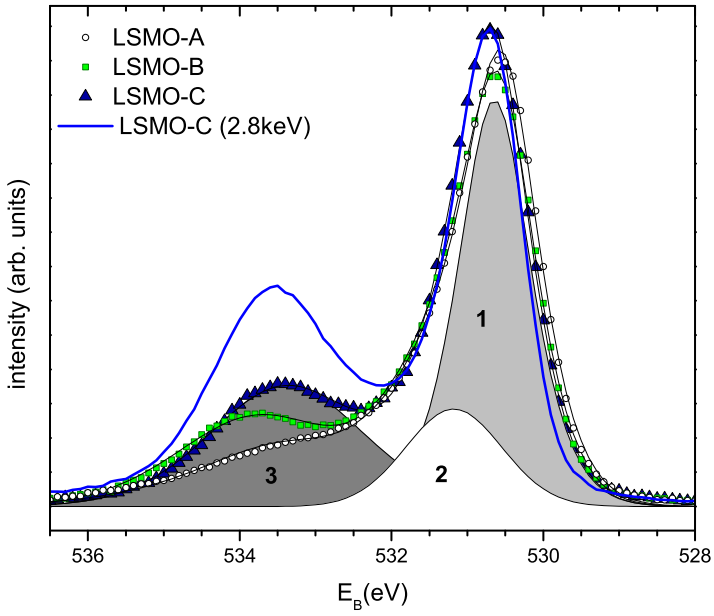

Figure 6.5.: $La_{0.65}Sr_{0.35}MnO_{3-\delta}$ O 1s core level spectra measured at 5.95 keV photon energy. The symbols are the raw data which were fitted with three components. For comparison the blue line shows a spectrum measured at 2.8 keV for LSMO-C.

associate to oxygen in oxygen-deficient parts of the sample, however, no clear dependence on the annealing time was found.

Comparison of the O 1s main component with Mn 2p gave oxygen deficiencies of 8.5 % and 13 % or a δ of 0.25 and 0.39 for the samples LSMO-B and C respectively. These values most probably have a relatively large error bar. Ratios calculated with the total intensity of all oxygen components showed an increased oxygen content with longer annealing time possibly due to stronger OH-adsorption on the annealed surfaces. To reliably determine the oxygen content, we made use of systematic changes in the Mn 3s exchange splitting as a function of the Mn valence.

Mn 3s exchange splitting

As discussed in the introduction, the Mn valence can be derived from the exchange splitting observable in Mn 3s core level spectra. Two representative spectra for the LSMO-A and C samples measured at 5.95 keV are shown in Figure 6.6. The peak positions were extracted by fitting two Voigt functions after background

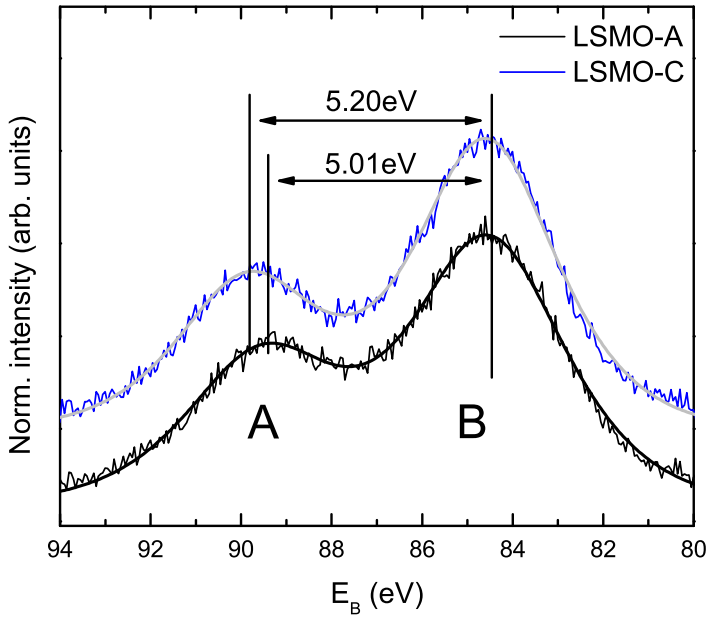

Figure 6.6.: Mn 3*s* core level spectra for the as-grown (LSMO-A, black line, bottom) and most annealed (LSMO-C, blue line, top) in comparison.

Table 6.2.: Results of the Mn 3*s* core level analysis.

sample	Mn 3*s* ΔE		Mn formal valence[1]
	5.95 keV	2.8 keV	ν_{Mn}
LSMO-A	5.01	5.18	3.3
LSMO-B	5.08	5.2	3.2
LSMO-C	5.20	···	3.1

subtraction. The results of the Mn 3*s* analysis are summarized in Table 6.2. The 3*s* spectra show a splitting into two components, where the larger peak is centered around 84 eV and the smaller one at 89.5 eV. For LSMO-A the splitting amounts to 5.01 eV and increases to 5.08 eV and 5.20 eV for LSMO-B and LSMO-C respectively. For measurements at an excitation energy of 2.8 keV the splittings are larger. The ratio of the two components A and B appears to vary with the oxygen content.

The valency ν_{Mn} can be estimated from the splitting. From the values in Table 6.2 the oxygen deficiency δ is estimated to be $\sim$ 0.02, 0.07 and 0.12 for LSMO-A, B and C, respectively. For LSMO-A, the small δ is consistent with the transport measurements which showed the absence of a metal–insulator transition in the resistivity behavior up to at least 480 K and the very low residual resistivity. These values are similar to those obtained for single crystals,[19] suggesting that

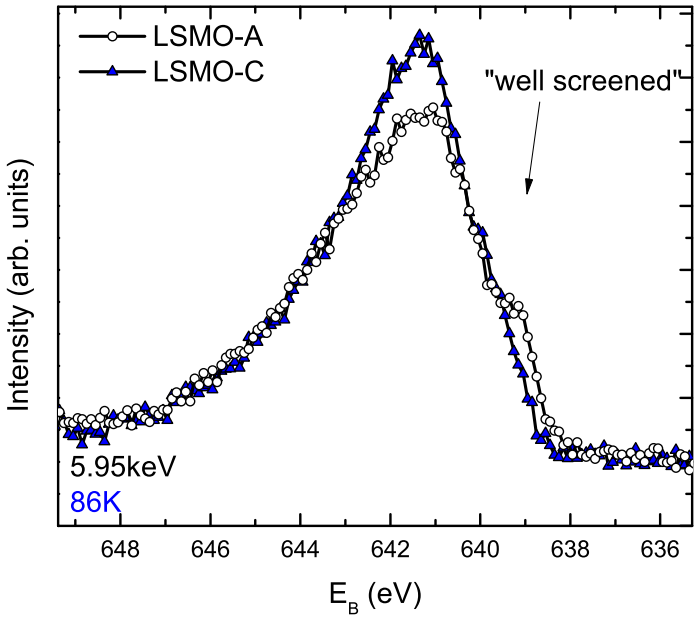

Figure 6.7.: Mn $2p$ core level spectra for the as-grown (LSMO-A, open circles) and most annealed (LSMO-C, blues triangles) samples. The measurements were performed at 86 K and a photon energy of 5.95 keV. The shoulder at 639 eV is not observed for LSMO-C.

LSMO-A should be very close to the optimal doping level of x = 0.35. Urushibara *et al.*[19] reported the electronic phase diagram of single crystals prepared by the floating-zone method. They report a T_c of 283 and 342 K for x = 0.175 and 0.25. The Mn^{4+} contents were determined by redox titration to be 17% and 19% (i.e., $\nu_{Mn} = 3.17$ and 3.19), respectively. Compared to the values for LSMO-B and C in Tables 6.1 and 6.2, T_{MI} appears to correlate quantitatively to ν_{Mn} in a consistent way, regardless of the oxygen vacancy concentration and the sample being a thin film or a bulk crystal.

Mn 2*p* screening state

Mn $2p_{3/2}$ core level spectra measured at 86 K and 5.95 keV for the LSMO-A and C samples are presented in Figure 6.7. The Mn $2p$ main line is found at 641 eV. For LSMO-A the spectra exhibit a low E_B feature, ∼2 eV below the main line (marked by an arrow in Figure 6.7). This feature is significantly more pronounced at higher photon energies and lower sample temperatures.

While the less reduced sample (LSMO-B) still exhibits a shoulder (not shown) which is comparable to that of the as-grown sample, the same feature is completely missing for the most oxygen-depleted sample (LSMO-C). The low E_B feature has been theoretically explained by the screening of the core hole on the Mn site by e_g valence electrons from neighboring atoms.[42–44] In particular, van Veenendaal[43] demonstrated, using an Hamiltonian model with a larger cluster size, that the low E_B feature was related to a non-local screening channel, which decreased with the increase of both the doping-level and the magnetic disorder. A dependence on the orbital ordering was also demonstrated. Using multicluster calculations, Horiba *et al.*[42] identified the screening to originate from a $2p^5 3d^5 \underline{C}$ final state where $\underline{C}$ represented doping-induced states at the E_F and $3d^5\underline{C}$ resulted from a charge transfer from $\underline{C}$ to the Mn $3d$ state. The screening feature was found to increase proportionally with the hybridization between the Mn $3d$ and the $\underline{C}$ states in agreement with the observed strong dependence on the doping level,[42] contrary to the finding by van Veenendaal. More recently, experimental evidence on the temperature dependence of the low E_B feature has been reported[150] to be associated with the ferromagnetic order and/or the metallicity of the $La_{1-x}Sr_xMnO_3$ samples. For the samples presented here, the strength of the low E_B feature correlates strongly with the hole doping level determined by the oxygen vacancy concentration. At 86 K only LSMO-A and B show the well screened feature, although all three samples are in a metallic state. We argue that the LSMO-C sample is on the verge of a metal-to-insulator transition and the weaker hybridization together with increasing electron localization reduce the efficiency of the screening effects.[2]

Valence band

Spectra of the valence band in the binding energy range from 9.5 eV to -1.5 eV are shown in Figure 6.8(a). The valence bands of $La_{0.65}Sr_{0.35}MnO_{3-\delta}$ show several shoulders. The different contributions have been discussed by Picozzi *et al.*[149] in a combined experimental and theoretical study. Accordingly, the strongest contribution at 5.5 eV is identified as the O $2p$ band. The shoulder at 3.5 eV is assigned to the O $2p$-Mn $3d$ hybridized states. The Mn $3d$ states are visible as an additional shoulder at $\sim$2 eV and states close to the Fermi edge and show a splitting into Mn $3d$ t_{2g} and Mn $3d$ e_g orbitals respectively. The t_{2g} states form a well-defined peak which can be interpreted as a core level, while the Mn e_g states are rather dispersed.

The positions of the Mn $3d$ t_{2g} and e_g and the O $2p$-Mn $3d$ hybrid show systematic changes as a function of annealing time, photon energy and tempera-

[2] Furthermore, in agreement with van Veenendaal[43] the magnetic disorder could also play a role in reducing the low E_B feature, as well as the increased orbital ordering expected in a strongly reduced $La_{0.65}Sr_{0.35}MnO_{3-\delta}$ film.[147]

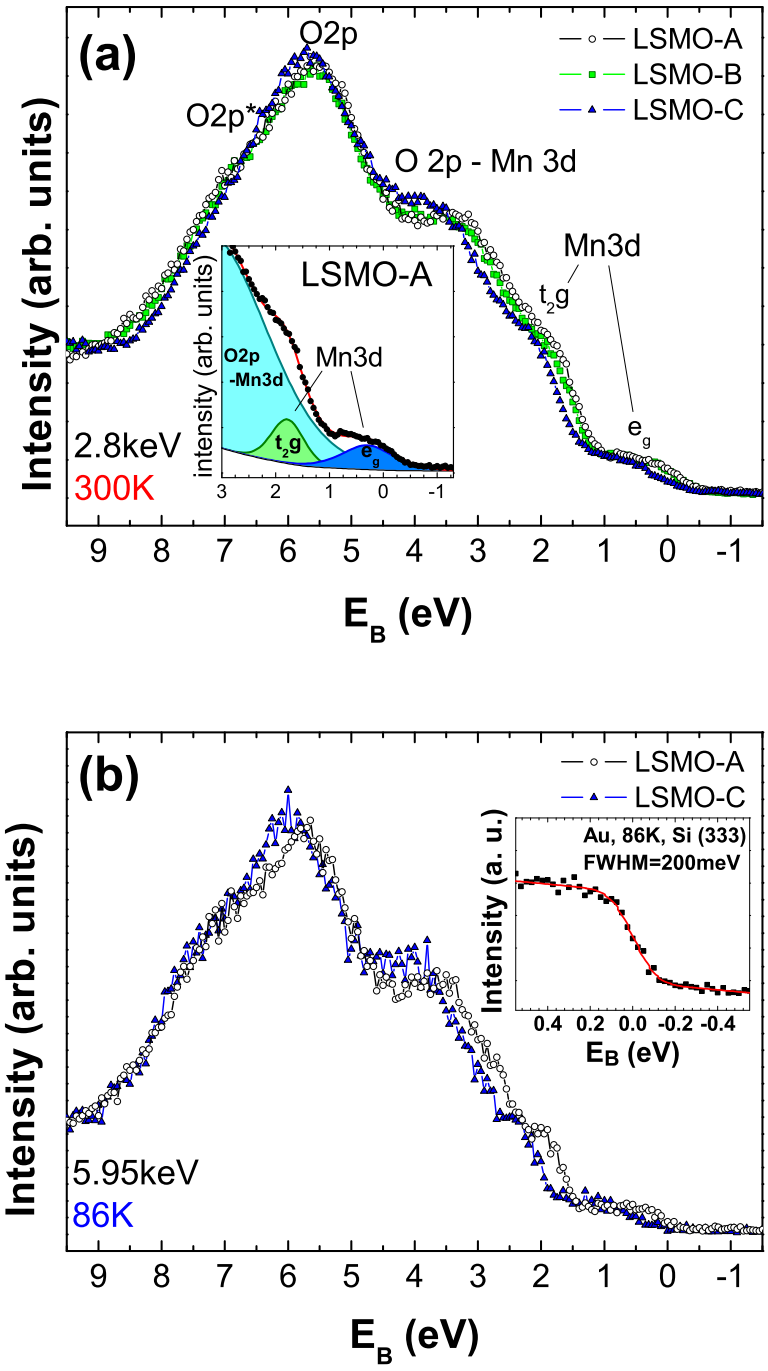

Figure 6.8.: Survey scans of the valence band recorded at (a) room temperature and 2.8 keV and (b) 86 K and 5.95 keV. For measurements at 5.95 keV a Si(333) post-monochromator was used to improve the energy resolution. The Fermi level of Au is shown in the inset of (b).

Table 6.3.: Binding energies of the valence band features. LT and RT indicate measurements performed at 86 K and at room temperature, respectively. The last rows, $\Delta E_{(LSMO\text{-}C)\text{-}(LSMO\text{-}A)}$, give the E_B difference between the untreated optimally doped sample (LSMO-A) and the most oxygen-depleted sample (LSMO-C) at RT.

sample	**hν** (keV)	**T** (K)	E_B (eV)			
			e_g	t_{2g}	Mn *3d* - O *2p*	O *2p*
LSMO-A	2.8	300	0.15	1.65	3.05	5.19
	5.95	86	0.27	1.60	3.28	5.21
	5.95	300	0.27	1.67	3.43	5.32
LSMO-B	2.8	300	0.27	1.84	3.22	5.35
	5.95	86	0.34	1.75	3.43	5.31
LSMO-C	2.8	300	0.53	1.9	3.35	5.57
	5.95	86	0.76	1.99	3.64	5.68
	5.95	300	0.97	2.12	3.68	5.64
$\Delta E_{(LSMO\text{-}C)\text{-}(LSMO\text{-}A)}$	2.8	300	0.38	0.25	0.3	0.38
	5.95	86	0.49	0.39	0.3	0.47

ture and the E_B of the states. For a quantitative comparison, the peak positions were extracted by a multi-peak fit. The inset of Figure 6.8(a) shows the fit of the LSMO-A sample for the binding energy range from -1.2 eV to 3 eV. The extracted peak positions for all of the samples are summarized in Table 6.3. The relative E_B difference between the LSMO-A and C samples ($\Delta E_{(LSMO\text{-}C)\text{-}(LSMO\text{-}A)}$) is shown in the last rows. In particular, a trend of shifts to higher E_B was found for: (i) longer annealing times, (ii) higher photon energy (5.95 keV),(iii) higher temperatures (85 K), and (iv) states with lower E_B.

Furthermore, there is a clear change of the energy band widths as a function of carrier concentration. The E_B increase of the e_g and t_{2g} states with reduced metallicity while the bottom of the valence band stays either fixed or moves slightly to lower E_B. These shifts result in an overall contraction of the valence band. Such an effect was experimentally inferred by X-ray absorption spectroscopy measurements,[137] but here it is measured directly. In strongly correlated systems, the electronic bands are not rigid for variations in the number of charge carriers. As a consequence, large energy band widths are associated with highly metallic samples, whereas in the less metallic sample (LSMO-C), consistent with the reduction of the energy band widths, electron localization effects are more likely.[164,165]

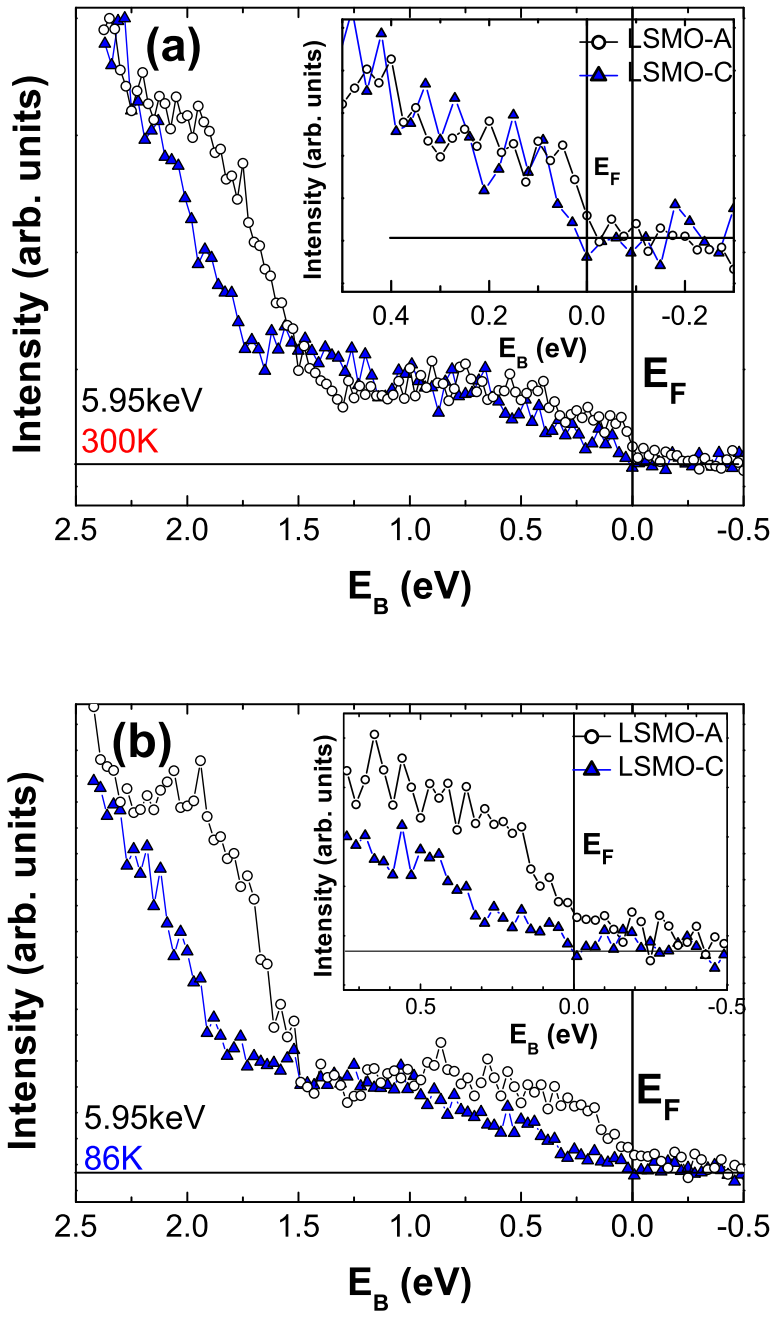

Figure 6.9.: High-resolution spectra of Mn $3d$ e_g states at (a) room temperature and (b) 86 K recorded at 5.95 keV. The photon energy of 5.95 keV was selected with a Si(333) post-monochromator to improve the energy resolution. The insets highlight the spectral region close to E_F.

Details of the t_{2g} and e_g states for LSMO-A and LSMO-C are shown in Figure 6.9(a) and (b) for measurements performed at RT and 86 K respectively. For the LSMO-A sample no significant differences in the e_g states are found between the two temperatures. Compared to LSMO-A at 86 K, LSMO-C shows a pronounced shift of the e_g states to a higher E_B. Nevertheless, the population of states up to E_F remains weak.

At room temperature the HAXPES data on LSMO-C in Figure 6.9(a) does not indicate the opening of a noticeable gap. This is in agreement with the transport measurements shown in Figure 6.3. An energy gap can be related to a polaron formation energy in terms of a thermally activated insulating state. In manganite systems, there is a universal linear relationship between the polaron formation energy and the T_{MI} value.[166] According to that linear relationship a T_{MI} value of about 270 K should correspond to a polaron formation energy of about 120 meV. No evidence of such gap opening has been observed in the temperature dependence of the valence band measurements (inset of Fig. 6.8(b)) within the experimental resolution. This allows us to rule out a polaron formation mechanism behind the insulating state of manganites close to T_{MI}.

6.4. Conclusions

The electronic properties of the strongly correlated manganite system were analyzed by means of the HAXPES technique and electronic transport measurements. Characterization by XRR showed that $La_{0.65}Sr_{0.35}MnO_3$ films grow in a layer-by-layer growth mode on $SrTiO_3$. The surface roughness increases only slightly from $\sim$1 ML to $\sim$2 ML after thermal treatment.

The transport measurements show a reduction of T_{MI} with increasing vacancy concentration. Fits of the metallic and insulating behaviors give indications for a Mott variable-range hopping mechanism.

The Mn valence states were examined via the Mn 3*s* exchange splitting. The observed reduction of valency with increasing oxygen deficiency gives evidence of a reduction in the hole doping level. Therefore, transport data could be correlated with the hole doping level.

The Mn 2*p* core levels show substantial differences in the metallic state of manganite systems. The well screened state at the Mn 2*p* level is reduced significantly as a result of the oxygen deficiency. Its disappearance indicates that the hybridization of the Mn 3*d* orbitals with the doping-induced states decreases.

Furthermore, the evaluation of the valence band spectra gives evidence of the effect of the carrier concentration on the binding energies of the Mn $3d$ e_g and t_{2g} states. The spectra show shifts of the Mn $3d$ states to higher E_B for oxygen-deficient samples. This ultimately leads to a reduction of the overall width of the valence band at lower charge densities. Moreover, consistent with the transport measurements, the valence band spectra do not show a significant opening of a band gap for the most oxygen-depleted $La_{0.65}Sr_{0.35}MnO_{3-\delta}$ sample above the T_{MI}. This finding supports a theoretical model with the insulating state resulting from Mott variable-range hopping rather than polaron formation.

7. Summary and Outlook

In this thesis, the origin of conductivity for a variety of different transition metal oxides was studied, namely, for films of $LaAlO_3$, $LaGaO_3$ and $NdGaO_3$ on $SrTiO_3$ (001), superlattices composed of $CaCuO_2$ and $SrTiO_3$, and oxygen-deficient $La_{0.65}Sr_{0.35}MnO_3$ films. The experiments were performed on ID32 at the ESRF, mainly employing hard X-ray photoelectron spectroscopy and the X-ray standing waves technique. The results provided insights into the unusual origins of the conductivity at the interfaces of transition metal oxide samples.

Hard X-ray photoelectron spectroscopy allows the bulk electronic structure to be measured, since the contributions from surface effects can be minimized. The large probing depth makes it an ideal technique for the study of interface properties. The combination of HAXPES with X-ray standing waves yields unique spatial information which make it an ideal tool for investigating conductivity in transition metal oxide systems.

Chapter 4 showed that the conductivity at the $LaAlO_3/SrTiO_3$ interface has two distinct contributions. The weak signature of charge carriers shows an in-gap state, a unique fingerprint associated with the oxygen vacancy related density of states, and, at the same time, shows Ti $3d$ states crossing E_F that support an intrinsic doping scenario. The formation of oxygen vacancies as a result of the growth conditions can be excluded. Thus, two contributions to the electron gas were identified, one fraction resulting from intrinsic electron doping from the polar $LaAlO_3$ layer, the remaining part originating from oxygen vacancies, induced by the polar overlayer, all occurring within a 2 nm (5uc) interfacial region in the $SrTiO_3$.

XSW imaging was employed to visualize the distortions in a two and a five monolayers thick $LaAlO_3$ film. The analysis indicates polar distortions and a modulation of the inter-planar spacing, both being more pronounced in the thinner film. Distortions were also observed for the $LaGaO_3$ films. The analysis indicates that the potential build-up is partially compensated by another mechanism than the distortion of the $LaAlO_3$ lattice. In agreement with the valence band decomposition, a possible mechanism may be the creation of vacancies due to a field-effect.

Furthermore, the OH-groups were found to adsorb in an ordered fashion on the $LaAlO_3$ surface. The stronger OH-feature for thicker films may indicate a connection with the build-up of the electrical potential with increasing film thickness.

For the epitaxial overlayers of orthorhombic $LaGaO_3$ and $NdGaO_3$ a combination of a $(\sqrt{2} \times \sqrt{2})R45°$ and a (2×1) double domain superstructure were observed. In $LaGaO_3$ films the $(\sqrt{2} \times \sqrt{2})R45°$ superstructure is preferred.

In Chapter 4 the feasibility of performing site-specific measurements of highly dilute, buried conduction electrons by making use of the site-specificity of the XSW method was demonstrated. This can be used to gain further insights in the conduction mechanisms at polar/non-polar interfaces and correlated electron systems in general. The XSW/HAXPES investigations of the 2D electron gas at the $LaAlO_3/SrTiO_3$ interface were facilitated by the high brightness and flux of the synchrotron photon source and the availability of high-throughput photoelectron analyzers such as the PHOIBOS 225 HV. New photoelectron analyzers with even higher transmission by wide-angle lenses, providing even higher sensitivity, will significantly benefit the further development of these techniques.

Chapter 5 presented results from HAXPES measurements on superconducting $CaCuO_2/SrTiO_3$ superlattices. In these samples, a electrostatic potential is expected to diverge, owing to the polar nature of the $CaCuO_2$ layers. A direct charge transfer between the $SrTiO_3$ and $CaCuO_2$ could be excluded from the measurements of the band alignment. The measurements showed that the build-up of the electrostatic potential was largely compensated by a redistribution of oxygen atoms at the interfaces.

Superconducting $CaCuO_2/SrTiO_3$ samples show multiple components in metal core level spectra providing evidence for a stronger oxidation of the interfacial plane. Furthermore, Cu $2p$ spectra show a decrease of the non-local screening channel which can be interpreted as evidence for an increased hole doping of the $CaCuO_2$ blocks.

In Chapter 6, the electronic properties of the strongly correlated manganite system were analyzed as a function of oxygen vacancy concentration. Characterization by XRR confirmed that the $La_{0.65}Sr_{0.35}MnO_3$ films grow in a layer-by-layer growth mode on $SrTiO_3$. No significant changes in surface roughness were observed if the samples were oxygen-depleted.

The metal–insulator transition temperature diminishes with increasing vacancy concentration and fits to the metallic and insulating characteristic curves are in support of a Mott variable-range hopping mechanism in the insulating regime. As further evidence, the evaluation of the Mn $3d$ e_g and t_{2g} states showed

shifts of the Mn 3*d* states to higher E_B in oxygen-deficient samples. This leads to an overall contraction of the valence band, indicative of stronger localization. Valence band spectra did not show a significant opening of a band gap for the most oxygen-depleted $La_{0.65}Sr_{0.35}MnO_3$ sample above the T_{MI}. This result supports a theoretical model with the insulating state resulting from Mott variable-range hopping rather than polaron formation.

The Mn valence is reduced with increasing oxygen deficiency in agreement with a reduction of the hole doping level. The analysis of the Mn 2*p* core levels indicates a decrease of the hybridization of the Mn 3*d* orbitals with the doping-induced states.

Finally, a number of questions arise from the results presented in this thesis which deserve to be addressed in further studies.

It should prove to be very interesting to conduct valence band decomposition studies on other metal oxide systems. For these studies, support from the theoretical side, to guide the interpretation, would be very useful. For example, in the $La_{1-x}Sr_xMnO_3$ system, changes in the hybridization of the Mn 3*d* and O 2*p* core levels that were deduced indirectly from the Mn 2*p* core level spectra could be detected directly. Experimentally a μm thick $La_{0.65}Sr_{0.35}MnO_3$ film could be rendered oxygen-deficient in-situ in consecutive annealing steps. A systematic study of the dependence of the doping level and different dopants in $SrTiO_3$ would provide a better understanding of this material.

Several interesting scientific questions remain unanswered concerning $CaCuO_2/SrTiO_3$ superlattices.

1. An extensive HAXPES study for a series of samples grown under different oxygen conditions should be conducted above and well below T_C ($\ll$40 K) with special focus on the Cu 2*p* core level and the valence band regions.

2. The appendix presents a preliminary XSW imaging study of a single $CaCuO_2/SrTiO_3$ slab under fluorescence excitation. Fluorescence is, however, hard to measure. The spectra are dominated by the substrate peaks causing problems with detector saturation. In addition, there is an overlap of emission lines (Ti, Ca with Nd) and the low-energy lines (e.g. Sr) are strongly attenuated in air. This could be overcome by measurements with a crystal spectrometer preferably under UHV conditions, or XSW imaging by means of HAXPES. For HAXPES measurements, the conductivity of the substrate must be ensured. The advantage of the HAXPES measurements would be the possibility of measuring the oxygen signal directly. These measurements should provide detailed information about the lattice distortions.

3. Another interesting question would be localizing the conductivity in these superlattices. Experimentally this could be achieved by depositing a thin $SrTiO_3/CaCuO_2$ superlattice slab in the range of five repeat units on a highly reflective metal multilayer mirror.[1] The measurements would be conducted under total reflection conditions. Several possible conclusions could be drawn from this experiment: (i) Determination of the interface roughness and intermixing. (ii) Localization of the additional components in the cation core levels and (iii) the Cu $2p$ screening features at the interface. (iv) The opening of a band gap in the $SrTiO_3$ blocks.

In conclusion, the experiments presented here highlight some of the exciting properties of oxide materials and the sensitive interplay of electronic and atomic structure. Since the first publications on $LaAlO_3/SrTiO_3$ in 2004, this field has developed into one of the most heavily researched areas in solid state physics. More and more polar/non-polar interfaces are being studied nowadays, moving from single interfaces to more complicated structures such as superlattices and sandwich structures and uncounted interesting scientific questions remain to be answered. With great curiosity we can anticipate the influence of oxide based electronics on future technology.

[1] To ensure epitaxy, the deposition of an oxide buffer layer may be necessary.

A. $CaCuO_2/La_{0.65}Sr_{0.35}O_3$ superlattices

This appendix presents preliminary HAXPES measurements of superconducting $CaCuO_2/La_{0.65}Sr_{0.35}O_3$ superlattices. The samples were grown under the same growth conditions as the $CaCuO_2/SrTiO_3$ superlattices presented in Chapter 5. Two superlattice samples were studied in this experiment, both consisting of 3 ML of $CaCuO_2$ alternating with 4 ML and 14 ML of $La_{0.65}Sr_{0.35}O_3$, respectively. The samples are referred to as 3×4 and 3×14 in the following. As reference samples, a bare $SrTiO_3$ substrate, a 10 nm thick $CaCuO_2$ film and a 14 ML $La_{0.65}Sr_{0.35}O_3$ film both grown on $NdGaO_3$ under conditions identical to those of the SC SL were measured. To avoid charging problems, the $SrTiO_3$ substrate was rendered slightly oxygen-deficient by vacuum annealing.

Section A.1 introduces the Mn 3*s* spectra and discusses the implications on the Mn valence states. In Section A.2 the Mn 2*p* core level spectra are presented. Section A.3 shows that characteristic core level shifts are observed for the $La_{0.65}Sr_{0.35}O_3$ core levels depending on the $La_{0.65}Sr_{0.35}O_3$ thickness.

Table A.1.: Fit results of the three components in Mn 3*s* and Cu 3*p* core levels. ΔE (2-1) is the exchange splitting and ν_{Mn} the calculated valence of the manganese.

	Mn 3*s*					**Cu 3*p***
	E_B (eV)			ΔE (2-1)	ν_{Mn}	E_B (eV)
sample	1	2	3			
3x4	83.62	89.16	92.82	5.54	2.8	75.2105
3x14	83.4	88.57	92.72	5.17	3.1	75.3620
14 ML Ref	83.43	88.45	92.81	5.01	3.3	...

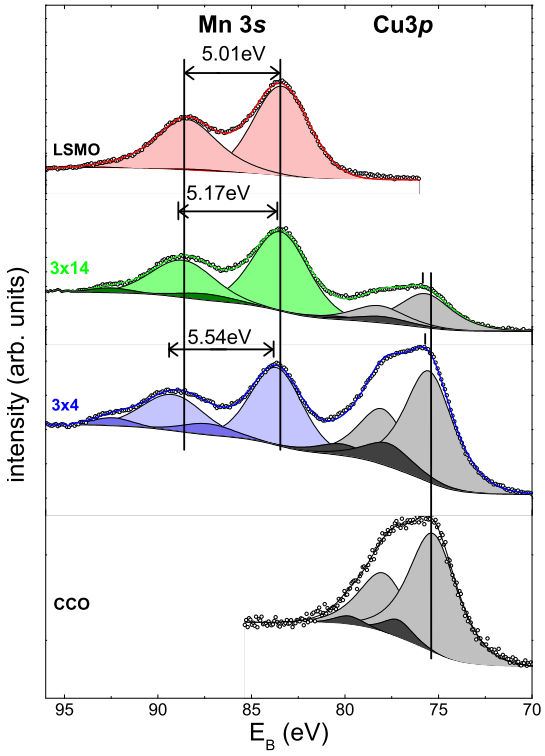

Figure A.1.: Mn 3s and Cu 3p core levels of the 3x4 3x14 superlattices and the 14 ML $La_{0.65}Sr_{0.35}O_3$ reference. A Cu 3p core level of a $CaCuO_2$ film is shown as a reference as well.

A.1. Mn 3s exchange splitting

Mn 3s spectra show an exchange splitting. Figure A.1 presents photoelectron spectra in the binding energy (E_B) range 68 eV to 96 eV for the 2 SLs and the reference samples. For the SL samples, the spectra show an overlap of the Cu 3p and Mn 3s core levels. Individual components were extracted in deconvolution procedures for the Mn 3s peak and the Cu 3p peak. Table A.1 summarizes the positions of the components presented in Figure A.1. The best fit was achieved using a doublet for the Cu 3p peak and two doublets for the Mn 3s peak. The exchange splitting increases in the multilayer samples with respect to the $La_{0.65}Sr_{0.35}O_3$ reference. As described in Chapter 2 the spin moment of the Mn and hence the Mn valence, ν_{Mn}, can be obtained from the value of the splitting.

For the reference sample, this corresponds to a valence ν_{Mn} of 3.3, very close to the value for the ideal doping level. For the 3x14 sample, is increased to a ν_{Mn} of 3.1. For the 3x4 sample, ν_{Mn} shows a clear decrease to about 2.8.

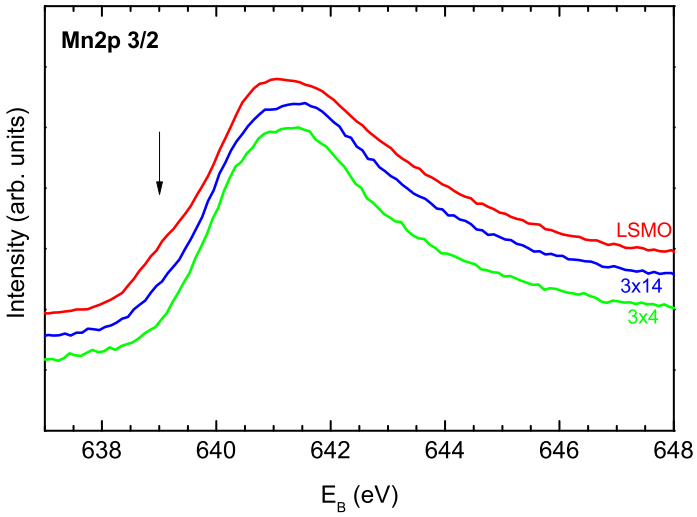

Figure A.2.: Mn 2*p* core levels of the 3x4 3x14 superlattices and the 14 ML $La_{0.65}Sr_{0.35}O_3$ reference sample measured at 5.95 keV without the post monochromator. A shoulder is visible on the low E_B side at 639 eV, as indicated by the arrow.

The change of ν_{Mn} can be interpreted as a sign for an electron transfer to the $La_{0.65}Sr_{0.35}O_3$ layer. For the 3x4 sample, this corresponds to a transfer of 0.5 electrons per $La_{0.65}Sr_{0.35}O_3$ unit cell. Considering 4 ML per $La_{0.65}Sr_{0.35}O_3$ block this means that 1.2 e^- are transferred from the $CaCuO_2$ slab to the $La_{0.65}Sr_{0.35}O_3$ layer. This may indicate a charge transfer from $CaCuO_2$ into the $La_{0.65}Sr_{0.35}O_3$ layers.

The origin of the second doublet in the Mn 3*s* spectra is not clear at present.

A.2. Mn 2*p* screening state

Figure A.2 shows Mn 2*p* core level spectra for the 3x4 SL, 3x14 SL and the 14 ML $La_{0.65}Sr_{0.35}O_3$ reference. The 'well screened' state is visible for the $La_{0.65}Sr_{0.35}O_3$ reference, but disappears for the multilayer samples.

Following the discussion in Chapters 2 and 6, the presence of the well-screened feature in Mn 2*p* core level spectra can be interpreted as a sign for a high carrier density at E_F and of strong hybridization with the Mn 3*d* states. The disappearance of the screening feature agrees qualitatively with the observed changes in the

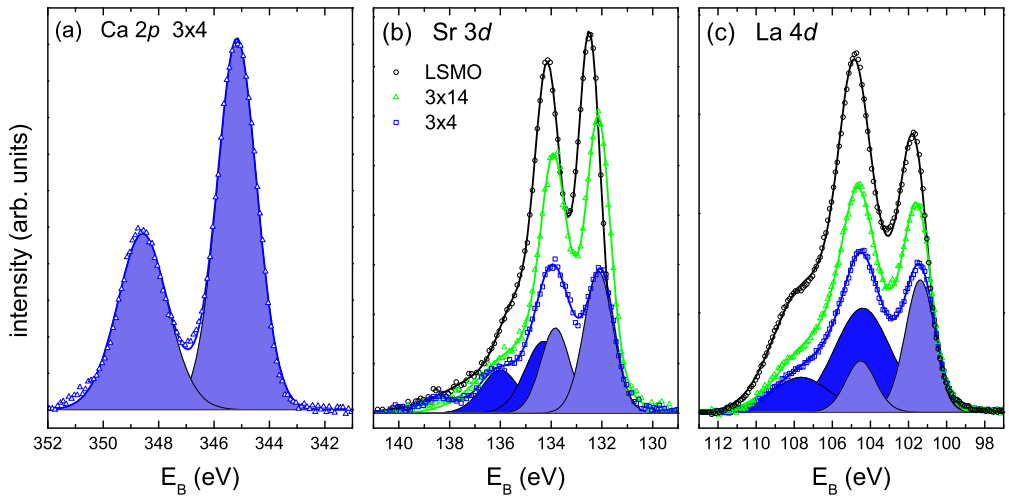

Figure A.3.: (a) Ca 2*p* core-level spectra for the 3x4 sample show no pronounced additional components. (b) Sr 3*d* and (c) La 4*d* core-level spectra from the 3x4 and 3x14 superlattices and the 14 ML $La_{0.65}Sr_{0.35}O_3$ reference consist of two, or more, doublets.

Mn valence, namely an electron uptake and hence a decrease in the hole doping concentration.

A.3. Core level shifts

Figure A.3(a) shows Ca 2*p* core-level spectra for the 3x4 sample. The spectra show no pronounced additional components.

The $La_{0.65}Sr_{0.35}O_3$ core levels shift to lower binding energies in the films with thinner $La_{0.65}Sr_{0.35}O_3$ interlayers. This behavior is similar to the shifts observed in the $CaCuO_2/SrTiO_3$ superlattices, but is significantly less pronounced. This effect can be seen in the La 4*d* and Sr 3*d* core-level spectra in Figure A.3(b) and (c). The peak positions are summarized in Table A.2.

The $CaCuO_2$ core levels appear to be shifted with respect to the $CaCuO_2/SrTiO_3$ superlattices to ∼1eV higher binding energies.

Table A.2.: Fit results of the La $4p$ $4d$and Sr $3d$ core levels. The binding energy and core level shift with respect to the 14 ML reference are listed.

sample	**La $4p_{3/2}$**	**ΔE**	**La $4d$**	**ΔE**	**Sr $3d$**	**ΔE**
3x4	194.761	0.37	101.383	0.329	132.028	0.458
3x14	194.957	0.174	101.518	0.194	132.116	0.37
14 ML Ref	195.131	0.0	101.712	0.0	132.486	0.0

B. XSW-imaging of a thin $CaCuO_2$ film

A $CaCuO_2/SrTiO_3$ slab grown on $NdGaO_3$ was studied by XSW real space imaging. The initial goal was to identify possible distortions in the $CaCuO_2$ lattice and possibly provide evidence for oxygen in the Ca-planes. Since the sample was insulating, HAXPES measurements were hampered by charging effects. Hence, XSW experiments using fluorescence detection in EH1 were performed instead. The XSW-modulated yield of the Cu Kα and Ca L fluorescence was investigated for 12 reflections from the $NdGaO_3$ substrate.

The sample consisted of a 3 ML thick $CaCuO_2$ layer, capped with a 2 ML thick $SrTiO_3$ layer grown on NdO_2 terminated $NdGaO_3(110)$ surfaces. The sample was deposited under exactly the same conditions as the superconducting SL. Thus, the $CaCuO_2/SrTiO_3$ overlayer corresponds to one repeat unit of the superconducting superlattices presented in Chapter 5. The orthorhombic **c**-axis of the substrate was aligned in-plane.

An excitation energy of 10 keV was selected using the double-crystal monochromator and the energy bandwidth was further reduced by the Si(444) post-monochromator. The XSW-modulated fluorescence yield was studied with a VORTEX detector for the Cu Kα and Ca Kα lines on the six-circle diffractometer installed in EH1. Each reflection (hkl) was aligned individually. The intensity of the diffracted and the inelastically scattered photons was detected while scanning the rocking curve of the reflection in θ.

A fluorescence spectrum of the sample is shown in Figure B.1. The spectrum is dominated by the strong Nd L lines in the energy range from 4.5 keV to 7.5 keV. The Cu Kα lines are visible as a single one peak centered close to 8 keV. The inset of Figure B shows the spectral range from 2.5 keV to 4.4 keV. The extraction of the Ca fluorescence yield is complicated by their overlap with the Nd L escape peaks, Nd L*.[1] The PyMCA program, was used to separate the spectral contributions

[1] When using a Si solid state detector, the emitted photons can themselves excite fluorescence in the Si photo diode. These peaks can be found 1.74 keV below the original line in the spectra.

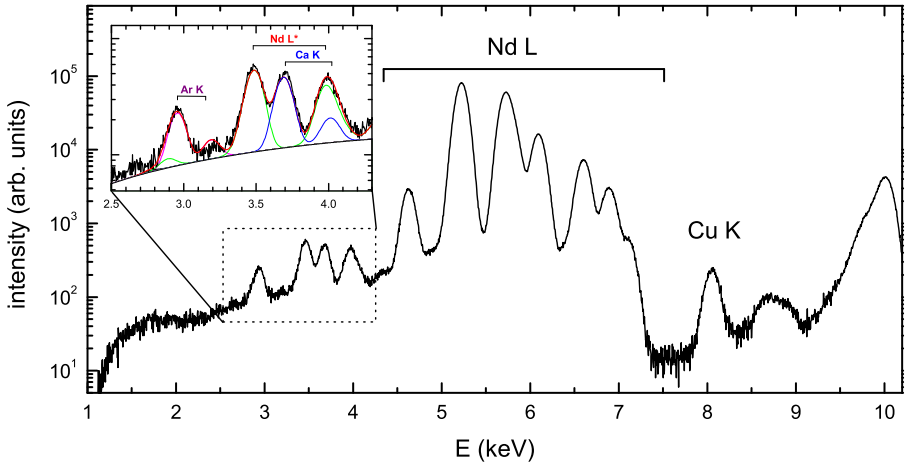

Figure B.1.: X-ray fluorescence spectrum from a 2 ML thick $CaCuO_2$ film on $NdGaO_3$ measured at an excitation energy of 10 keV. The spectrum is dominated by the Nd L lines. The Cu KL2 and KL3 lines are found at 8 keV, the Cu KM3 line at 8.9 keV. The inset shows the spectral region from 2.5 keV to 4.3 keV. The Ca K lines overlap with the Nd L* escape peak and the Ar K lines.

from the Ca K, Nd L* and Ar K lines and obtain the fluorescence yield of the Cu K and Ca K lines for the reflections listed in Table B.1.

Figure B.2(a) shows a selection of representative fluorescence yield and reflectivity curves. The solid lines show the best fit curves to the data. The Fourier components determined for the measured reflections (hkl) are presented in Table B.1. In the second column the indices $(hkl)_{cub}$ respective to the pseudo-cubic lattice are given. The Ca signal in the XFS spectra was very weak and did not provide an adequate signal-to-noise ratio for a reliable analysis for all of the reflections.

The data sets were expanded assuming a P4mm symmetry. Formally, the $NdGaO_3$ (110) surface has a p2 symmetry, however, since only displacements along z are considered in the analysis, the generalization is valid.

In Figure B.2(b), a real space image for Cu is presented. The black box represents the extended pseudo-cubic $NdGaO_3$ unit cell. The atomic density of Cu is marked in red. The positions showing the maximum atomic density are found at two symmetrically inequivalent sites, slightly above the positions corresponding to a bcc lattice. The two positions are found to have equal intensities. The doubling of the number of atomic sites can be attributed to missing low-order reflections.

Table B.1.: Best fit results for the XSW data recorded from a $CaCuO_2/SrTiO_3$ slab on a $NdGaO_3(110)$ substrate. The corresponding curve fits are shown can be found in Figure B.2(a)

		Cu		**Ca**	
(hkl)	$(hkl)_{cub}$	fH	PH	fH	PH
2 2 0	0 0 2	0.239	0.201	...	...
4 4 0	0 0 4	0.421	0.012	...	...
4 2 0	2 2 2	0.145	0.14	0.16	1.05
1 1 2	1 0 1	0.214	0.206	...	...
3 3 2	1 0 3	0.145	0.14	0.16	1.05
5 5 2	1 0 5	0.451	0.07	...	...
3 1 2	1 1 2	0.29	0.23	0.29	0.83
5 3 2	1 1 4	0.127	1.031	0.17	0.88
1 3 2	1 1 2	0.29	0.23	0.29	0.83
5 1 2	1 2 3	0.225	0.279	0.1	0.47
4 2 4	2 1 3	0.37	0.214	0.11	0.28
3 -1 2	1 1 2	0.2	0.175	...	...

Even using the (002) reflection it is not possible to distinguish between the two positions because it also has a short XSW periodicity.

With respect to the extended pseudocubic $NdGaO_3$ lattice (**c***≈ 3.86 Å) the positions z = 0.5356 and z = 1.0356 correspond to an averaged outwards displacement of 0.137 Å. The relaxed $CaCuO_2$ **c**-lattice constant has the value 3.18 Å.[167] Thus, the observed Cu positions correspond to an expansion of the $CaCuO_2$ lattice by an average of 0.817 Å. The observed deviation of the Cu position can be interpreted as a response to the potential build-up, similar to the one observed in $SrTiO_3/LaAlO_3$, and the oxygen uptake in the Ca-planes.

Real space images calculated for Ca do not show maxima with high intensity. This is probably due to the low coherent fractions obtained in the fits to the fluorescence yield (see Table B.1).

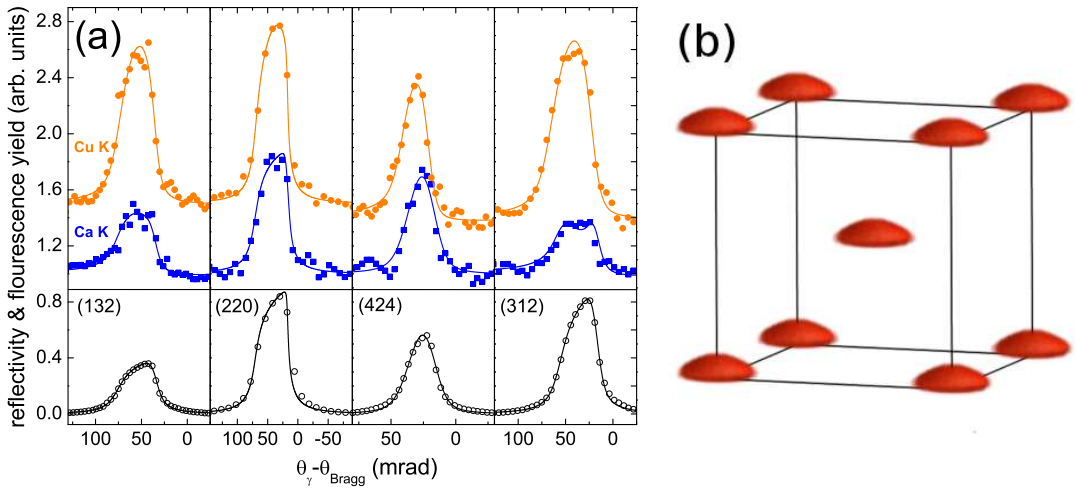

Figure B.2.: (a) XSW modulated fluorescence yield curves (filled symbols) and the corresponding reflectivity curves (open symbols) measured at 10 keV. The Cu yield curves are offset by 0.5 for better visibility. The solid lines show the best fit curves to the data. (b) 3D atomic density map for Cu. The black lines indicate the pseudo-cubic unit cell of the $NdGaO_3$ substrate.

C. Determination of the Nb-site in Nb:$SrTiO_3$

Nb:$SrTiO_3$ was studied to determine the lattice sites occupied by the Nb-dopant atoms. Although the Ti-site is the most probable location, a partial occupation of other lattice sites, or the formation of clusters of metallic Nb, is also possible. The transport properties of $SrTiO_3$ would be strongly influenced by the formation of Nb-clusters, since they would not participate in the doping process.

XSW imaging is a suitable technique for measurements of this kind. Alternative lattice sites are revealed directly in the real space images and the presence of Nb-clusters results in diminished coherent fractions in the individual XSW scans.

XSW measurements were preformed using the HAXPES setup of ID32 in backscattering geometry for the (111), (002), (112), (202), (103) and (222) reflections from $SrTiO_3$ by collecting the XSW-modulated photoelectron yield for the Ti $2p$ and Nb $3d$ core levels. The measured data (open symbols) and the best fit curves (solid lines) are presented in Figure C.1, the fit results are summarized in Table C.1.

The very similar coherent positions for both Nb and Ti shows that the Nb atoms only occupy Ti lattice sites. There are some minor discrepancies in the coherent fractions which may be attributed to non-dipolar effects.

Table C.1.: Best fit results from the XSW data recorded using the Ti 2*p* and Nb 3*d* core levels in 2 at. % Nb-doped $SrTiO_3$. The corresponding fits are shown in Figure C.1.

	Ti		**Nb**	
(hkl)	fH	PH	fH	PH
1 1 1	0.823	0.530	1.294	0.534
0 0 2	0.927	0.046	1.125	0.084
1 1 2	0.838	0.004	0.941	0.018
2 0 2	0.829	1.002	0.73	0.004
1 0 3	0.835	0.062	0.826	0.082
2 2 2	1.048	1.020	0.863	1.003

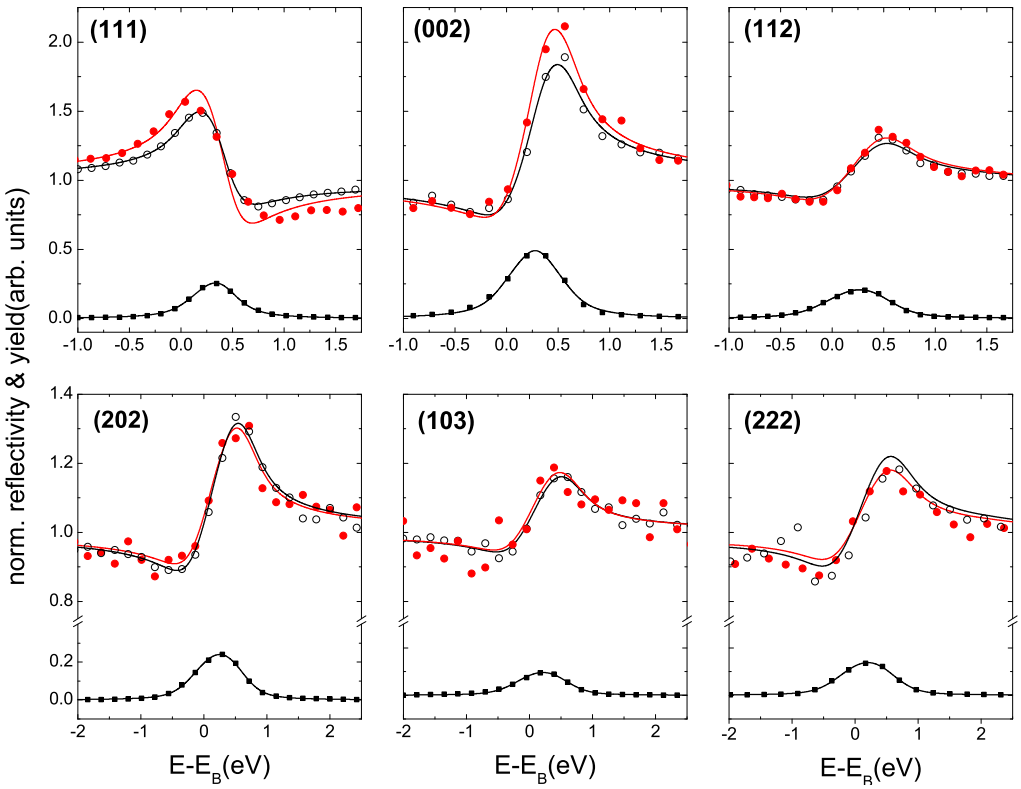

Figure C.1.: XSW-modulated photoelectron yield curves of Ti 2p (open black circles) and Nb 3d (filled red circles) core levels and the corresponding reflectivity curves (squares) for the (111), (002), (112), (202), (103, and (222) reflections from $SrTiO_3$. The solid lines show the best fit curves to the data.

Bibliography

[1] G. A. Prinz, "Spin-Polarized Transport," *Phys. Today* **48**, 58 (1995). 1

[2] O. Auciello, J. F. Scott, and R. Ramesh, "The physics of ferroelectric memories," *Phys. Today* **51**, 22 (1998). 1

[3] P. J. van der Zaag, P. J. H. Bloemen, J. M. Gaines, R. M. Wolf, P. A. A. van der Heijden, R. J. M. van de Veerdonk, and W. J. M. de Jonge, "On the construction of an Fe_3O_4-based all-oxide spin valve," *J. Magn. Magn. Mater.* **211**, 301 (2000). 1

[4] A. Ohtomo and H. Y. Hwang, "A high-mobility electron gas at the $LaAlO_3/SrTiO_3$ heterointerface," *Nature* **427**, 423 (2004). 1, 37, 39, 43, 92

[5] J. M. D. Coey, M. Viret, and S. von Molnár, "Mixed-valence manganites," *Adv. Phys.* **48**, 167 (1999). 2, 110, 113, 117

[6] L. P. Gor'kov and V. Z. Kresin, "Mixed-valence manganites: fundamentals and main properties," *Phys. Rep.* **400**, 149 (2004). 2, 110, 113

[7] J. C. Woicik, E. J. Nelson, L. Kronik, M. Jain, J. R. Chelikowsky, D. Heskett, L. E. Berman, and G. S. Herman, "Hybridization and Bond-Orbital Components in Site-Specific X-Ray Photoelectron Spectra of Rutile TiO_2," *Phys. Rev. Lett.* **89**, 077401 (2002). 2, 25

[8] J. C. Woicik, M. Yekutiel, E. J. Nelson, N. Jacobson, P. Pfalzer, M. Klemm, S. Horn, and L. Kronik, "Chemical bonding and many-body effects in site-specific x-ray photoelectron spectra of corundum V_2O_3," *Phys. Rev. B* **76**, 165101 (2007). 2, 44

[9] S. Thiess, T. Lee, F. Bottin, and J. Zegenhagen, "Valence band photoelectron emission of $SrTiO_3$ analyzed with X-ray standing waves," *Solid State Commun.* **150**, 553 (2010). 2, 25, 44, 83

[10] C. Aruta, C. Schlueter, T.-L. Lee, D. Di Castro, D. Innocenti, A. Tebano, J. Zegenhagen, and G. Balestrino, "Interfaces reconstruction in novel superconducting $CaCuO_2/SrTiO_3$ superlattices," *to be published* (2012). 4, 91

[11] C. Schlueter, P. Orgiani, T.-L. Lee, A. Y. Petrov, A. Galdi, B. A. Davidson, J. Zegenhagen, and C. Aruta, "Evidence of electronic band redistribution in $La_{0.65}Sr_{0.35}MnO_{3-\delta}$ by hard x-ray photoelectron spectroscopy," *Phys. Rev. B* **86**, 155102 (2012). 4, 109

[12] J. B. Goodenough, "Electronic and ionic transport properties and other physical aspects of perovskites," *Rep. Prog. Phys.* **67**, 1915 (2004). 5

[13] D. Goldschmidt and H. L. Tuller, "Fundamental absorption edge of $SrTiO_3$ at high temperatures," *Phys. Rev. B* **35**, 4360 (1987). 6, 97

[14] V. M. Goldschmidt, "Die Gesetze der Krystallochemie," *Naturwissenschaften* **14**, 477 (1926), 10.1007/BF01507527. 7

[15] R. D. Shannon, "Revised effective ionic radii and systematic studies of interatomic distances in halides and chalcogenides," *Acta Crystallogr. A* **32**, 751 (1976). 7

[16] A. M. Glazer, "Simple ways of determining perovskite structures," *Acta Crystallogr. A* **31**, 756 (1975). 7

[17] L. Vasylechko, A. Matkovskii, D. Savytskii, A. Suchocki, and F. Wallrafen, "Crystal structure of $GdFeO_3$-type rare earth gallates and aluminates," *J. Alloys Compd.* **291**, 57 (1999). 8

[18] R. von Helmolt, J. Wecker, B. Holzapfel, L. Schultz, and K. Samwer, "Giant negative magnetoresistance in perovskitelike $La_{2/3}Ba_{1/3}MnO_x$ ferromagnetic films," *Phys. Rev. Lett.* **71**, 2331 (1993). 8, 110, 111

[19] A. Urushibara, Y. Moritomo, T. Arima, A. Asamitsu, G. Kido, and Y. Tokura, "Insulator-metal transition and giant magnetoresistance in $La_{1-x}Sr_xMnO_3$," *Phys. Rev. B* **51**, 14103 (1995). 8, 110, 111, 116, 120, 121

[20] J. Park, E. Vescovo, H. Kim, C. Kwon, R. Ramesh, and T. Venkatesan, "Direct evidence for a half-metallic ferromagnet," *Nature* **392**, 794 (1998). 8, 110

[21] C. H. Ahn, J. Triscone, and J. Mannhart, "Electric field effect in correlated oxide systems," *Nature* **424**, 1015 (2003). 8, 112

[22] H. Lehnert, H. Boysen, P. Dreier, and Y. Yu, "Room temperature structure of $LaAlO_3$," *Z. Kristallogr.* **215**, 145 (2000). 8

[23] T. Siegrist, S. M. Zahurak, D. W. Murphy, and R. S. Roth, "The parent structure of the layered high-temperature superconductors," *Nature* **334**, 231 (1988). 9

[24] M. Smith, A. Manthiram, J. Zhou, J. Goodenough, and J. Markert, "Electron-doped Superconductivity at 40-K in the infinite-layer compound $Sr_{1-y}Nd_YCuO_2$," *Nature* **351**, 549 (1991). 9

[25] G. Balestrino, P. G. Medaglia, P. Orgiani, A. Tebano, C. Aruta, S. Lavanga, and A. A. Varlamov, "Very large purely intralayer critical current density in ultrathin cuprate artificial structures," *Phys. Rev. Lett.* **89**, 156402 (2002). 9, 92

[26] P. Orgiani, C. Aruta, G. Balestrino, D. Born, L. Maritato, P. G. Medaglia, D. Stornaiuolo, F. Tafuri, and A. Tebano, "Direct Measurement of Sheet Resistance $R_\square$ in Cuprate Systems: Evidence of a Fermionic Scenario in a Metal-Insulator Transition," *Phys. Rev. Lett.* **98**, 036401 (2007). 9, 92

[27] D. Di Castro, M. Salvato, A. Tebano, D. Innocenti, C. Aruta, W. Prellier, O. I. Lebedev, I. Ottaviani, N. B. Brookes, M. Minola, M. Moretti Sala, C. Mazzoli, P. Medaglia, G. Ghiringhelli, L. Braicovich, M. Cirillo, and G. Balestrino, "High T_c superconductivity in superlattices of insulating oxides,", `arXiv:1107.2239v2 [cond-mat.supr-con]`. 9, 92, 93, 95

[28] D. Di Castro, "Private communication,". 9, 92

[29] C. Aruta, S. Amoruso, R. Bruzzese, X. Wang, D. Maccariello, F. Miletto Granozio, and U. Scotti di Uccio, "Pulsed laser deposition of $SrTiO_3/LaGaO_3$ and $SrTiO_3/LaAlO_3$: Plasma plume effects," *Appl. Phys. Lett.* **97**, 252105 (2010). 10, 40, 41, 51

[30] M. N. R. Ashfold, F. Claeyssens, G. M. Fuge, and S. J. Henley, "Pulsed laser ablation and deposition of thin films," *Chem. Soc. Rev.* **33**, 23 (2004). 10

[31] T. J. Jackson and S. B. Palmer, "Oxide superconductor and magnetic metal thin film deposition by pulsed laser ablation: a review," *J. Phys. D: Appl. Phys.* **27**, 1581 (1994). 10

[32] P. Willmott, "Deposition of complex multielemental thin films," *Prog. Surf. Sci.* **76**, 163 (2004). 10

[33] C. Giacovazzo, H. L. Monaco, D. Artioli, D. Viterbo, G. G. Ferraris, G. Gilli, G. Zanotti, and M. Catti, *Fundamentals of Crystallography. International Union of Crystallography*IUCr Texts on Crystallography, 2nd ed. (Oxford University Press, 1993). 14

[34] I. K. Robinson, "Crystal truncation rods and surface roughness," *Phys. Rev. B* **33**, 3830 (1986). 15, 79

[35] J. H. Scofield, *Theoretical photoionization cross sections from 1 to 1500 keV* (Lawrence Livermore National Laboratory Report UCRL-51326, 1973). 16

[36] S. Hüfner, *Photoelectron Spectroscopy* (Springer Verlag, Heidelberg, Germany, 1995). 17, 18

[37] C. S. Fadley, *Electron Spectroscopy: Theory, Techniques and Applications*volume 2 (Accademic Press, 1978). 17, 18

[38] J. F. Watts and J. Wolstenholme, *An Introduction to Surface Analysis by XPS and AES* (John Wiley & Sons, Ltd, 2005). 19

[39] S. Hagström, C. Nordling, and K. Siegbahn, "Electron spectroscopic determination of the chemical valence state," *Z. Phys. A-Hadron.Nucl.* **178**, 439 (1964), 10.1007/BF01379473. 19

[40] C. S. Fadley, D. A. Shirley, A. J. Freeman, P. S. Bagus, and J. V. Mallow, "Multiplet Splitting of Core-Electron Binding Energies in Transition-Metal Ions," *Phys. Rev. Lett.* **23**, 1397 (1969). 20, 113

[41] N. Mannella, C. H. Booth, A. Rosenhahn, B. C. Sell, A. Nambu, S. Marchesini, B. S. Mun, S. Yang, M. Watanabe, K. Ibrahim, E. Arenholz, A. Young, J. Guo, Y. Tomioka, and C. S. Fadley, "Temperature-dependent evolution of the electronic and local atomic structure in the cubic colossal magnetoresistive manganite $La_{1-x}Sr_xMnO_3$," *Phys. Rev. B* **77**, 125134 (2008). 20, 113

[42] K. Horiba, M. Taguchi, A. Chainani, Y. Takata, E. Ikenaga, D. Miwa, Y. Nishino, K. Tamasaku, M. Awaji, A. Takeuchi, M. Yabashi, H. Namatame, M. Taniguchi, H. Kumigashira, M. Oshima, M. Lippmaa, M. Kawasaki, H. Koinuma, K. Kobayashi, T. Ishikawa, and S. Shin, "Nature of the Well Screened State in Hard X-Ray Mn 2*p* Core-Level Photoemission Measurements of $La_{1-x}Sr_xMnO_3$ Films," *Phys. Rev. Lett.* **93**, 236401 (2004).

20, 113, 122

[43] M. A. van Veenendaal, "Competition between screening channels in core-level X-ray photoemission as a probe of changes in the ground-state properties of transition-metal compounds," *Phys. Rev. B* **74**, 085118 (2006). 20, 21, 106, 113, 122

[44] A. Sandell and A. J. Jaworowski, "The Mn 2*p* core-level photoelectron spectrum of Pd-Mn bimetallic systems on Pd(1 0 0)," *J. Electron Spectrosc.* **135**, 7 (2004). 20, 113, 122

[45] S. Tanuma, C. J. Powell, and D. R. Penn, "Calculation of electron inelastic mean free paths (IMFPs) VII. Reliability of the TPP-2M IMFP predictive equation," *Surf. Interface Anal.* **35**, 268 (2003). 22, 30

[46] S. Tanuma, C. J. Powell, and D. R. Penn, "Calculations of electron inelastic mean free paths. IX. Data for 41 elemental solids over the 50 eV to 30 keV range," *Surf. Interface Anal.* **43**, 689 (2011). 22

[47] D. P. Woodruff, B. C. C. Cowie, and A. R. H. F. Ettema, "Surface structure determination using X-ray standing waves: a simple view," *J. Phys.: Condens. Matter* **6**, 10633 (1994). 23

[48] J. Zegenhagen, "Surface-structure determination with X-ray standing waves," *Surf. Sci. Rep.* **18**, 199 (1993). 23

[49] B. W. Batterman, "Effect of Dynamical Diffraction in X-Ray Fluorescence Scattering," *Physical Review* **133**, A759 (1964). 25

[50] J. C. Woicik *et al.*, "X-ray standing-wave investigations of valence electronic structure," *Phys. Rev. B* **64**, 125115 (2001). 26

[51] S. Thieß, *Interface Structure and Electronic Properties of $SrTiO_3$ and $YBa_2Cu_3O_{7-\delta}$ Crystals and Thin Films*, PhD thesis Universtät Hamburg 2007. 26

[52] J. Zegenhagen *et al.*, "X-ray standing waves and hard X-ray photoelectron spectroscopy at the insertion device beamline ID32," *J. Electron Spectrosc.* **178-179**, 258 (2010). 31

[53] F. Sette, "http://www.esrf.eu/news/general/Beamline-closure/," 2011. 31

[54] S. Thiel, "Tunable Quasi-Two-Dimensional Electron Gases in Oxide Heterostructures," *Science* **313**, 1942 (2006). 37

[55] C. Bell, S. Harashima, Y. Hikita, and H. Y. Hwang, "Thickness dependence of the mobility at the $LaAlO_3/SrTiO_3$ interface," *Appl. Phys. Lett.* **94**, 222111 (2009). 37

[56] H. Chen, A. M. Kolpak, and S. Ismail-Beigi, "Electronic and Magnetic Properties of $SrTiO_3/LaAlO_3$ Interfaces from First Principles," *Adv. Mater.* **22**, 2881 (2010). 37

[57] C. Cantoni, J. Gazquez, F. Miletto Granozio, M. P. Oxley, M. Varela, A. R. Lupini, S. J. Pennycook, C. Aruta, U. S. di Uccio, P. Perna, and D. Maccariello, "Electron Transfer and Ionic Displacements at the Origin of the 2D Electron Gas at the LAO/STO Interface: Direct Measurements with Atomic-Column Spatial Resolution," *Adv. Mater.* **24**, 3952 (2012). 37, 41, 61, 87

[58] P. W. Tasker, "The stability of ionic crystal surfaces," *Journal of Physics C: Solid State Physics* **12**, 4977 (1979). 38

[59] C. Noguera, *Physics and Chemistry of Oxide Surfaces* (Cambridge University Press, 1996). 39

[60] Z. Zhong, P. X. Xu, and P. J. Kelly, "Polarity-induced oxygen vacancies at $LaAlO_3/SrTiO_3$ interfaces," *Phys. Rev. B* **82**, 165127 (2010). 39, 41, 87

[61] N. Nakagawa, H. Y. Hwang, and D. A. Muller, "Why some interfaces cannot be sharp," *Nat. Mater.* **5**, 204 (2006). 39, 40, 43, 92, 93

[62] J. Lee and A. A. Demkov, "Charge origin and localization at the n-type $SrTiO_3/LaAlO_3$ interface," *Phys. Rev. B* **78**, 193104 (2008). 40, 87

[63] C. Cen, S. Thiel, G. Hammerl, C. W. Schneider, K. E. Andersen, C. S. Hellberg, J. Mannhart, and J. Levy, "Nanoscale control of an interfacial metal-insulator transition at room temperature," *Nat. Mater.* **7**, 298 (2008). 40

[64] K. Yoshimatsu, R. Yasuhara, H. Kumigashira, and M. Oshima, "Origin of Metallic States at the Heterointerface between the Band Insulators $LaAlO_3$ and $SrTiO_3$," *Phys. Rev. Lett.* **101**, 026802 (2008). 40

[65] Y. Segal, J. H. Ngai, J. W. Reiner, F. J. Walker, and C. H. Ahn, "X-ray photoemission studies of the metal-insulator transition in $LaAlO_3/SrTiO_3$ structures grown by molecular beam epitaxy," *Phys. Rev. B* **80**, 241107 (2009). 40

[66] B.-C. Huang, Y.-P. Chiu, P.-C. Huang, W.-C. Wang, V. T. Tra, J.-C. Yang, Q. He, J.-Y. Lin, C.-S. Chang, and Y.-H. Chu, "Mapping Band Alignment across Complex Oxide Heterointerfaces," *Phys. Rev. Lett.* **109**, 246807 (2012). 40

[67] P. R. Willmott *et al.*, "Structural Basis for the Conducting Interface between $LaAlO_3$ and $SrTiO_3$," *Phys. Rev. Lett.* **99**, 155502 (2007). 40, 41, 43, 93

[68] R. Pentcheva and W. E. Pickett, "Charge localization or itineracy at $LaAlO_3/SrTiO_3$ interfaces: Hole polarons, oxygen vacancies, and mobile electrons," *Phys. Rev. B* **74**, 035112 (2006). 40, 87

[69] S. A. Pauli *et al.*, "Evolution of the Interfacial Structure of $LaAlO_3$ on $SrTiO_3$," *Phys. Rev. Lett.* **106**, 036101 (2011). 40, 41, 75, 92

[70] N. Reyren *et al.*, "Superconducting Interfaces Between Insulating Oxides," *Science* **317**, 1196 (2007). 40, 43

[71] A. Kalabukhov, R. Gunnarsson, J. Börjesson, E. Olsson, T. Claeson, and D. Winkler, "Effect of oxygen vacancies in the $SrTiO_3$ substrate on the electrical properties of the $LaAlO_3/SrTiO_3$ interface," *Phys. Rev. B* **75** (2007). 40, 43, 87

[72] M. Basletic, J. Maurice, C. Carretero, G. Herranz, O. Copie, M. Bibes, E. Jacquet, K. Bouzehouane, S. Fusil, and A. Barthelemy, "Mapping the spatial distribution of charge carriers in $LaAlO_3/SrTiO_3$ heterostructures," *Nat. Mater.* **7**, 621 (2008). 40, 62, 64

[73] A. Dubroka, M. Rössle, K. W. Kim, V. K. Malik, L. Schultz, S. Thiel, C. W. Schneider, J. Mannhart, G. Herranz, O. Copie, M. Bibes, A. Barthélémy, and C. Bernhard, "Dynamical Response and Confinement of the Electrons at the $LaAlO_3/SrTiO_3$ Interface," *Phys. Rev. Lett.* **104**, 156807 (2010). 40, 64

[74] M. Sing, G. Berner, K. Goß, A. Müller, A. Ruff, A. Wetscherek, S. Thiel, J. Mannhart, S. A. Pauli, C. W. Schneider, P. R. Willmott, M. Gorgoi, F. Schäfers, and R. Claessen, "Profiling the Interface Electron Gas of $LaAlO_3/SrTiO_3$ Heterostructures with Hard X-Ray Photoelectron Spectroscopy," *Phys. Rev. Lett.* **102**, 176805 (2009). 40, 44, 62, 64

[75] P. Perna, D. Maccariello, M. Radovic, U. S. di Uccio, I. Pallecchi, M. Codda, D. Marre, C. Cantoni, J. Gazquez, M. Varela, S. J. Pennycook, and F. M. Granozio, "Conducting interfaces between band insulating oxides: The $LaGaO_3/SrTiO_3$ heterostructure," *Appl. Phys. Lett.* **97**, 152111 (2010). 40,

43, 51

[76] M. Reinle-Schmitt, C. Cancellieri, D. Li, D. Fontaine, M. Medarde, E. Pomjakushina, C. Schneider, S. Gariglio, P. Ghosez, J.-M. Triscone, and P. Willmott, "Tunable conductivity threshold at polar oxide interfaces," *Nature Communications* **3**, 932 (2012). 40

[77] R. Pentcheva and W. E. Pickett, "Avoiding the Polarization Catastrophe in $LaAlO_3$ Overlayers on $SrTiO_3$(001) through Polar Distortion," *Phys. Rev. Lett.* **102**, 107602 (2009). 40

[78] M. S. Park, S. H. Rhim, and A. J. Freeman, "Charge compensation and mixed valency in $LaAlO_3/SrTiO_3$ heterointerfaces studied by the FLAPW method," *Phys. Rev. B* **74**, 205416 (2006). 40

[79] V. Vonk, M. Huijben, K. J. I. Driessen, P. Tinnemans, A. Brinkman, S. Harkema, and H. Graafsma, "Interface structure of $SrTiO_3/LaAlO_3$ at elevated temperatures studied in situ by synchrotron X-rays," *Phys. Rev. B* **75**, 235417 (2007). 40, 43

[80] J. Maurice, C. Carrétéro, M. Casanove, K. Bouzehouane, S. Guyard, E. Larquet, and J. Contour, "Electronic conductivity and structural distortion at the interface between insulators $SrTiO_3$ and $LaAlO_3$," *Phys. Status Solidi A* **203**, 2209–2214 (2006). 41

[81] M. Salluzzo, J. C. Cezar, N. B. Brookes, V. Bisogni, G. M. De Luca, C. Richter, S. Thiel, J. Mannhart, M. Huijben, A. Brinkman, G. Rijnders, and G. Ghiringhelli, "Orbital Reconstruction and the Two-Dimensional Electron Gas at the $LaAlO_3/SrTiO_3$ Interface," *Phys. Rev. Lett.* **102**, 166804 (2009). 41

[82] G. Herranz, M. Basletic, M. Bibes, C. Carretero, E. Tafra, E. Jacquet, K. Bouzehouane, C. Deranlot, A. Hamzic, J. Broto, A. Barthelemy, and A. Fert, "High Mobility in $LaAlO_3/SrTiO_3$ Heterostructures: Origin, Dimensionality, and Perspectives," *Phys. Rev. Lett.* **98**, 216803 (2007). 41

[83] A. S. Kalabukhov, Y. A. Boikov, I. T. Serenkov, V. I. Sakharov, V. N. Popok, R. Gunnarsson, J. Börjesson, N. Ljustina, E. Olsson, D. Winkler, and T. Claeson, "Cationic Disorder and Phase Segregation in $LaAlO_3/SrTiO_3$ Heterointerfaces Evidenced by Medium-Energy Ion Spectroscopy," *Phys. Rev. Lett.* **103**, 146101 (2009). 41, 92

[84] J. J. Yang, F. Miao, M. D. Pickett, D. A. A. Ohlberg, D. R. Stewart, C. N. Lau, and R. S. Williams, "The mechanism of electroforming of metal oxide

memristive switches," *Nanotechnology* **20**, 215201 (2009). 41, 87

[85] Y. Chen, N. Pryds, J. E. Kleibeuker, G. Koster, J. Sun, E. Stamate, B. Shen, G. Rijnders, and S. Linderoth, "Metallic and Insulating Interfaces of Amorphous $SrTiO_3$-Based Oxide Heterostructures," *Nano Lett.* **11**, 3774 (2011). 42, 87

[86] A. Brinkman, M. Huijben, M. van Zalk, J. Huijben, U. Zeitler, J. C. Maan, W. G. van der Wiel, G. Rijnders, D. H. A. Blank, and H. Hilgenkamp, "Magnetic effects at the interface between non-magnetic oxides.," *Nature Mater.* **6** (2007). 43

[87] W. Siemons, G. Koster, H. Yamamoto, W. A. Harrison, G. Lucovsky, T. H. Geballe, D. H. A. Blank, and M. R. Beasley, "Origin of Charge Density at $LaAlO_3$ on $SrTiO_3$ Heterointerfaces: Possibility of Intrinsic Doping," *Phys. Rev. Lett.* **98**, 196802 (2007). 43

[88] N. Reyren, S. Gariglio, A. D. Caviglia, D. Jaccard, T. Schneider, and J. Triscone, "Anisotropy of the superconducting transport properties of the $LaAlO_3/SrTiO_3$ interface," *Appl. Phys. Lett.* **94**, 112506 (2009). 43

[89] A. Savoia, D. Paparo, P. Perna, Z. Ristic, M. Salluzzo, F. Miletto Granozio, U. Scotti di Uccio, C. Richter, S. Thiel, J. Mannhart, and L. Marrucci, "Polar catastrophe and electronic reconstructions at the $LaAlO_3/SrTiO_3$ interface: Evidence from optical second harmonic generation," *Phys. Rev. B* **80**, 075110 (2009). 43, 51, 62, 64

[90] A. Ohtomo, D. A. Muller, J. L. Grazul, and H. Y. Hwang, "Artificial charge-modulationin atomic-scale perovskite titanate superlattices.," *Nature* **419** (2002). 43

[91] Y. Hotta, Y. Mukunoki, T. Susaki, H. Y. Hwang, L. Fitting, and D. A. Muller, "Growth and epitaxial structure of $LaVO_x$ films," *Appl. Phys. Lett.* **89**, 031918 (2006). 43

[92] Y. Hotta, T. Susaki, and H. Y. Hwang, "Polar Discontinuity Doping of the $LaVO_3/SrTiO_3$ Interface," *Phys. Rev. Lett.* **99**, 236805 (2007). 43

[93] U. S. di Uccio, C. Aruta, C. Cantoni, E. Di Gennaro, A. Gadaleta, A. R. Lupini, D. Maccariello, D. Marré, I. Pallecchi, D. Paparo, P. Perna, M. Riaz, and F. Miletto Granozio, "Reversible and Persistent Photoconductivity at the $NdGaO_3/SrTiO_3$ Conducting Interface," *ArXiv e-prints* (2012) 1206.5083. 43

[94] A. Kalabukhov, R. Gunnarsson, T. Claeson, and D. Winkler, "Electrical transport properties of polar heterointerface between KTaO3 and SrTiO3," *ArXiv e-prints* (2007) 0704.1050. 43

[95] V. E. Henrich, G. Dresselhaus, and H. J. Zeiger, "Surface defects and the electronic structure of $SrTiO_3$ surfaces," *Phys. Rev. B* **17**, 4908 (1978). 44

[96] A. Fujimori, I. Hase, M. Nakamura, H. Namatame, Y. Fujishima, Y. Tokura, M. Abbate, F. M. F. de Groot, M. T. Czyzyk, J. C. Fuggle, O. Strebel, F. Lopez, M. Domke, and G. Kaindl, "Doping-induced changes in the electronic structure of $La_xSr_{1-x}TiO_3$: Limitation of the one-electron rigid-band model and the Hubbard model," *Phys. Rev. B* **46**, 9841 (1992). 44

[97] D. D. Sarma, S. R. Barman, H. Kajueter, and G. Kotliar, "Spectral functions in doped transition metal oxides," *Europhys. Lett.* **36**, 307 (1996). 44, 85

[98] T. Higuchi, T. Tsukamoto, N. Sata, M. Ishigame, Y. Tezuka, and S. Shin, "Electronic structure of p-type $SrTiO_3$ by photoemission spectroscopy," *Phys. Rev. B* **57**, 6978 (1998). 44

[99] T. Higuchi, T. Tsukamoto, K. Kobayashi, Y. Ishiwata, M. Fujisawa, T. Yokoya, S. Yamaguchi, and S. Shin, "Electronic structure in the band gap of lightly doped $SrTiO_3$ by high-resolution x-ray absorption spectroscopy," *Phys. Rev. B* **61**, 12860 (2000). 44

[100] F. D. M. Haldane and P. W. Anderson, "Simple model of multiple charge states of transition-metal impurities in semiconductors," *Phys. Rev. B* **13**, 2553 (1976). 44

[101] H. Raebiger, S. Lany, and A. Zunger, "Charge self-regulation upon changing the oxidation state of transition metals in insulators," *Nature* **453**, 763 (2008). 44

[102] N. Shanthi and D. D. Sarma, "Electronic structure of electron doped $SrTiO_3$: $SrTiO_{3-x}$ and $Sr_{1-x}La_xTiO_3$," *Phys. Rev. B* **57**, 2153 (1998). 44, 62, 87

[103] Y. Ishida *et al.*, "Coherent and Incoherent Excitations of Electron-Doped $SrTiO_3$," *Phys. Rev. Lett.* **100**, 056401 (2008). 44, 84

[104] W. Meevasana, P. D. C. King, R. H. He, S. Mo, M. Hashimoto, A. Tamai, P. Songsiriritthigul, F. Baumberger, and Z. Shen, "Creation and control of a two-dimensional electron liquid at the bare $SrTiO_3$ surface," *Nat. Mater.* **10**, 114 (2011). 44

[105] A. F. Santander-Syro, O. Copie, T. Kondo, F. Fortuna, S. Pailhès, R. Weht, X. G. Qiu, F. Bertran, A. Nicolaou, A. Taleb-Ibrahimi, P. Le Fèvre, G. Herranz, M. Bibes, N. Reyren, Y. Apertet, P. Lecoeur, A. Barthélémy, and M. J. Rozenberg, "Two-dimensional electron gas with universal subbands at the surface of $SrTiO_3$," *Nature* **469**, 189 (2011). 44

[106] M. Kawasaki, A. Ohtomo, T. Arakane, K. Takahashi, M. Yoshimoto, and H. Koinuma, "Atomic control of $SrTiO_3$ surface for perfect epitaxy of perovskite oxides," *Appl. Surf. Sci.* **107**, 102 (1996). 46

[107] G. Koster, B. L. Kropman, G. J. H. M. Rijnders, D. H. A. Blank, and H. Rogalla, "Quasi-ideal strontium titanate crystal surfaces through formation of strontium hydroxide," *Appl. Phys. Lett.* **73**, 2920 (1998). 46, 47

[108] T. Ohnishi, K. Shibuya, M. Lippmaa, D. Kobayashi, H. Kumigashira, M. Oshima, and H. Koinuma, "Preparation of thermally stable TiO_2-terminated $SrTiO_3$(100) substrate surfaces," *Appl. Phys. Lett.* **85**, 272 (2004). 46

[109] J. Zhang, D. Doutt, T. Merz, J. Chakhalian, M. Kareev, J. Liu, and L. Brillson, "Depth-resolved subsurface defects in chemically etched $SrTiO_3$," *Appl. Phys. Lett.* **94** (2009). 47

[110] N. Erdman and L. D. Marks, "$SrTiO_3$(001) surface structures under oxidizing conditions," *Surf. Sci.* **526**, 107 (2003). 47

[111] N. Erdman, O. Warschkow, M. Asta, K. R. Poeppelmeier, D. E. Ellis, and L. D. Marks, "Surface Structures of $SrTiO_3$ (001): A TiO_2-rich Reconstruction with a c(4×2) Unit Cell," *J. Am. Chem. Soc.* **125**, 10050 (2003). 47

[112] T. Kubo and H. Nozoye, "Surface structure of $SrTiO_3$(1 0 0)," *Surf. Sci.* **542**, 177 (2003). 48

[113] V. M. Kaganer, R. Köhler, M. Schmidbauer, R. Opitz, and B. Jenichen, "X-ray diffraction peaks due to misfit dislocations in heteroepitaxial structures," *Phys. Rev. B* **55**, 1793 (1997). 59

[114] J. E. Boschker, C. Folkman, C. W. Bark, A. F. Monsen, E. Folven, J. K. Grepstad, E. Wahlström, C. B. Eom, and T. Tybell, "Structural coupling across the $LaAlO_3/SrTiO_3$ interface: High-resolution x-ray diffraction study," *Phys. Rev. B* **84**, 205418 (2011). 59

[115] L. Qiao, T. C. Droubay, T. Varga, M. E. Bowden, V. Shutthanandan, Z. Zhu, T. C. Kaspar, and S. A. Chambers, "Epitaxial growth, structure, and intermixing at the $LaAlO_3/SrTiO_3$ interface as the film stoichiometry is varied," *Phys. Rev. B* **83**, 085408 (2011). 61

[116] D. Ricci, G. Bano, G. Pacchioni, and F. Illas, "Electronic structure of a neutral oxygen vacancy in $SrTiO_3$," *Phys. Rev. B* **68**, 224105 (2003). 85

[117] N. Pavlenko, T. Kopp, E. Y. Tsymbal, G. A. Sawatzky, and J. Mannhart, "Magnetic and superconducting phases at the $LaAlO_3/SrTiO_3$ interface: The role of interfacial Ti $3d$ electrons," *Phys. Rev. B* **85**, 020407 (2012). 87

[118] H. Y. Hwang, Y. Iwasa, M. Kawasaki, B. Keimer, N. Nagaosa, and Y. Tokura, "Emergent phenomena at oxide interfaces," *Nat. Mater.* **11**, 103 (2012). 92

[119] G. Balestrino, S. Martellucci, P. G. Medaglia, A. Paoletti, G. Petrocelli, and A. A. Varlamov, "Dependence of the critical temperature on n in $(BaCuO_2)_2/(CaCuO_2)_n$ superlattices," *Phys. Rev. B* **58**, R8925 (1998). 92

[120] A. Gozar, G. Logvenov, L. F. Kourkoutis, A. T. Bollinger, L. A. Giannuzzi, D. A. Muller, and I. Bozovic, "High-temperature interface superconductivity between metallic and insulating copper oxides," *Nature* **455**, 782 (2008). 92

[121] G. Logvenov, A. Gozar, and I. Bozovic, "High-Temperature Superconductivity in a Single Copper-Oxygen Plane," *Science* **326**, 699 (2009). 92

[122] H. Y. Hwang, "Tuning Interface States," *Science* **313**, 1895 (2006). 92

[123] W. A. Harrison, E. A. Kraut, J. R. Waldrop, and R. W. Grant, "Polar heterojunction interfaces," *Phys. Rev. B* **18**, 4402 (1978). 93

[124] S. A. Chambers, T. Droubay, T. C. Kaspar, and M. Gutowski, "Experimental determination of valence band maxima for $SrTiO_3$, TiO_2, and SrO and the associated valence band offsets with Si(001)," *J. Vac. Sci. Technol. B* **22**, 2205 (2004). 97

[125] L. Qiao, T. Droubay, T. Kaspar, P. Sushko, and S. Chambers, "Cation mixing, band offsets and electric fields at $LaAlO_3/SrTiO_3(001)$ heterojunctions with variable La:Al atom ratio," *Surf. Sci.* **605**, 1381 (2011). 97

[126] M. A. van Veenendaal, H. Eskes, and G. A. Sawatzky, "Strong nonlocal contributions to Cu $2p$ photoelectron spectroscopy," *Phys. Rev. B* **47**, 11462 (1993). 106

[127] K. Okada and A. Kotani, "Nonlocal screening effects on core-level photoemission spectra investigated by large-cluster models," *Phys. Rev. B* **52**, 4794 (1995). 106

[128] M. Taguchi, A. Chainani, N. Kamakura, K. Horiba, Y. Takata, M. Yabashi, K. Tamasaku, Y. Nishino, D. Miwa, T. Ishikawa, S. Shin, E. Ikenaga, T. Yokoya, K. Kobayashi, T. Mochiku, K. Hirata, and K. Motoya, "Bulk screening in core-level photoemission from Mott-Hubbard and charge-transfer systems," *Phys. Rev. B* **71**, 155102 (2005). 107

[129] Y. Lu, X. W. Li, G. Q. Gong, G. Xiao, A. Gupta, P. Lecoeur, J. Z. Sun, Y. Y. Wang, and V. P. Dravid, "Large magnetotunneling effect at low magnetic fields in micrometer-scale epitaxial $La_{0.67}Sr_{0.33}MnO_3$ tunnel junctions," *Phys. Rev. B* **54**, R8357 (1996). 110, 111

[130] J. Z. Sun, W. J. Gallagher, P. R. Duncombe, L. Krusin-Elbaum, R. A. Altman, A. Gupta, Y. Lu, G. Q. Gong, and G. Xiao, "Observation of large low-field magnetoresistance in trilayer perpendicular transport devices made using doped manganate perovskites," *Appl. Phys. Lett.* **69**, 3266 (1996). 110, 111

[131] M. B. Salamon and M. Jaime, "The physics of manganites: Structure and transport," *Rev. Mod. Phys.* **73**, 583 (2001). 110, 112, 116

[132] C. Zener, "Interaction between the d-Shells in the Transition Metals. II. Ferromagnetic Compounds of Manganese with Perovskite Structure," *Phys. Rev.* **82**, 403 (1951). 111

[133] A. J. Millis, T. Darling, and A. Migliori, "Quantifying strain dependence in "colossal" magnetoresistance manganites," *J. Appl. Phys.* **83**, 1588 (1998). 111

[134] S. Jin, T. H. Tiefel, M. McCormack, R. A. Fastnacht, R. Ramesh, and L. H. Chen, "Thousandfold Change in Resistivity in Magnetoresistive La-Ca-Mn-O Films," *Science* **264**, 413 (1994). 111

[135] J. Quintanilla and C. Hooley, "The strong-correlations puzzle," *Phys. World* **22**, 32 (2009). 112

[136] B. R. K. Nanda and S. Satpathy, "Electronic and magnetic structure of the $(LaMnO_3)_{2n}/(SrMnO_3)_n$ superlattices," *Phys. Rev. B* **79**, 054428 (2009). 112

[137] A. Galdi, C. Aruta, P. Orgiani, C. Adamo, V. Bisogni, N. B. Brookes, G. Ghiringhelli, D. G. Schlom, P. Thakur, and L. Maritato, "Electronic band redistribution probed by oxygen absorption spectra of $(SrMnO_3)_n(LaMnO_3)_{2n}$ superlattices," *Phys. Rev. B* **85**, 125129 (2012). 112, 124

[138] M. J. Calderón, L. Brey, and F. Guinea, "Surface electronic structure and magnetic properties of doped manganites," *Phys. Rev. B* **60**, 6698 (1999). 112

[139] H. Zenia, G. A. Gehring, G. Banach, and W. M. Temmerman, "Electronic and magnetic properties of the (001) surface of hole-doped manganites," *Phys. Rev. B* **71**, 024416 (2005). 112

[140] P. Orgiani, A. Y. Petrov, R. Ciancio, A. Galdi, L. Maritato, and B. A. Davidson, "Evidence of direct correlation between out-of-plane lattice parameter and metal-insulator transition temperature in oxygen-depleted manganite thin films," *Appl. Phys. Lett.* **100**, 042404 (2012). 112, 114

[141] Y. Du, B. Wang, T. Li, D. Yu, and H. Yan, "Effects of annealing procedures on the structural and magnetic properties of epitaxial $La_{0.7}Sr_{0.3}MnO_3$ films," *J. Magn. Magn. Mater.* **297**, 88 (2006). 112

[142] P. Orgiani, C. Aruta, R. Ciancio, A. Galdi, and L. Maritato, "Enhanced transport properties in $La_xMnO_{3-\delta}$ thin films epitaxially grown on $SrTiO_3$ substrates: The profound impact of the oxygen content," *Appl. Phys. Lett.* **95**, 013510 (2009). 112

[143] J. Ye and K. Nakamura, "Quantitative structure analyses of $YBa_2Cu_3O_{7-\delta}$ thin films: Determination of oxygen content from x-ray-diffraction patterns," *Phys. Rev. B* **48**, 7554 (1993). 112

[144] P. Murugavel, J. H. Lee, J.-G. Yoon, T. W. Noh, J.-S. Chung, M. Heu, and S. Yoon, "Origin of metal–insulator transition temperature enhancement in underdoped lanthanum manganite films," *Appl. Phys. Lett.* **82**, 1908 (2003). 112

[145] C. Aruta, M. Angeloni, G. Balestrino, N. G. Boggio, P. G. Medaglia, A. Tebano, B. Davidson, M. Baldini, D. D. Castro, P. Postorino, P. Dore, A. Sidorenko, G. Allodi, and R. D. Renzi, "Preparation and characterization of $LaMnO_3$ thin films grown by pulsed laser deposition," *J. Appl. Phys.* **100**,

023910 (2006). 112

[146] M. Sirena, N. Haberkorn, M. Granada, L. B. Steren, and J. Guimpel, "Metal-insulator transition induced by postdeposition annealing in low doped manganite films," *J. Appl. Phys.* **105**, 033902 (2009). 112

[147] C. Aruta, G. Balestrino, A. Tebano, G. Ghiringhelli, and N. B. Brookes, "Cooperative enhancement of in-plane orbital ordering by oxygen deficiency and in-plane tensile strain in $La_{0.7}Sr_{0.3}MnO_{3-\delta}$ thin films," *Europhys. Lett.* **80**, 37003 (2007). 112, 122

[148] X. J. Chen, S. Soltan, H. Zhang, and H.-U. Habermeier, "Strain effect on electronic transport and ferromagnetic transition temperature in $La_{0.9}Sr_{0.1}MnO_3$ thin films," *Phys. Rev. B* **65**, 174402 (2002). 112

[149] S. Picozzi, C. Ma, Z. Yang, R. Bertacco, M. Cantoni, A. Cattoni, D. Petti, S. Brivio, and F. Ciccacci, "Oxygen vacancies and induced changes in the electronic and magnetic structures of $La_{0.66}Sr_{0.33}MnO_3$: A combined ab initio and photoemission study," *Phys. Rev. B* **75**, 094418 (2007). 113, 122

[150] F. Offi, N. Mannella, T. Pardini, G. Panaccione, A. Fondacaro, P. Torelli, M. W. West, J. F. Mitchell, and C. S. Fadley, "Temperature-dependent electronic structure of the colossal magnetoresistive manganite $La_{0.7}Sr_{0.3}MnO_3$ from hard x-ray photoemission," *Phys. Rev. B* **77**, 174422 (2008). 113, 122

[151] V. R. Galakhov, M. Demeter, S. Bartkowski, M. Neumann, N. A. Ovechkina, E. Z. Kurmaev, N. I. Lobachevskaya, Y. M. Mukovskii, J. Mitchell, and D. L. Ederer, "Mn 3*s* exchange splitting in mixed-valence manganites," *Phys. Rev. B* **65**, 113102 (2002). 113

[152] E. Beyreuther, S. Grafström, L. M. Eng, C. Thiele, and K. Dörr, "XPS investigation of Mn valence in lanthanum manganite thin films under variation of oxygen content," *Phys. Rev. B* **73**, 155425 (2006). 113

[153] A. Y. Petrov, C. Aruta, S. Mercone, C. Adamo, I. Alessandri, and L. Maritato, "Room temperature metal-insulator transition in as grown (LaSr) MnO thin films deposited by molecular beam epitaxy," *Eur. Phys. J. B* **40**, 11 (2004). 113

[154] L. J. van der Pauw, "A method of measuring specific resistivity and Hall effect of discs of arbitrary shape," *Philips Res. Rep.* **13** (1958). 114

[155] E. Dagotto, editor, *Nanoscale Phase Separation and Colossal Magnetoresistance* (Springer-Verlag, Heidelberg, 2003). 116

[156] M. Jaime, P. Lin, M. B. Salamon, and P. D. Han, "Low-temperature electrical transport and double exchange in $La_{0.67}$ $(Pb,Ca)_{0.33}MnO_3$," *Phys. Rev. B* **58**, R5901 (1998). 116

[157] P. Schiffer, A. P. Ramirez, W. Bao, and S.-W. Cheong, "Low Temperature Magnetoresistance and the Magnetic Phase Diagram of $La_{1-x}Ca_xMnO_3$," *Phys. Rev. Lett.* **75**, 3336 (1995). 117

[158] S. Mercone, C. A. Perroni, V. Cataudella, C. Adamo, M. Angeloni, C. Aruta, G. De Filippis, F. Miletto, A. Oropallo, P. Perna, A. Y. Petrov, U. Scotti di Uccio, and L. Maritato, "Transport properties in manganite thin films," *Phys. Rev. B* **71**, 064415 (2005). 117

[159] N. F. Mott, *Metal-insulator Transitions*, 2 ed. (Taylor & Francis, London, 1990). 117

[160] C. P. Adams, J. W. Lynn, Y. M. Mukovskii, A. A. Arsenov, and D. A. Shulyatev, "Charge Ordering and Polaron Formation in the Magnetoresistive Oxide $La_{0.7}Ca_{0.3}MnO_3$," *Phys. Rev. Lett.* **85**, 3954 (2000). 117

[161] C. Adamo, C. A. Perroni, V. Cataudella, G. De Filippis, P. Orgiani, and L. Maritato, "Tuning the metal-insulator transitions of $(SrMnO_3)_n/(LaMnO_3)_{2n}$ superlattices: Role of interfaces," *Phys. Rev. B* **79**, 045125 (2009). 117

[162] P. A. Lee and T. V. Ramakrishnan, "Disordered electronic systems," *Rev. Mod. Phys.* **57**, 287 (1985). 117

[163] L. Maritato, C. Adamo, C. Barone, G. M. De Luca, A. Galdi, P. Orgiani, and A. Y. Petrov, "Low-temperature resistivity of $La_{0.7}Sr_{0.3}MnO_3$ ultra thin films: Role of quantum interference effects," *Phys. Rev. B* **73**, 094456 (2006). 117

[164] J. M. Rondinelli, N. M. Caffrey, S. Sanvito, and N. A. Spaldin, "Electronic properties of bulk and thin film $SrRuO_3$: Search for the metal-insulator transition," *Phys. Rev. B* **78**, 155107 (2008). 124

[165] P. Orgiani, C. Aruta, G. Balestrino, S. Lavanga, P. Medaglia, and A. Tebano, "Strain effect on transport properties of $SrRuO_3$ films grown by laser MBE," *Eur. Phys. J. B* **26**, 23 (2002). 124

[166] P. Orgiani, C. Adamo, C. Barone, A. Galdi, A. Y. Petrov, D. G. Schlom, and L. Maritato, "Influence of a single disorder parameter on the conduction mechanisms in manganite thin films," *Phys. Rev. B* **76**, 012404 (2007). 126

[167] J. Karpinski, I. Mangelschots, H. Schwer, K. Conder, A. Morawski, T. Lada, and A. Paszewin, "Single crystal growth of HgBaCaCuO and infinite layer $CaCuO_2$ at high gas pressure," *Physica C* **235-240**, 917 (1994). 141

Acronyms

2DEG	2-dimensional electron gas
AES	Auger electron spectroscopy
AFM	Atomic force microscopy
ARPES	Angle resolved photoelectron spectroscopy
BHF	Buffered hydroflouric acid
CCO	Calcium cuprate – $CaCuO_2$
CMR	Colossal magnetoresisitance
CT-AFM	Conducting-tip atomic force microscopy
CTR	Crystal truncation rod
EH	Experimental hutch
HAXPES	Hard X-ray photoelectron spectroscopy
HTS	High-temperature superconductivity
LAO	Lanthanum alluminate – $LaAlO_3$
LEED	Low energy electron diffraction
LSMO	Lanthanum doped strontium manganate – $La_{(1-x)}Sr_xMnO_3$
MBE	Molecular beam epitaxy
ML	Monoloayer
MOSFET	Metal-oxide-semiconductor field-effect transistor

PLD	Pulsed laser deposition
RHEED	Reflection high energy electron diffraction
r.l.u.	Reciprocal lattice units
RSM	Reciprocal space map
SCL	Surface characterization laboratory
STO	Strontuim titanate – $SrTiO_3$
SXPS	Soft X-ray photoelectron spectroscopy
SXRD	Surface X-ray diffraction
TMO	Transition metal oxide
UHV	Ultra-high vacuum
UPS	Ultraviolet photoelectron spectroscopy
UC	Unit cell
XPS	X-ray photoelectron spectroscopy
XSW	X-ray standing wave field
YBCO	Yttrium barium cuprate – $YBa_2Cu_3O_{7-\delta}$

Acknowledgement

Foremost, I would like to express my gratitude to **Jörg Zegenhagen** who shared with me a lot of his expertise and research insight. His enthusiasm, inspiration, and great professionalism were most helpful with this work and for me in my personal development. Thank you for your ongoing support.

I would like to thank especially **Robert Johnson** for supervising this thesis, his thoughtful advise in the production of this work and the detailed proofreading of the manuscript.

I am indebted to **Christof Kunz** who kindly agreed to serve as an examiner of this thesis.

Many people contributed to this work over the last few years. I want to express a big thank you to all of you!

The huge impact by **Tien-Lin Lee** cannot be understated. His enthusiasm, profound knowledge and patience were extremely helpful. Although he spent most of his time at Diamond he did not mind the time, costs and effort to come for nearly all off my beam times to the ESRF. Thank you for everything!

Lina Aruta was of great help in this work. She provided the high quality $LaAlO_3/SrTiO_3$ samples from Naples and established the contact for two fruitful collaborations on $La_{0.65}Sr_{0.35}MnO_{3-\delta}$ films and $CaCuO_2/SrTiO_3$ superlattices. Thank you for your help! I acknowledge the people form here lab who helped with the $LaAlO_3/SrTiO_3$ sample preparation: **Fabio Miletto Granozio, Umberto Scotti di Uccio and Emiliano Di Gennaro**.

In this context I want to thank **Pasquale Origiani**, **Bruce Davidson**, **Alice Galdi** and their colleagues for the collaboration in the $La_{0.65}Sr_{0.35}MnO_{3-\delta}$ project and providing excellent samples.

I am very grateful to all the people involved in the $CaCuO_2/SrTiO_3$ superlattices project in Rome: **Daniele Di Castro, Davide Innocenti, Antonello Tebano, and Guiseppe Balestrino**. It was very exciting to work on these unique samples!

Jean-Francois Guillet assisted with the AFM measurements in the Surface Science Laboratory of the ESRF.

Of course on the beam line support is essential and my thanks go to **Lionel André, Blanka Detlefs, Julien Duvernay, Jérôme Roy, Yanyu Mi, Helena Isern, Lucien Petit, Hadeel Hussain, Frederik Golks and Parasmani Rajput** for their vital assistance at the ID32 beamline and all the advise and help given. I enjoyed my time at the ESRF with you. Thank you for the uncounted coffee breaks, night shifts, cakes and chats!

I want to thank the people I had the chance to share my office with and make friends: **Thomas Cornelius, Frederick Golcks, Anastasios Pasteras, Thomas Scheler, Fracesca Mastroprieto, Genziana Bussone, Hadeel Hussain, Valentina Cantelli, Raphael Griffone, Riccardo Mettere, Jean-Piere Valade, and Nicolas Bocanegra**. Thank you for the nice atmosphere in our office and the many happy moments. It was a pleasure to share the room with you! Also outside of work, I had the chance to make some great friends. Especially I want to mention **Najor, Jonathan, Emilio, Felipe, Christoforos** and **Lef** for their friendship and many good moments as well as **Maciej** and **Bogdan** for being amazing flat mates and even better friends.

Furthermore, I want to express my deepest gratitude to **Nuria** for all her support and love. Thanks to you, everything is always a bit easier.

Last but not least I want want to thank my parents, **Dorothee** and **Robert Schlueter** as well as my sister **Katharina** for their continuous support and encouragement.

Christoph Schlueter